

Non-contact femtosecond laser-based methods for investigating glass mechanics at small scales

THÈSE N° 8323 (2018)

PRÉSENTÉE LE 29 MARS 2018

À LA FACULTÉ DES SCIENCES ET TECHNIQUES DE L'INGÉNIEUR

LABORATOIRE GALATEA

PROGRAMME DOCTORAL EN PHOTONIQUE

ÉCOLE POLYTECHNIQUE FÉDÉRALE DE LAUSANNE

POUR L'OBTENTION DU GRADE DE DOCTEUR ÈS SCIENCES

PAR

Christos Edouardos ATHANASIOU

acceptée sur proposition du jury:

Prof. D. Psaltis, président du jury
Prof. Y. Bellouard, directeur de thèse
Prof. M. Lancry, rapporteur
Prof. J. Vlassak, rapporteur
Prof. F. Sorin, rapporteur



ÉCOLE POLYTECHNIQUE
FÉDÉRALE DE LAUSANNE

Suisse
2018

Abstract

With the progress made in miniaturizing systems over the last decades, understanding materials' behavior at small scales has become a necessity.

In this context, glass behavior has remained largely unknown, partly for technological reasons and partly due to the inherent difficulties associated with its brittle fracture behavior. Despite their importance for technological implementation, questions such as its failure statistics or its behavior under constant load remain unanswered.

This thesis aims at filling the gap of the available methodologies and instrumentation for the mechanical testing of glass at the micro-/nano- scale.

Until recently, suitable methods for manufacturing arbitrary shapes in glass were missing, hampering the implementation of appropriate testing methods. Fortunately, recent progress in the field of femtosecond laser processing has opened new opportunities for designing specific tools adapted to the investigation of glass micromechanics. In addition, the careful observation of nanoscale self-organization processes taking place during laser exposure offers a novel means for observing fracture statistical behavior.

Here, we use this novel glass processing method to introduce two novel experimental approaches: one based on novel concept of contactless micro-/nano-monolithic tensile tester, and a second one, based on statistical observations of an intermittent behavior occurring during laser exposure. Using these two approaches, we are able not only to load the material to unprecedented high level of stress and this, in a pure tensile mode, but also to study stress relaxation effects and finally, to explore its fracture statistical behavior.

From the technology development perspective, this thesis offers an experimental framework for contactless testing of glass materials that, in particular for silica, set guidelines for microsystems designers. In parallel, this work demonstrates the use of unconventional methods, inherited from other scientific disciplines, as a means for extracting relevant brittle fracture parameters, usually difficult to obtain at the micro-scale and requiring extensive numbers of experiments.

Keywords: Fused silica, mechanics, micro-scale, fracture, femtosecond lasers

Résumé

Avec les progrès effectués dans la miniaturisation des systèmes au cours des dernières décennies, la compréhension du comportement des matériaux aux petites échelles est devenue une nécessité.

Dans ce contexte, le comportement des verres en général reste méconnu, d'une part pour des raisons technologiques, et d'autre part, en raison des difficultés inhérentes associées à son comportement fragile en rupture. Entre autres, des questions telles que sa probabilité de rupture ou son comportement sous une charge constante, demeurent sans réponse, et ceux, malgré leurs importances pour l'implémentation technologique. Ceci est d'autant plus vrai pour le verre de silice.

Cette thèse a pour objectif principal de combler le vide quant aux méthodes et l'instrumentation disponibles pour tester le verre de silice aux échelles micro- et nanométriques.

Jusqu'à récemment, les technologies de fabrication de formes arbitraires dans le verre de silice étaient limitées, entravant ainsi la mise en œuvre de méthodes de tests appropriées. L'usinage par laser à impulsions femtosecondes a changé la donne en permettant la conception d'outils spécifiques à l'étude micromécanique de ces matériaux. De plus, comme nous le verrons dans ce travail, l'observation minutieuse des procédés d'auto-organisation à l'échelle nanométrique résultant de l'exposition laser, offre un moyen inattendu pour l'étude du comportement statistique en rupture.

Dans ce travail, nous utilisons cette nouvelle méthode d'usinage du verre pour étudier deux nouvelles approches expérimentales : une première, basée sur un nouveau concept d'essai de traction monolithique sans contact, et une deuxième, tirant profit d'observations statistiques d'un comportement intermittent survenant lors de l'exposition laser. En utilisant ces deux approches, nous sommes capables, non seulement d'astreindre le matériau à un haut niveau de contrainte - et ceci dans un mode en traction pure, mais également d'étudier les effets de relaxation, et finalement, d'étudier son comportement en rupture.

Dans la perspective de futurs développements technologiques, cette thèse offre une méthodologie et un cadre expérimental pour tester - sans contact - les verres de silice, permettant d'établir des lignes directrices pour les concepteurs de microsystèmes. En parallèle, ce travail démontre l'utilisation de méthodes non-conventionnelles, héritées d'autres disciplines scientifiques, permettant d'extraire des paramètres pertinents pour prédire une rupture fragile, habituellement difficiles à obtenir à l'échelle microscopique et nécessitant un nombre important d'expériences.

Mots clés: verre, mécanique, échelle micrométrique, rupture, laser à impulsions femtosecondes.

Table of Contents

Abstract.....	iii
Résumé.....	v
Chapter I - Motivation & Thesis Objectives.....	1
A. Thesis rationale	2
B. Problem statement	5
C. Glass mechanics and fracture	6
D. State-of-the-art mechanical testing at small scales	7
i) Micro- and nano-indentation	7
ii) Three-points bending test	9
iii) Bulge test	10
iv) Mechanical resonance test	11
v) Micro-scale tensile testing	12
E. Thesis objectives	14
F. Thesis outline	14
Chapter II - A Tensile Tester to Investigate Fused Silica Fracture Mechanics	17
A. Introduction	18
B. Femtosecond lasers as a means to manufacture and load fused silica devices	19
i) Micro-manufacturing.....	20
ii) Stress manipulation	21
C. Micro-tensile tester design and working principle	22
i) Micro-scale tensile testing	22
ii) Test beam dimensioning and loading cell	24
iii) Lever amplification mechanism	25
iv) Mechanical guidance	26
D. Experimental results.....	28
i) Manufacturing	28
ii) Loading scheme optimization	29
iii) Third-harmonic generation (THG) as an in-situ metrology tool.....	33
iv) Stress monitoring through photoelasticity	35
v) Stress measurement on silica micro-beam.....	36
vi) Weibull statistics of femtosecond laser processed fused silica loaded in uniaxial tension at the micro-scale.....	39

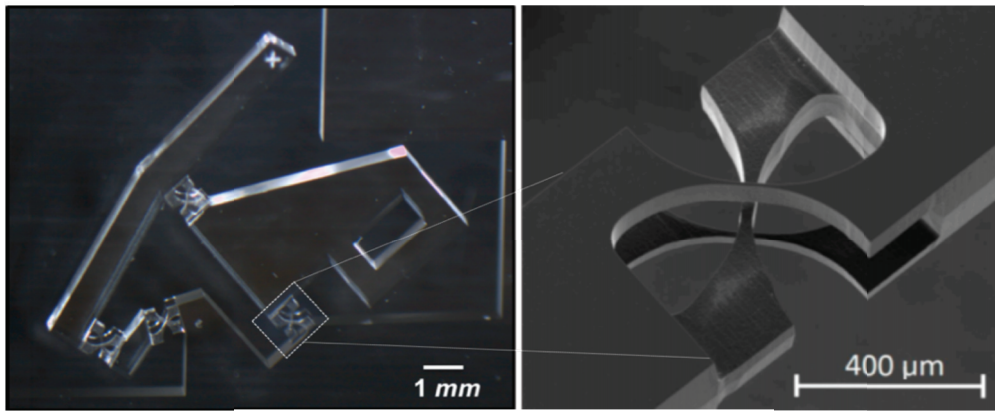
vii) Error analysis for the experimental technique.....	40
E. Discussion.....	40
F. Conclusions and Outlook.....	41
Chapter III - Relaxation Phenomena in Fused Silica Specimens Under Constant Tensile Stress	43
A. Introduction.....	44
B. Experimental procedure	44
i) Micro-tensile tester design and working principle	44
ii) Manufacturing	45
iii) Measurement setup.....	45
C. Experimental results.....	49
i) Stress evolution of fused silica, or the laser affected zones?	50
ii) Interpretation and discussion.....	51
D. Conclusion	53
Chapter IV - A Femtosecond Laser to Investigate Fused Silica Fracture Mechanics	55
A. Introduction.....	56
B. Experimental observation of intermittent behavior.....	56
i) Experimental method.....	56
ii) Surface modification and observations	57
C. Modeling the intermittent behavior.....	59
i) Concept of nano-fracture experiments	59
ii) Queuing system framework.....	61
iii) Microscopic modelling.....	64
D. Experimental results.....	66
i) Nano-loading results on fused silica.....	66
ii) Further validation: Effect of surface quality on mechanical strength	69
iii) Testing other brittle materials: Sapphire and α -quartz.....	70
E. State-of-the-art nanogratings formation models and discussion	72
F. Conclusion	73
Chapter V - Proof-of-Concept: Stress-Based Polarization Device	75
A. Introduction.....	76
B. Waveplate concept	76
C. Experimental procedure	77
i) Setup and measurement principle.....	77

ii) Experimental results	79
D. Modelling and Discussion.....	81
i) One-dimensional analytical model	81
ii) Two-dimensional analytical model	84
iii) Comparison with experimental results.....	86
E. Conclusion.....	87
Chapter VI - Conclusions & Discussion.....	89
A. Retrospective.....	90
B. Future work	91
Appendix.....	95
Appendix A: Fused silica properties.....	96
Appendix B: Types of modifications in fused silica.....	97
Appendix C: Parameters influencing the femtosecond laser processing method	99
Bibliography	103
Authors Contributions.....	117
Acknowledgements.....	119

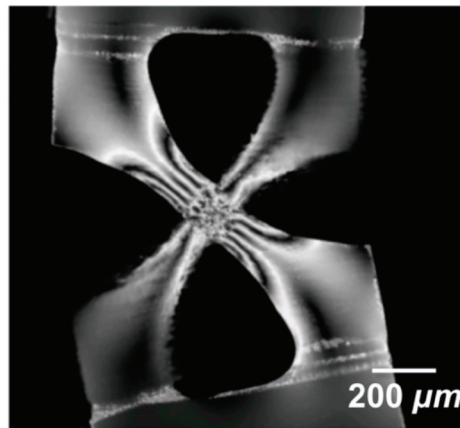
Chapter I - MOTIVATION & THESIS OBJECTIVES

A. Rationale

Femtosecond laser micromanufacturing has opened new opportunities for producing glass-based microdevices; it provides the intrinsic capability to manufacture three-dimensional (3D) systems with high surface qualities [1-3]. The monolithic glass microdevices can combine optical, mechanical, and fluid-handling functionalities altogether (or separately), in a single piece of fused silica. In this section, examples of such devices developed for both industrial and academic needs are presented.



(a)



(b)

Fig. 1. (a) (Left) Image acquired by an optical microscope of a monolithic mechanical guidance (known as Hoecken linkage), machined out of a single piece of fused silica [4]. (Right) Scanning electron microscope (SEM) image of the three-dimensional hinge. (b) Photoelasticity image of the hinge. The hinge is in an angular deformation 13° from its rest position corresponding to a stress of 1.9 GPa .

A first example is illustrated in Fig. 1a. A Hoecken linkage made of 3D cross-spring pivots is machined out of glass [4]. The role of this guidance is to convert a rotational motion into a linear one. An example where the hinge is highly deformed is shown in Fig. 1b.

A more complex example of device is shown in Fig. 2a, where an embedded Mach-Zehnder waveguide-based interferometer is manufactured exploiting the mechanical and optical properties of the fused silica substrate [3]. A flexure along with an integrated optical waveguide located in its geometrical center are fabricated. The flexure is vibrating while the waveguide follows the motion of the tip of the flexure.

In Fig. 2b, one of the first examples of an all-glass, flexure-based optical sensing devices is shown. As the mobile part of the device is linearly translated, a displacement sensing element consisting of integrated waveguides acts as an integrated linear encoder. More details on this work can be found here [1].

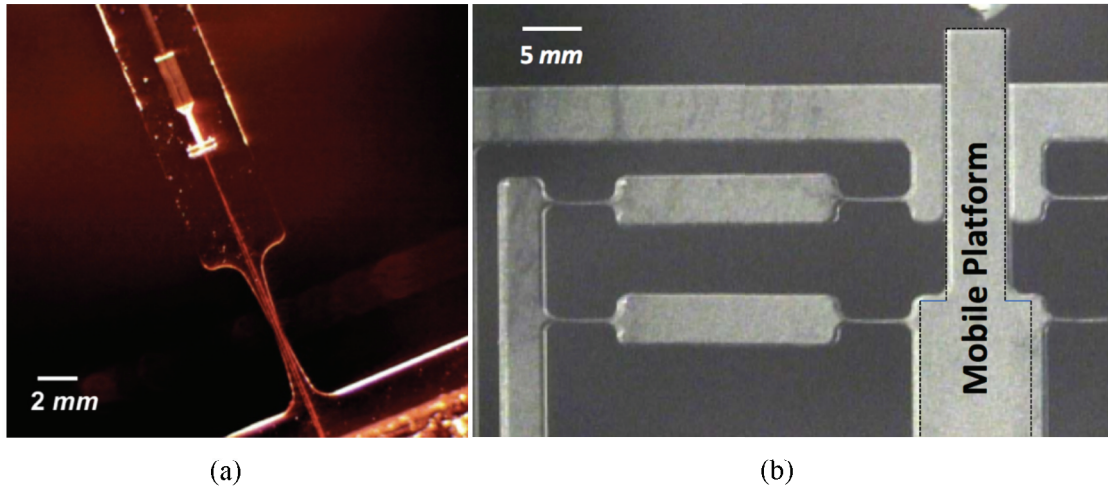


Fig. 2. (a) Image of a Mach-Zehnder interferometer machined out of a single piece of fused silica (Picture courtesy of Translume Inc.) [3]. (b) Optical microscope image of one of the first all-glass optical sensor merging optics and mechanics developed in a single silica substrate [1].

A mechanism designed to serve for eye surgeries is illustrated in Fig. 3. The glass mechanism is designed to be inserted into a cannula. The whole device is designed such as to penetrate the eye and puncture certain veins to deliver fluid that dissolves congestions in the blood flow.

From the industrial point of view, a recent example of device manufactured out of fused silica is a glass balance bridge illustrated in Fig. 4 (manufactured by FEMTOprint SA for Ulysse Nardin). The balance bridge is a micromechanical wheel that moves back and forth, being returned to its center position by a spiral torsion spring. The benefit of manufacturing this device out of a single piece of silica glass is the ability to integrate a spiral shock absorber to it, maintaining concentricity with the pivot.

Besides the examples of monolithic devices with optical, mechanical, and fluid-handling functionalities such as the ones shown here, the integration of electrical functionalities has also recently been demonstrated [5, 6].

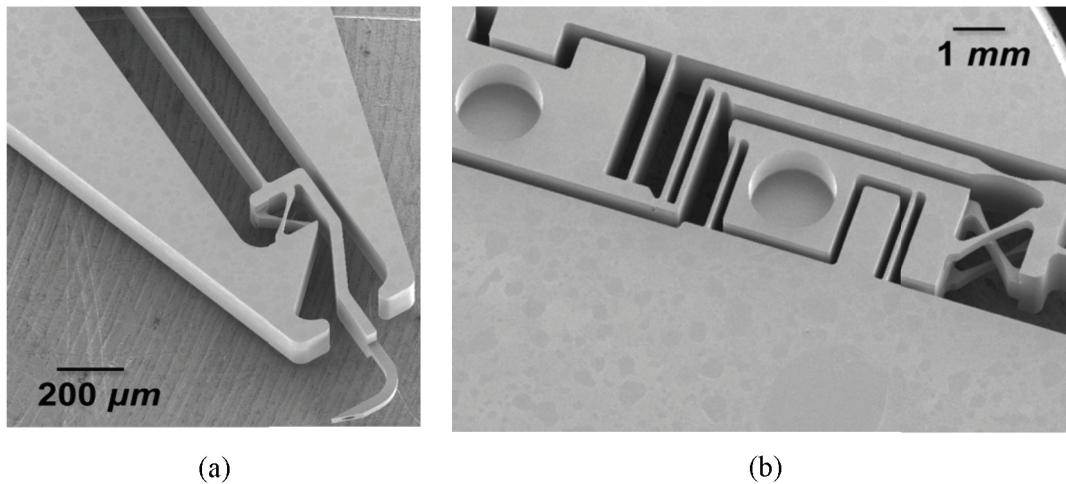


Fig. 3. A fused silica mechanism designed to serve as a tool for eye surgeries. The mechanism will be inserted into a cannula and the whole device will penetrate the eye, puncturing certain veins to deliver fluid that dissolves congestions in the blood flow. (a) the fluid will be delivered through the nozzle in veins with a diameter of approximately 100 μm . The diameter of the nozzle *per se* will be 10 μm (b) the mechanism converting linear to circular motion through a cross spring pivot is shown.

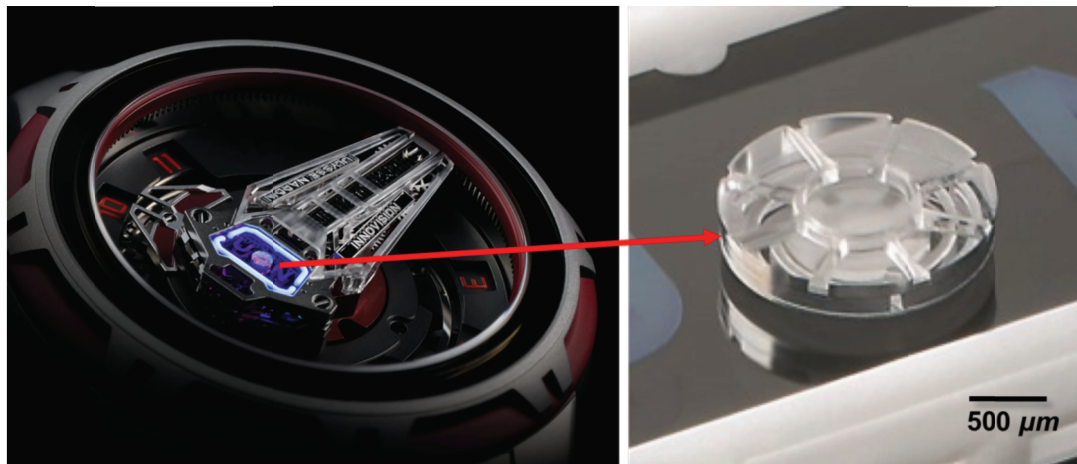


Fig. 4. A monolithic glass balance bridge features a spiral shock absorber that is made entirely out of the single piece of glass. The integrated shock-absorbing system maintains concentricity with the pivot as it is constructed out of a single piece of glass. The images are courtesy of Ulysse Nardin/FEMTOprint SA.

In summary, prototypes of multifunctional micromechanical devices have recently been produced out of a single piece of fused silica both for industrial and scientific needs. To date, researchers and engineers use trial-and-error methods to design such devices due to uncertainties associated with the mechanical behavior of the material.

Besides the technological and engineering challenges associated with the mechanical performance of fused silica, fundamental aspects of the mechanical behavior of the material at the micro- and nano-scale also remain unexplored.

Fused silica is prone to static fatigue under constant loading due to stress-corrosion effects, i.e., spontaneous crack growth leading to a reduction of the fracture strength in the presence of water molecules. However, a detailed view of the interaction of strained Si-O bonds with H₂O molecules is still a topic of debate [7-10].

At the nano-scale, silica glass is found to exhibit unconventional behavior such as “pseudoductility” [11-13]. Molecular dynamics simulations suggest that a fracture in silica glass proceeds through the growth and coalescence of nano-scale cavities [14]. Yet, this peculiar behavior has not been quantified.

B. Problem statement

In the first section of the introductory chapter, we highlighted the importance of further investigation of the mechanical properties of silica glass at small scales. However, testing materials at such scales is challenging; it requires delicate methods for applying controlled loads in a reproducible manner, while yet generating measurable displacements with high resolution.

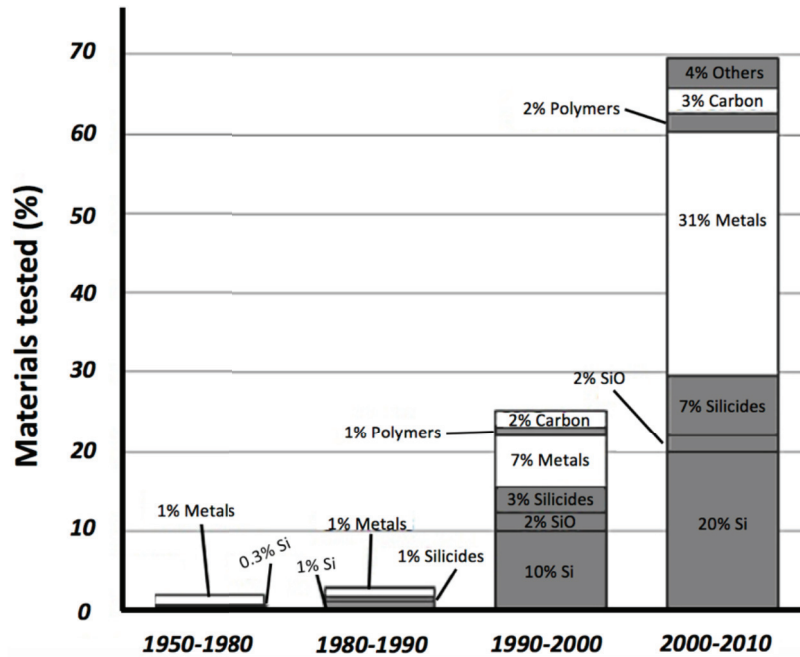


Fig. 5. Graph illustrating the materials tested at the micro-/nano-scales over the last decades [15]. Testing of glass materials has been limited due to the lack of the testing methods available.

The technical challenges associated with its testing make glass as a mechanically under-investigated material. This is reflected on the limited previous investigations as shown in Fig. 5 [15].

This thesis aims at filling the gap of available methodologies and instrumentation for mechanical testing glass materials at the micro-/nano- scale. In particular, based on the femtosecond laser interaction with silica, and in combination with new design approaches, we propose novel methods to investigate the mechanical properties of glass at small scales.

C. Glass mechanics and fracture

The fracture strength of glass is dictated by the presence of surface flaws rather than by the intrinsic strength of the Si–O bond. It fractures according to the weakest-link scaling (WLS) principle [16-18]. In the WLS framework, the material may be visualized as a one-dimensional chain (shown in Fig. 6). Its strength is controlled by the chain's weakest link (the link with the lowest mechanical strength); if the weakest link fails, the whole material fails. The Weibull model is the probability distribution (Fig. 7) for WLS systems and is used to predict fracture probability. The main assumption of the Weibull model is that there is no interaction between defects inside the material.

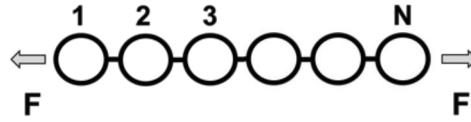


Fig. 6. Illustration of the weakest link model made up of a chain of elements, each representing a unit volume of material. According to this model if one link fails, the whole material fails.

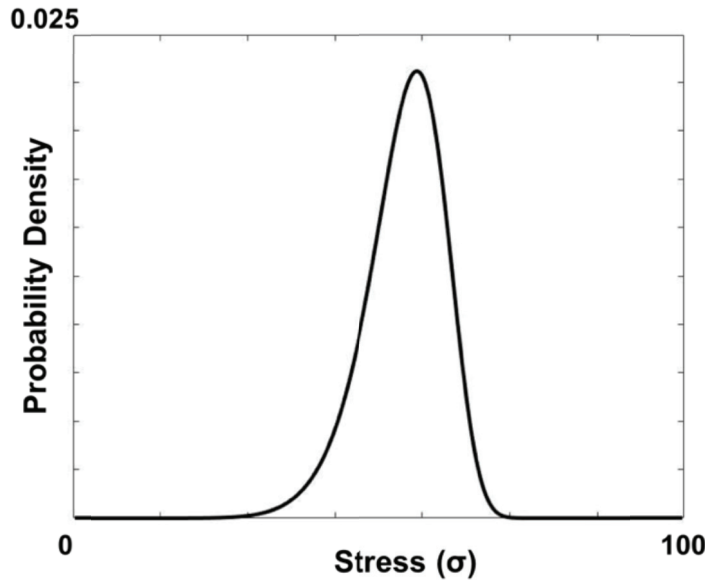


Fig. 7. Illustration of the probability density of the Weibull function for $m = 10$ and a fixed value of $\sigma_0 = 100$.

Fused silica's bulk Si–O network is of high purity. Thus, its weakest link may be reasonably assumed that lays on its surface. Surface flaws act as stress concentrators where

nucleation of cracks can take place. The probability of the material to fail is following a two-parameter Weibull distribution [16]:

$$P_f(m, \sigma_N; \sigma) = 1 - \exp[-(\sigma/\sigma_0)^m] \quad (1.1)$$

where P_f is the probability of the material to fail, if it is loaded to a stress level σ . The probability of the material surviving, R , is given by: $R = 1 - P_f$. The quantities σ_0 and m are model parameters that are determined by fitting of a logarithmic plot based on experimental data.

The shape parameter, m , is a property of the material under test. It is independent of the testing procedure and the tested volume, and therefore indicates the quality of the material tested. It essentially represents the scatter of the strength data: the smaller the m , the wider the distribution is. σ_0 is a characteristic strength value which depends on the testing method and volume.

A Weibull-type strength distribution arises both for homogeneous and inhomogeneous stress states. Moreover, it should be noted that for the case of non-uniform stress states a correction factor representing the effective surface (or volume) tested should be added in Eq. (1.1) as it will be further discussed in Chapter IV.

In this thesis, the experiments are conducted using synthetic fused silica meeting the quality standards of Corning 7980 0F [19]. Models, analyses and interpretations are assuming properties according to these standards. A detailed discussion on the properties of fused silica glass can be found in Appendix A.

D. State-of-the-art mechanical testing at small scales

In this section, the existing experimental techniques commonly used to perform static or dynamic mechanical testing of fused silica at small scales are examined (review publications can be found here [20-22]). The advantages and limitations of each method are outlined in the context of their applicability to our specific case.

i) Micro- and nano-indentation

Micro- and nano-indentation is a widely-used technique to determine mechanical properties of materials at small scales [23-25]. In a typical indentation test, the load is applied to an indenter that is in contact with the surface of the specimen as illustrated in Fig. 8. The load as well as the penetration depth are recorded as the load increases from zero to a peak value, and vice versa. When the indenter is removed from the material, the material attempts to regain its original shape.

From the indentation load-displacement curve, the hardness and the elastic modulus of the specimen can be determined. The specimen hardness H can be calculated with the peak load F_{max} by the following equation [22]:

$$H = \frac{F_{max}}{A} \quad (1.2)$$

where A is the projected contact area. The elastic modulus E can be estimated using the Oliver-Pharr analysis procedure as presented in [26].

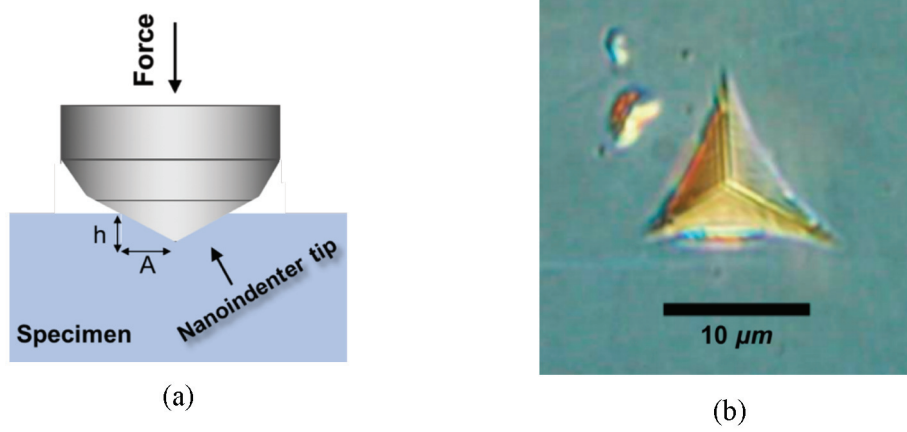


Fig. 8. (a) Schematic of a typical nano-indentation test. A hard tip whose mechanical properties are known is punched into the test specimen. From the applied load and the depth of penetration, the load-displacement curve can be created. (b) Example of an indentation mark in a fused silica substrate [27].

The relationship among the unloading stiffness, K_u , and A , E is given by:

$$K_u = 2\beta E_r \sqrt{\frac{A}{\pi}} \quad (1.3)$$

where β is a constant depending on the geometry of the indenter tip. $K_u = dF/dh$ can be obtained from the slope of the initial portion of the unloading curve. Here, h is the indentation depth, E_r is the reduced elastic modulus that accounts for the fact that elastic deformation occurs in both the sample and the indenter, which is given by:

$$\frac{1}{E_r} = \frac{1 - \nu^2}{E} + \frac{1 - \nu_i^2}{E_i} \quad (1.4)$$

where E_i , and ν_i are the elastic modulus and Poisson's ratio of the indenter, and ν is the Poisson ratio of the specimen. From Eq. (1.4) one can estimate the elastic modulus of the material under test.

Although this technique is applicable to a wide range of materials, it suffers from a lack of direct link between the measured hardness and the uniaxial mechanical characteristics of the material being tested. The limited knowledge of the large stress and strong strain gradient formed under the indenter makes the data interpretation problematic [28].

ii) Three-points bending test

Three-point (or double clamped) bending test is one of the first techniques introduced for the study of the mechanics of thin films and membranes [29-31].

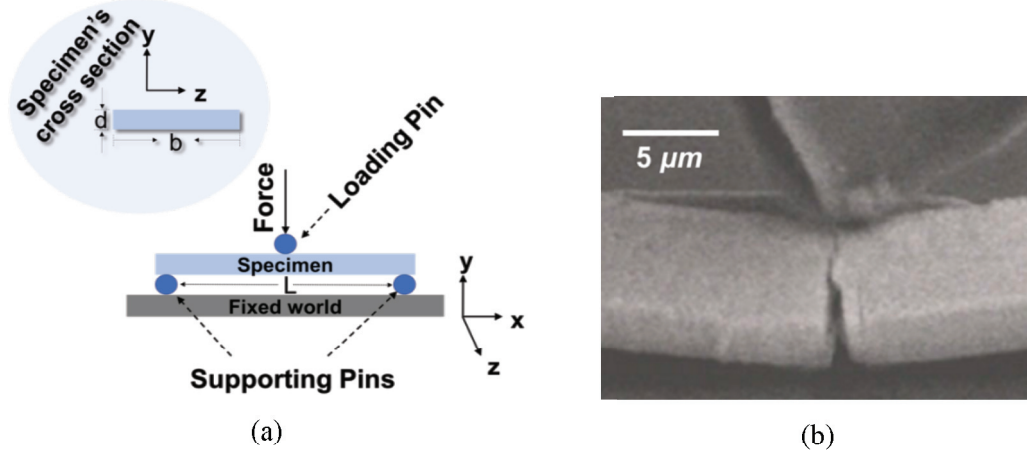


Fig. 9. (a) A typical three-point bending setup. The specimen with the rectangular cross section is placed between two supporting pins. A loading pin placed perpendicularly to the test specimen is applying a force. (b) Scanning electron microscope (SEM) image of a micron scale three-point bending experiment (image adapted from [32]).

In this test, a specimen with rectangular cross section is placed between two parallel supporting pins (Fig. 9).

The loading force is applied in the middle and perpendicularly to the specimen by a loading pin. The flexural stress σ of material under test can be calculated by [33]:

$$\sigma = \frac{3PL}{2bd^2} \quad (1.5)$$

and its elastic modulus E , from the following formula:

$$E = \frac{L^3 m}{4bd^3} \quad (1.6)$$

where m is the gradient of the initial straight line portion of the load deflection curve, b and d are the width and the thickness of the test specimen, respectively, L is the support span and P is the applied force.

For the case of micro-scale specimens, the implementation of three-points bending test requires an atomic force microscope (AFM) cantilever which is used to bend the test

specimen. The bending deformation is usually large enough to be evaluated using a scanning electron microscope [22].

An extension of this test is the four points bending test, where the volume of the material tested is spread over a larger area [34].

The main limitation of bending tests at small scales is the influence of interfacial effects due to the stress concentration developed at the boundaries [15]. This limits the stress level that can be reached. Furthermore, the manipulation and fabrication of thin membranes can be particularly difficult.

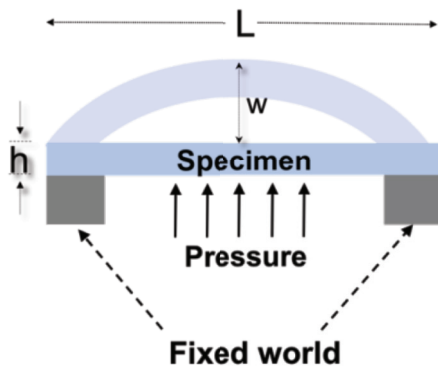
iii) Bulge test

In this test [36-40], a test specimen is clamped on two parallel supporting pins. Uniform pressure is applied, causing the specimen to deflect. From the measurement of the deflection as a function of the applied pressure, the stress-strain relation of the material is extracted.

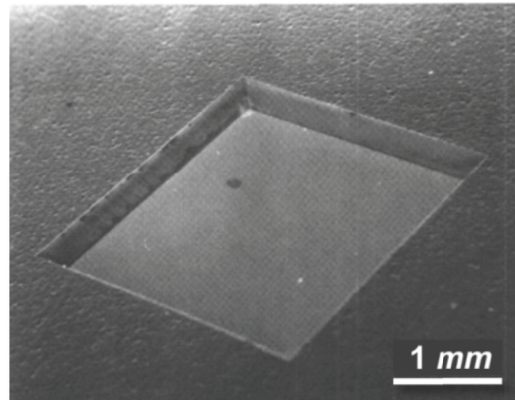
For the case of tensile loading of the specimen, the load deflection is given by [41]:

$$P(w) = c_1 \frac{\sigma_0 h}{L^2} w + c_2 \frac{Eh}{L^4(1-\nu)} w^3 \quad (1.7)$$

where P denotes the differential pressure, E the elastic modulus of the material, σ_0 the residual stresses of a square film, L the membrane width, h the film thickness, w the deflection and ν the Poisson's ratio as shown in Fig. 10a. The coefficients c_1 and c_2 depend on the sample geometry.



(a)



(b)

Fig. 10. (a) Illustration of a bulge test setup. The test specimen is placed between two supporting pins. Uniform pressure is applied to the one side of the specimen. (b) Scanning electron microscope (SEM) image of a silicon nitride window (SiN_x) test membrane [41] in a silicon wafer.

Similarly to the three-points bending test, this technique suffers from the stress concentration developed at the boundaries of the specimen, eventually limiting the stress level that can be tested. Furthermore, the fabrication of glass membranes is challenging. For the case of fused silica, membranes could be realized by thin film growth methods. Nevertheless, using this fabrication technique, the testing would be limited to ultra-thin membranes.

iv) Mechanical resonance test

Mechanical resonance is a non-destructive testing technique that is based on beam theory. It can be used to obtain the elastic modulus of micro-scale specimens (Fig. 11) by mechanical or electrical field excitation [42-46].

Mechanical resonance of the test specimen is achieved when the frequency of the periodic excitation approaches the resonance frequency of the specimen. Assuming small oscillation amplitude, the relationship between the first resonance frequency and the elastic modulus of the material in a low damping environment is given by the Euler-Bernoulli equation [47]:

$$f = \frac{1.8 D}{8\pi L} \sqrt{\frac{E}{\rho}} \quad (1.8)$$

where f is the first resonance frequency, ρ is the density of the material, E is its elastic modulus, D and L are the test specimen's thickness and length, respectively.

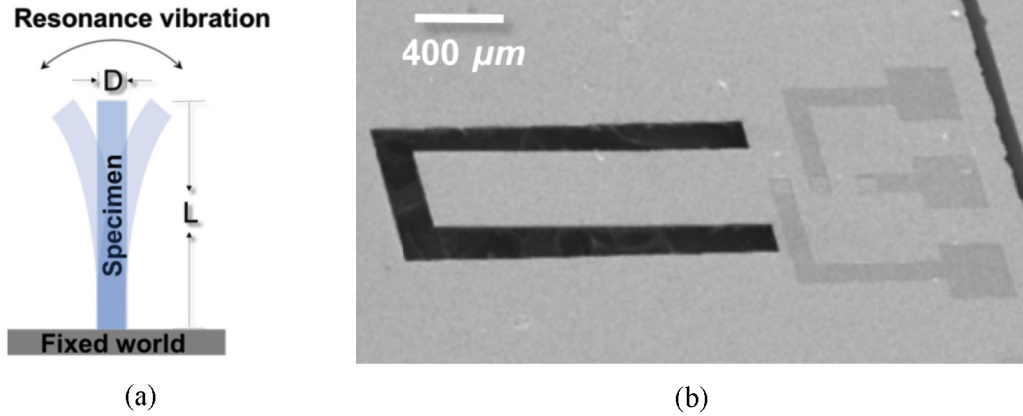


Fig. 11. (a) Illustration of a single clamped beam excited by a periodic force close to its resonance frequency. (b) SEM image of the mechanical resonance test in the micro-scale using piezoelectric cantilevers [48].

This technique is more specialized and has limited use since it can be used only to measure the elastic modulus of the test specimen.

v) Micro-scale tensile testing

Tensile testing of freestanding materials is the most established way of testing materials' mechanical properties [33, 49]. Micro-tensile testing is a natural extension of the classical macroscale tensile tester. In a typical tensile test, the test specimen is subjected to controlled axial load as shown in Fig. 12a.

In this technique, loads and displacements are measured independently, and no mathematical assumptions are needed to extract the material's uniaxial stress-strain response. Therefore, the data analysis of this technique is particularly straightforward. Various micro-tensile testing schemes have been proposed so far [22, 50-54].

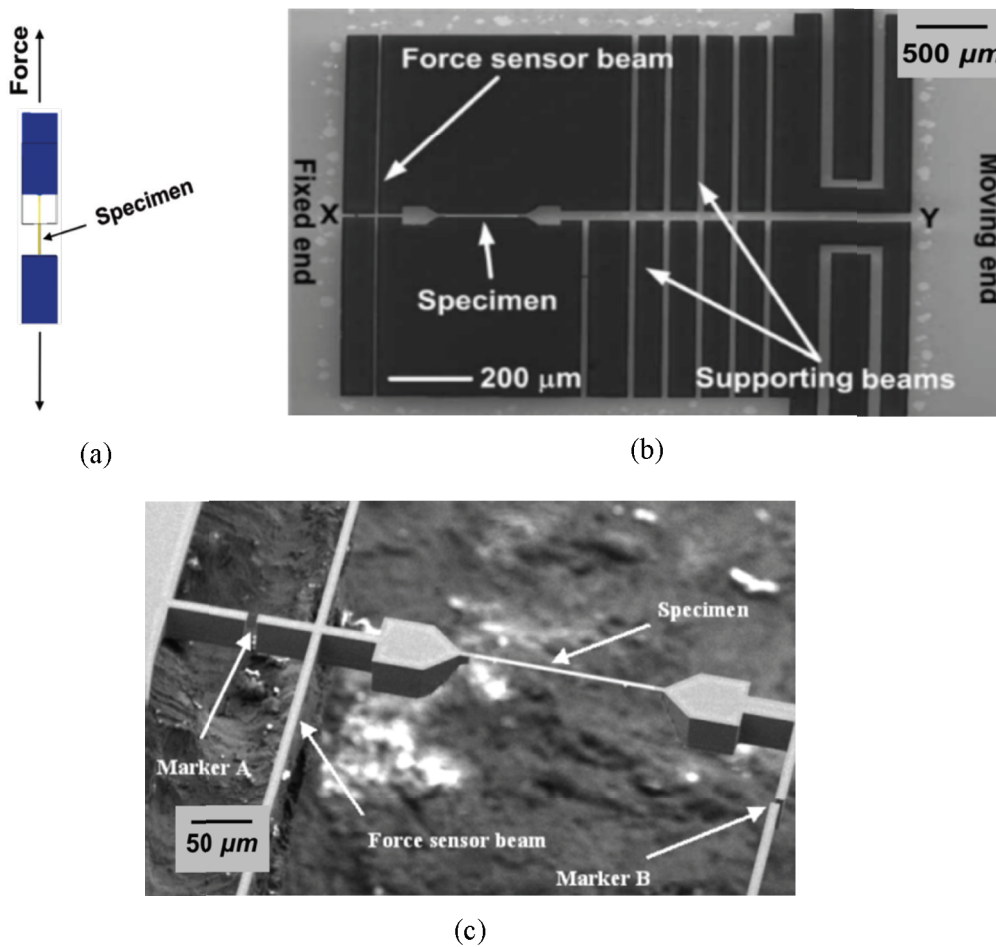


Fig. 12. (a) Schematic illustrating the principle of tensile testing. Controlled axial load is applied to a test specimen. The induced stress and strain on the specimen are measured. (b - c) Scanning electron microscope (SEM) images of one of the first micro-tensile testers developed by Saif's group in University of Illinois at Urbana-Champaign (UIUC) [50]. The device utilizes flexures beams for alignment and force measurement, and can perform *in situ* tests either in a SEM or in a transmission electron microscope (TEM) chamber.

In Fig. 12b one of the first micro-tensile testers developed by Saif's group in University of Illinois at Urbana-Champaign is shown [50]. The actuation principle is piezoelectric. The double-clamped beams are used as a force sensor. Several supporting beams located between the piezo-actuator and the specimen are designed to cancel off-axis loading of the externally applied displacement through a piezo actuator. The device is operated inside a scanning electron microscope chamber which makes the specimen manipulation and alignment cumbersome and time-consuming.

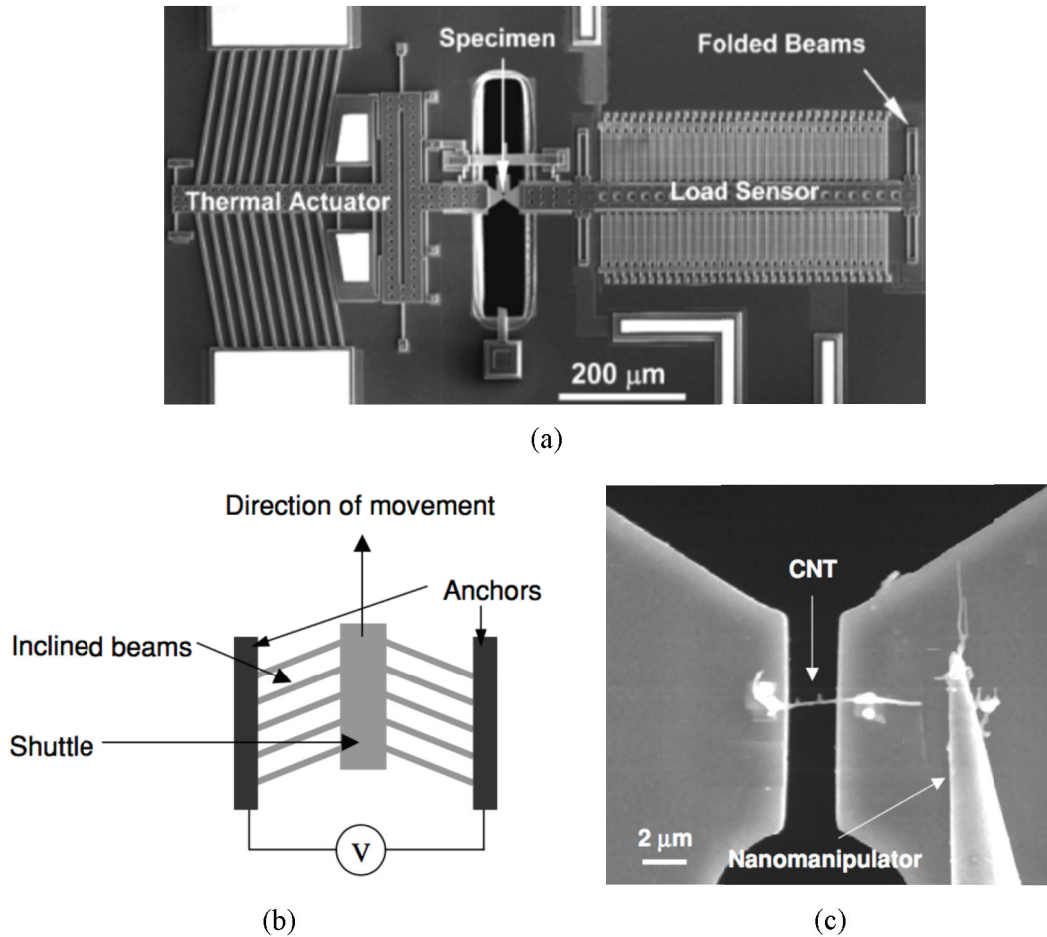


Fig. 13. (a) Scanning electron microscope image of a micro-tensile tester based on thermal actuation. The device consists of a thermal actuator, a load sensor and the test specimen [55]. (b) Schematic of the loading process. (c) Close view of the test specimen, mounted on the device by a nano-manipulator.

Lu *et al.* [56] and later Zhu *et al.* [55], designed nano-tensile testers based on thermal actuation. In Fig. 13, a nano-tensile stage consisting of a thermal actuator and a flexible beam force sensor is shown. Integrated motion amplification structures (V-shaped compliant beams in Fig. 13b) are incorporated to increase the range of motion. A capacitive sensor is integrated to measure the load electronically. The advantage of thermal actuators is their large stiffness in comparison to the electrostatic actuators. As a result, they can provide higher actuation force. However, special care needs be taken against the possible heat conduction to the specimen and the out-of-plane displacements of the thermal

actuator. These effects can be eliminated by integrating micro-heat sinks and optimizing the device geometry as discussed in [55].

Despite the remarkable progress that has been made in micro- and nano-scale tensile testing over the last decade, the performance of such tests remains a challenging task. Difficulties mainly arise from specimen fabrication, manipulation, and mounting. An additional challenge is the application of controlled displacements in a highly accurate, yet reproducible, manner. Moreover, the existing micro-tensile testers are operated within SEM chambers, which adds additional technical challenges such as to ensure vacuum compatible wiring [49] and require clean room facilities to be fabricated.

E. Thesis objectives

The main objective of this thesis is to develop novel methods for investigating the mechanical properties of glass in the micro-/nano- scale. In particular, material properties such as ultimate tensile stress (UTS), statistical fracture mechanics (SFM), and mechanical behavior over time under high constant load need to be investigated.

The development of such technology is *essential* from both a fundamental and a technological point of view to:

1. Help us understand the fracture behavior of fused silica in the micro- and nano- scale as well as related scaling phenomena.
2. Study the long-term mechanical stability of fused silica under constant load in different environmental conditions.
3. Identify possible mechanical effects in the interaction of femtosecond lasers with glass, and therefore, optimize the laser parameters to avoid cracks, and maximize etching.
4. Provide designers with the necessary guidelines to predict phenomena such as mechanical failure or mechanical relaxation of the glass.

F. Thesis outline

In this *introductory chapter*, we reviewed the state-of-the-art methods of mechanical characterization of materials at the micro-scale. The possible advantages and drawbacks of each one of them were highlighted. We concluded that none of these methods can be efficiently applicable for the case of femtosecond laser processed fused silica mechanical testing.

In the *second chapter*, a monolithic micro-tensile tester tailored for the exclusive requirements of micron scale glass testing is realized [57]. The design methodology, fabrication process, operation, and characterization results of the micro-tensile tester developed are presented and discussed in detail. Furthermore, the Weibull statistical failure results of fused silica using this instrument are presented.

The *third chapter* deals with the investigation of stress relaxation phenomena and delayed failure of fused silica at the micro-scale. Using the micro-tensile tester presented in the previous chapter, we perform long-term stress monitoring experiments in different environmental conditions and various tensile stress levels.

In the *fourth chapter*, based on the observations of self-organized nano-scale patterns alternating with chaotic ones, we investigated the formation of nano-scale patterns (nanogratings) at the surface of fused silica upon femtosecond laser exposure. We incidentally discovered a correlation between the formation of these patterns and the mechanics of fused silica *per se*. The mathematical modelling as well as experimental results proving that this method may be used to extract fracture statistics is presented [58].

The *fifth chapter* presents a polarization device, highlighting the importance of the knowledge on silica mechanics provided in the previous chapters from the technological point of view [59].

The *last chapter* brings together all the results of this thesis along with discussion and recommendations for future research.

Chapter II - A TENSILE TESTER TO INVESTIGATE FUSED SILICA FRACTURE MECHANICS

Based on the publication:

C.-E. Athanasiou and Y. Bellouard, "A Monolithic Micro-Tensile Tester for Investigating Silicon Dioxide Polymorph Micromechanics, Fabricated and Operated Using a Femtosecond Laser" in *Micromachines*, vol. 6, no. 9, pp. 1365-1386, 2015.

A. Introduction

In Section 1A, examples of devices made out of a single piece of fused silica were presented. The scale of the mechanical flexures in the devices (ranging from a few micrometers to a few millimeters) is illustrating the scale of specimens that need to be tested.

Among the existing mechanical testing methods, the most suitable that can provide all the required information -including long-term mechanical behavior- is the micro-tensile testing method.

In Section 1D, the advantages and limitations of the existing micro-tensile testers were discussed. Due to the complexity of their fabrication and operation in combination with the mechanical properties of fused silica *per se* (discussed in Appendix A), we concluded that none of them was particularly suitable for testing glass at the micro-scale.

To fill this need, a new instrument specifically designed to test the mechanical properties of fused silica is presented in this chapter. The development of such an instrument requires (Fig. 14):

- An *actuation* (loading) principle for applying a controlled force on the test sample.
- A proper *guiding mechanism* to ensure uniaxial loading conditions.
- Measurement of the generated specimen's *deformations* with nanometer resolution [3, 60, 61].
- Diagnosis of the developed *stress* in the specimen with a resolution of a few megapascals (MPa).

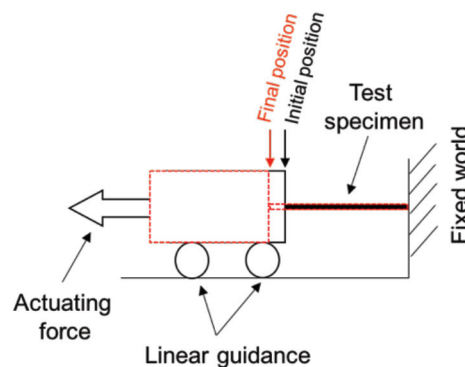


Fig. 14. Functional diagram of a tensile test. An actuation force is required. Once the force is applied to the test specimen, guidance is needed to ensure the uniaxial directionality of the force. Only stress and strain need to be measured in the elongated specimen.

B. Femtosecond lasers as a means to manufacture and load fused silica devices

Femtosecond lasers were developed around the 1980s. They provide pulses from a few femtoseconds ($1 \text{ fs} = 10^{-15} \text{ s}$) to several hundreds of femtoseconds. So far, these lasers were mainly used in research to investigate ultrashort-time phenomena. However, more recently they have been proven to be a powerful tool for manufacturing devices both at the micro- and the nanoscales [62]. The main difference compared to other laser-based manufacturing processes that use longer pulses (i.e., nanosecond lasers) or continuous wave lasers (i.e., CO_2 lasers) is that the femtosecond lasers offer a radically different laser-matter interaction (Fig. 15).

Femtosecond pulses confine energy in extremely short pulses and when tightly focused within a small volume. Consequently, ultra-high peak power is locally reached (for example focusing a 300 fs laser in a spot size of $2 \times 2 \mu\text{m}^2$ leads to irradiance level as high as 10 GW/cm^2). As a result, non-linear absorption phenomena are triggered starting with multi-photon processes, which ultimately induce permanent structural changes in the material [63, 64]. Owing to the nonlinearity of the process, a high spatial resolution interaction beyond the diffraction limit can be achieved. As another consequence of the non-linearity of the interaction, femtosecond laser manufacturing intrinsically provides the capability of three-dimensional (3D) manufacturing with versatility in terms of materials that can be processed [4, 5, 65-69].

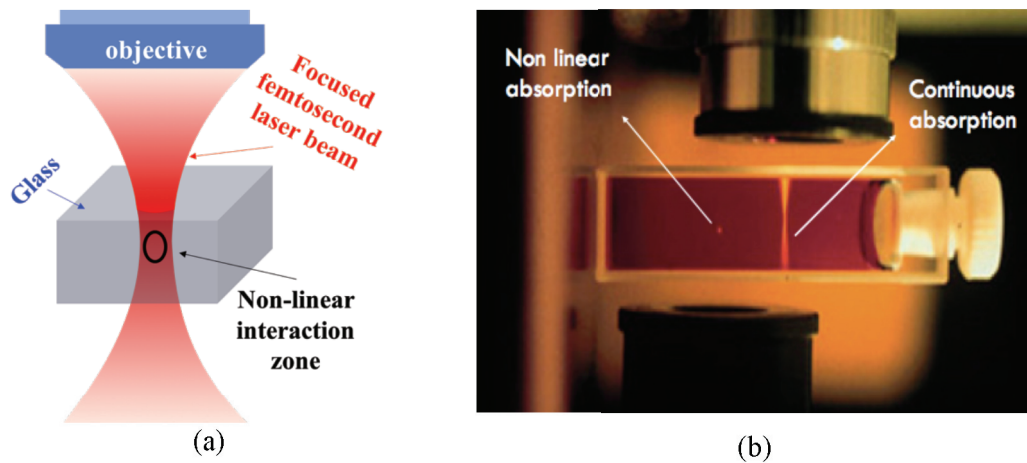


Fig. 15. (a) Illustration of the nonlinear process affecting a confined zone in the bulk of the material. (b) Image demonstrating the two radically different types of laser-matter interaction. On the right part of fluorescent dye the effect of continuous absorption is captured, while on the left part the confined nonlinear absorption zone is shown (Source: Amos at the University of Strathclyde [70]).

In the two following subsections, we will discuss the manufacturing and loading capabilities of femtosecond lasers in the context of the development and operation of a micro-tensile testing device.

i) Micro-manufacturing

Femtosecond laser micro-manufacturing takes place as follows: a femtosecond laser beam is focused on the surface of a material or within its volume (in our case fused silica); by scanning the beam or by moving the specimen under the beam, the material can be locally modified (Fig. 16). The manufacturing principle is depicted in Fig. 17.

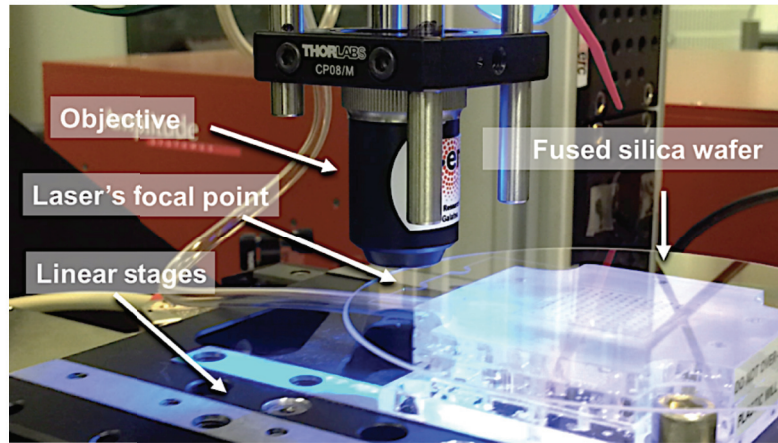
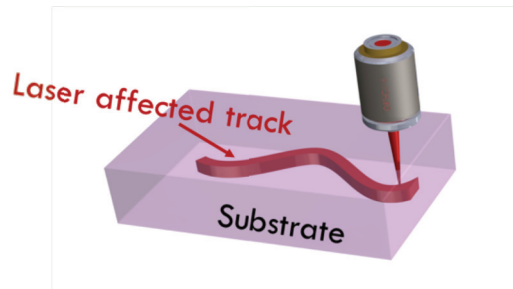


Fig. 16. Illustration of the setup used in this thesis for fused silica machining. The stages on which the silica wafer is mounted have two-degree of freedom (vertical and lateral in the wafer's plane), while the objective is mounted on a vertically moving stage. With these three degrees of freedom, the laser spot can follow three-dimensional (3D) trajectories within the volume of fused silica.

Step 1/ Femtosecond laser exposure (no ablation)



Step 2/ Chemical Etching (low concentration HF bath)

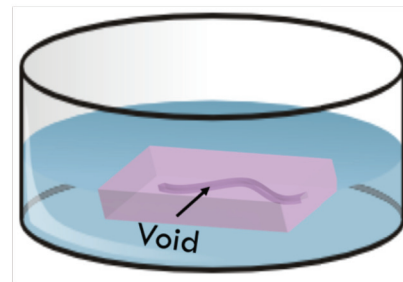


Fig. 17. Illustration of the two steps of the femtosecond laser micro-manufacturing process [71]. On the **left** schematic, the laser (or the substrate) moves while being tightly focused on the surface of the material (Step 1). The red track represents the volume of the laser-modified material. The etching step (Step 2) of the process is illustrated on the **right** schematic. Once modified by the laser the material is put in an HF bath. As a result, the laser modified zones (red track in the left image) have been dissolved producing the final structure.

A subsequent wet chemical etching step is used (in our case hydrofluoric acid – HF [72]), to dissolve the laser modified zones accessible to the acid [71, 73]. Following etching, the sample is rinsed in de-ionized water and dried.

The parameters affecting the laser process are the polarization of the laser beam with respect to the scanning direction, the repetition rate, the numerical aperture of the objective, and the pulse energy. A detailed discussion on how they affect the micro-manufacturing process can be found in Appendix C.

This two-step subtractive process can provide an out-of-the-cleanroom manufacturing method to fabricate a tensile testing device at the desired scale.

ii) Stress manipulation

Previous studies have shown that femtosecond laser pulses under certain energy deposition parameters can induce volume changes in fused silica [74, 75]. In this thesis, we make use of these volume variations to accurately apply forces in certain parts of the microdevice.

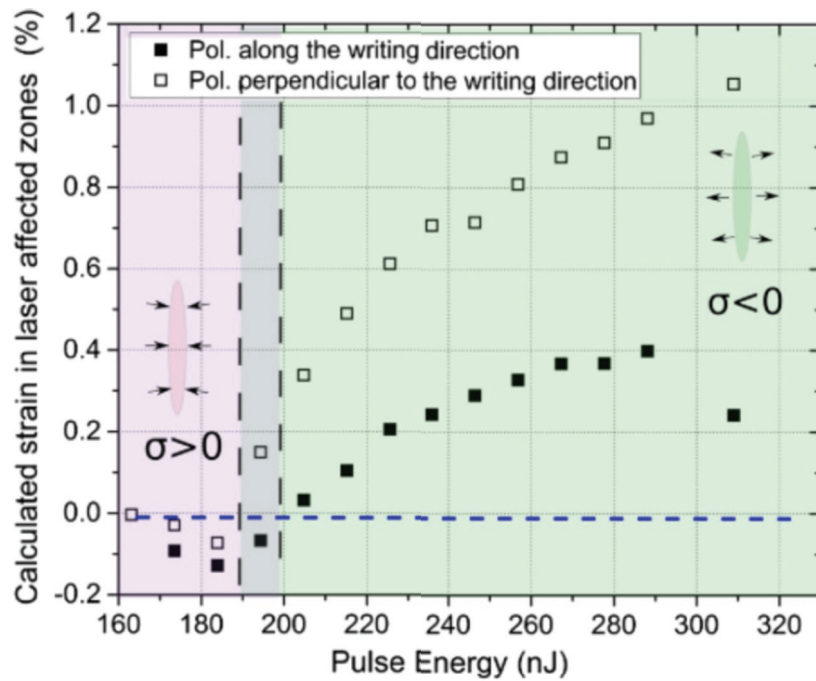


Fig. 18. Strain induced in the material volume exposed to the laser as a function of laser energy deposition [76]. The deposited energy was tuned by varying the writing speeds. Interestingly, both compressive and tensile strains can be achieved.

The order of magnitude of these modifications strongly depends on the exposure parameters (further discussion in Chapter IV) but typically is in the order of 0.01% to 0.05%. In Fig. 18, the induced strain of a laser-exposed line in fused silica is plotted according to the energy deposition. The work on the underlying physical mechanisms explaining the volume densification and expansion can be found here [76].

The confined volume variations inside the bulk of the material can be used as a loading tool to avoid electrostatic or thermal actuation and their associated manufacturing challenges.

C. Micro-tensile tester design and working principle

By making use of the femtosecond laser micromanufacturing and loading principles, we present a monolithic tensile tester for investigating fused silica's mechanical response, fracture mechanics and load-term behavior under constant load.

The instrument is entirely fabricated out of a single piece of silica glass by a femtosecond laser. The *same* femtosecond laser that is used to fabricate the instrument is also used to operate it (load the specimen) as well as to perform *in situ* measurements (strain measurements). The stress is measured using photoelasticity.

The contactless manufacturing and characterization methods used allow the material's testing without any mechanical interaction with the test specimen.

i) Micro-scale tensile testing

The device is fabricated using a two-step femtosecond laser-based process described in the previous subsection as well as in [71]. Firstly, the silica substrate is exposed to low-energy femtosecond laser pulses. As a result, the material structure is locally modified, causing an accelerated etching rate in laser-exposed regions [71]. The follow-up etching step is performed in a low concentration hydrofluoric HF bath (2.5%).

In the previous subsection, we demonstrated that laser-affected zones in silica exhibit a net volume expansion (Fig. 18) [75]. We use this principle to expand the lateral bars in a controlled manner by juxtaposing laser-affected zones consisting of lines written across the volume. To mechanically load the specimen, we re-expose the two transverse bars (part 1 and 2 in Fig. 19a) to the same femtosecond laser. Fig. 19b further illustrates the loading process. We call these laser-affected structures, "stressors".

To measure the beam elongation resulting from the stress load (typically a tenth, to a few % of the beam length), the displacement is mechanically amplified using a two-stage flexure-based lever mechanism (part B in Fig. 19a) connected in parallel to the main load cell. When a load is applied, the load cell induces a mechanical moment on the flexure that rotates, causing an amplified displacement of the lever. The kinematics and working principle of this amplification mechanism are further discussed in the next paragraphs.

Finally, with the use of the same laser, yet at much lower pulse energy, so that no further modification is made to the material we measure the displacement of the lever amplification beam (Fig. 19d) using the third harmonic optical signal generated while scanning the beam across the specimen's surface [77-81].

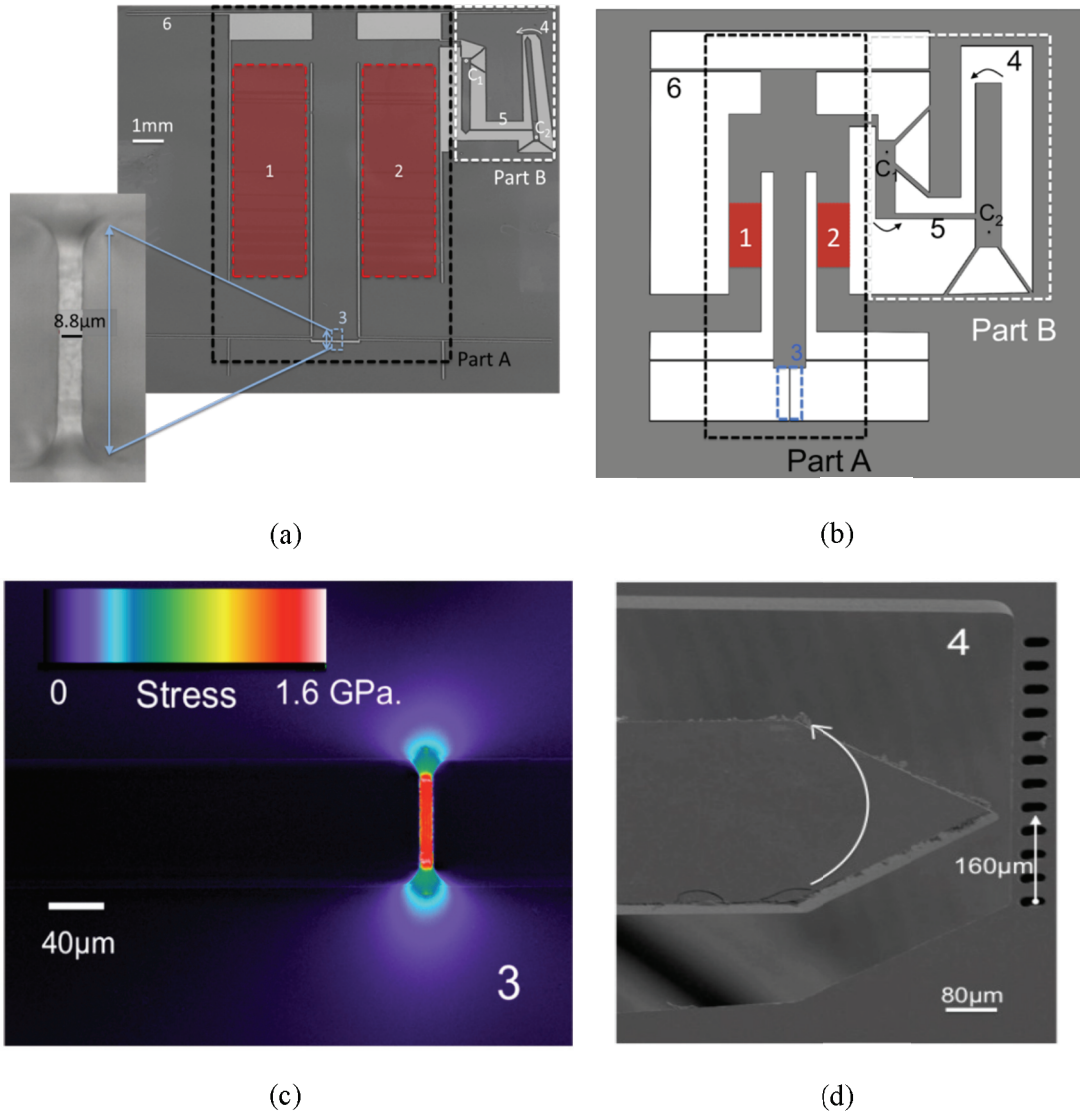


Fig. 19. (a) Monolithic micro-tensile tester seen through an optical microscope. The overall dimensions of the system are $15\text{ mm} \times 15\text{ mm}$. Part A is the loading cell and part B is the displacement amplification sensor. The test beam (#3 in part A) is also shown magnified in the inset. (b) Graphical representation of the micro-tensile tester. Note that the dimensions of the device used here are not the real ones, but were chosen for a clearer understanding of the device's operation. (c) Photoelasticity image of a test beam. (d) Magnified view of the system's displaced lever beam as seen in an SEM.

The five steps of the process of the device manufacturing, operation, and characterization are summarized in Fig. 20. The fact that none of the techniques used requires physical interaction with the test specimen sets the scene for a novel instrument able to test mechanical properties contactless.

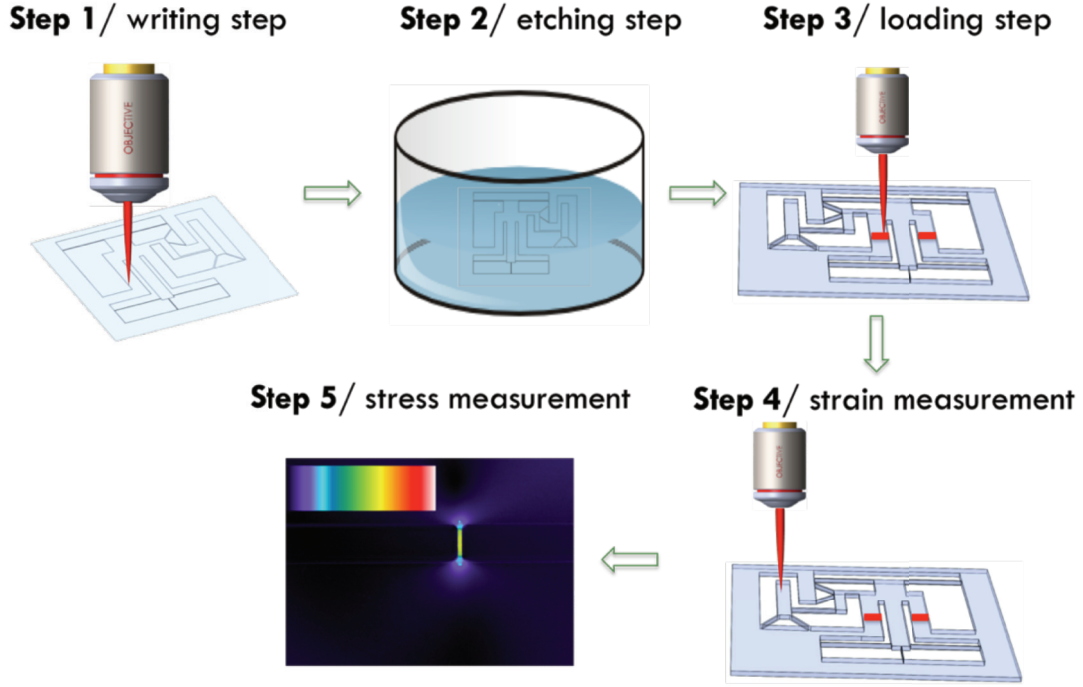


Fig. 20. Schematic illustrating the five steps followed for the device manufacturing, operation, and characterization. All the methods used are contactless allowing a full tensile test to be performed without any physical interaction with the specimen. Following this approach, we overcome manipulation and alignment challenges of the micron scale brittle specimen.

ii) Test beam dimensioning and loading cell

In this section, we evaluate the stress in the test beam as a function of the number of laser-written lines defining the volume expansion of the load cell. Note that single laser-affected lines, for the energy level considered here [82] consist of an arrangement of periodic nanoplanes (nanogratings) [83-86] as illustrated in Fig. 21.

Let A_{LB} , A_{TB} be the cross-sections of the laser-exposed beams (“LB”) and the test beam (“TB”), respectively, and likewise, σ_{LB} and σ_{TB} the corresponding stresses in both beams. The stress in the test beam is expressed as:

$$\frac{\sigma_{LB}}{\sigma_{TB}} = \frac{A_{TB}}{A_{LB}} \text{ and } \sigma_{LB} = E_{LB}\varepsilon_{LB} \Rightarrow \sigma_{TB} = E_{TB}n\varepsilon_{LB} \left(\frac{A_{TB}}{A_{LB}} \right) \quad (2.1)$$

where ε_{LB} is the strain caused by the volume variation induced to the laser-affected beams, E_{TB} is the elastic modulus of fused silica, E_{LB} is the elastic modulus of the composite material formed in the fused silica matrix following laser-exposure, and n is the number of stressors induced in the system.

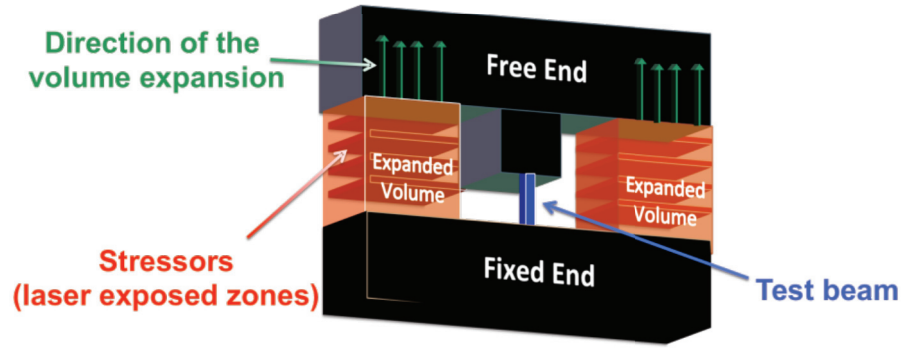


Fig. 21. Illustration of the loading cell's working principle. The two loading bars (red areas) expand during femtosecond laser exposure resulting in the loading of the middle (blue) test beam.

The volume of the material exposed to the laser is inhomogeneous and consists of a composite structure of modified and unmodified zones as shown in Fig. 21.

iii) Lever amplification mechanism

The displacements induced in the system are particularly small (a few tens of nanometers) to be detected accurately with common microscopy tools.

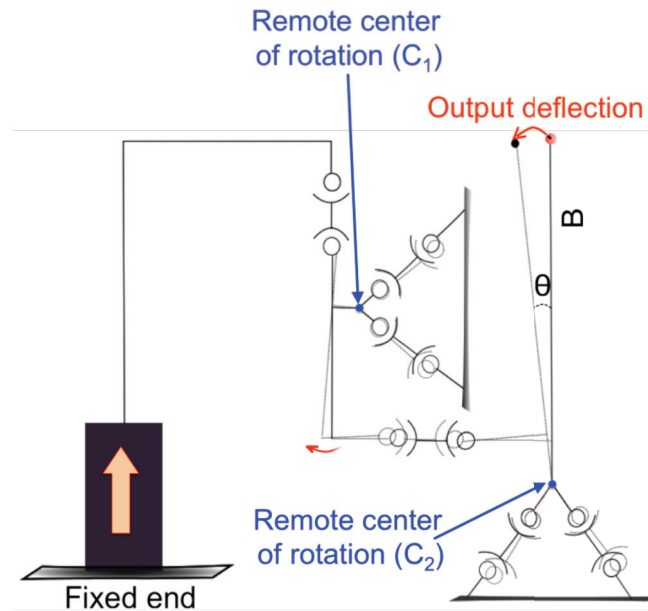


Fig. 22. Kinematics of the displacement amplification mechanism. The circles represent one-degree-of-freedom rotation pivot joints. The bars represent rigid links. The dash lines indicate the kinematics being operated. The end-effector is body B.

To measure the deformation resulting from the elongation of the test beam, we use a two-stage in-plane motion amplification mechanism.

The mechanism is itself equivalent to a slider-crank kinematic to convert the linear motion into a rotational one around a pivot point defined by a four-bar mechanism, defining a remote center of rotation. The lever amplification kinematics is depicted using pivot joints (Fig. 22). A lever pivots around a point (point C_1 in Fig. 22 and Fig. 23) anchored to a fixed body. Two bars (bars 1 and 2 in Fig. 23) fixed at their one end (from the kinematics point of view each bar is equivalent with two pivots) form a hinge, which is used to interface the linear motion of the actuator with the angular motion of the pivot.

The loading cell (illustrated as a dashpot in Fig. 22) forming the input of the mechanism is attached at one end while the output of the mechanism is at the other end of the lever (part B in Fig. 19a and magnified in Fig. 19d). The second stage of the amplification acts exactly like the first one, scaling up the input linear motion even more. The amplification level for small angles θ of the end-effector bar (Fig. 22) is the ratio of the output displacement of the mechanism and the input displacement induced in the system.

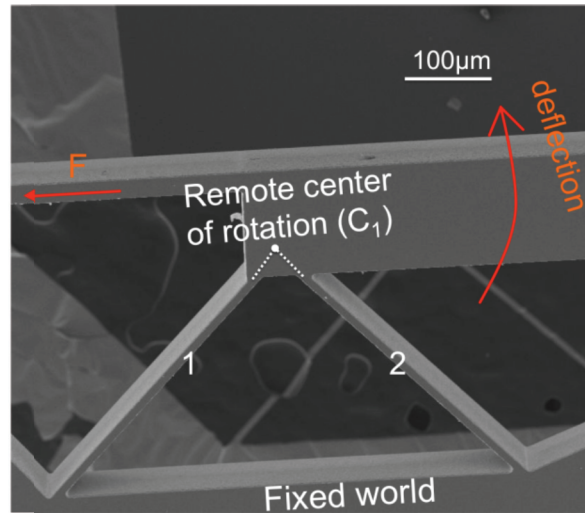


Fig. 23. Scanning electron microscope view of part of the displacement amplification sensor fabricated using femtosecond laser machining and chemical etching.

To meet the high-precision requirements and achieve a monolithic design, the kinematics is implemented using flexures. Flexures are commonly used in precision engineering to approximate kinematics using elastic elements since at least the 1920s (see, for instance, the work from Sears [87]). Modern treatises are numerous and the reader interested in the topic can refer to [88-91].

iv) Mechanical guidance

A mechanical guidance is needed to obtain uniform loading conditions on the test beam. Here, we implement it with four leaf springs of equal length (#6 in Fig. 19a), attached on

one side to the rigid element of the loading cell and to a fixed reference on their other end (as shown in Fig. 24a).

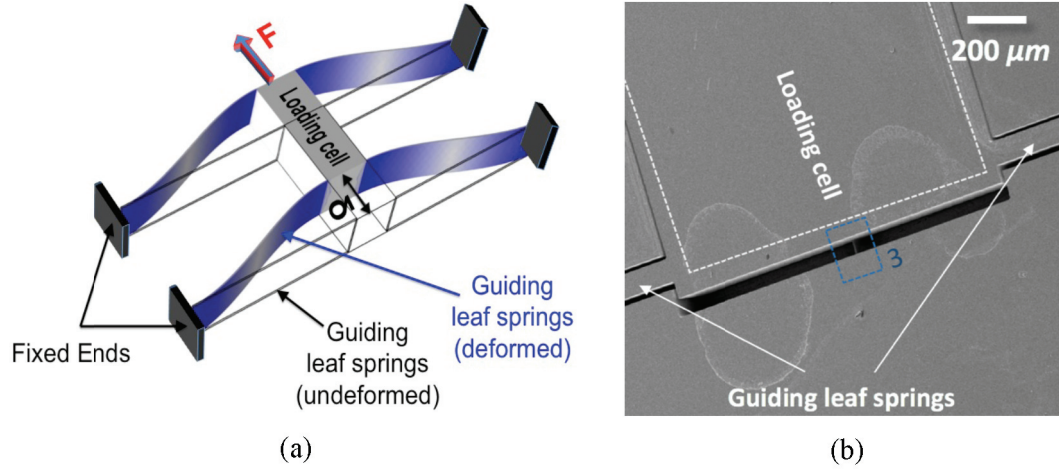


Fig. 24. (a) Mechanical guidance principle of the loading cell. Four leaf springs are used to limit the out-of-plane displacements. (b) Two of the four leaf springs of the device are shown in the SEM image. Part #3 is referring to Fig. 19.

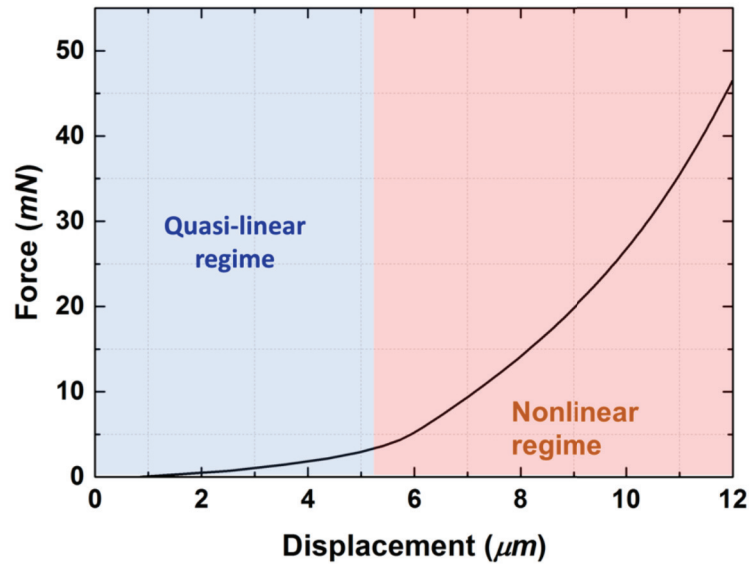


Fig. 25. The characteristic force-deformation curve of the guidance which consists of four parallel leaf-springs is shown here. The parameters ($w = 100 \mu\text{m}$, $l = 5000 \mu\text{m}$, and $t = 230 \mu\text{m}$) chosen for this graph correspond to the parameters of the fabricated device shown in the previous Fig. 24. Here, the guidance is used in its quasi-linear regime.

This construction allows for a rectilinear movement of the loading cell, albeit with a non-linear stiffness (Fig. 25). The force-displacement relationship of this system is given by [91]:

$$F \approx \frac{6wtE_{\text{SiO}_2}\delta^4}{3\delta l^3 - \sqrt{6}wl^3 \coth\sqrt{\frac{3}{2}}\left(\frac{\delta}{w}\right)} \quad (2.2)$$

where δ is the displacement of the loading cell from its initial position, w is the width, l is the length, and t is the thickness of the guiding flexures. A double-compound flexure [1] could also be used to achieve rectilinear motion with a linear stiffness, but at the expense of occupying more real estate on the substrate and adding more complexity. The over guided-one used here is a compromise between linearity *versus* volume required. Although this guiding mechanism is not linear, we bypass this issue by using it in its quasi-linear regime (Fig. 25), since the displacements are extremely small.

D. Experimental results

i) Manufacturing

Our experimental setup consists of a femtosecond laser, positioning stages and a 250 μm thick silica substrate. The laser (Amplitude Systèmes, Bordeaux, France) emits 275 fs pulses at 1030 nm from an Yb-fiber amplifier operating at 800 kHz. The laser beam is focused using a 20 \times objective (OFR-20X-1054, Thorlabs, NJ, USA) with a numerical aperture (NA) of 0.40. The linear positioning stages, on which the specimen is mounted, provide three degrees of freedom with a resolution of 0.1 μm and a repeatability of 0.2 μm at the operated speeds.

For the fabrication of the device, a scanning speed of 12 mm/s with pulse energy of 250 nJ is used. The complete exposure step lasted approximately two hours. After laser exposure, the device is etched for twenty-four hours in HF – twelve hours are essentially needed for the laser affected zones to be totally etched out; we let the device in the bath for another twelve hours to achieve better surface quality and therefore enhance mechanical strength [60].

The re-exposure of the specimen to induce the desired volume variation is implemented by scanning adjacent lines with a writing speed of 10 mm/s and with energy per pulse of 220 nJ. The re-exposure step requires approximately eight hours.

For the device fabrication, circular polarization is used while for the re-exposure step linear polarization perpendicular to the scanning directions is applied (so that the highest possible volume variation for the given pulse energy is induced [61, 75]).

It should be noted that the process was not optimized for speed, and the manufacturing time could be significantly reduced (by an order of magnitude), for instance, by using higher writing speeds and/or repetition rates [92].

ii) Loading scheme optimization

The same mechanism used for the amplification of the strain in the tensile tester is also used for the quantitative evaluation of the loading process.

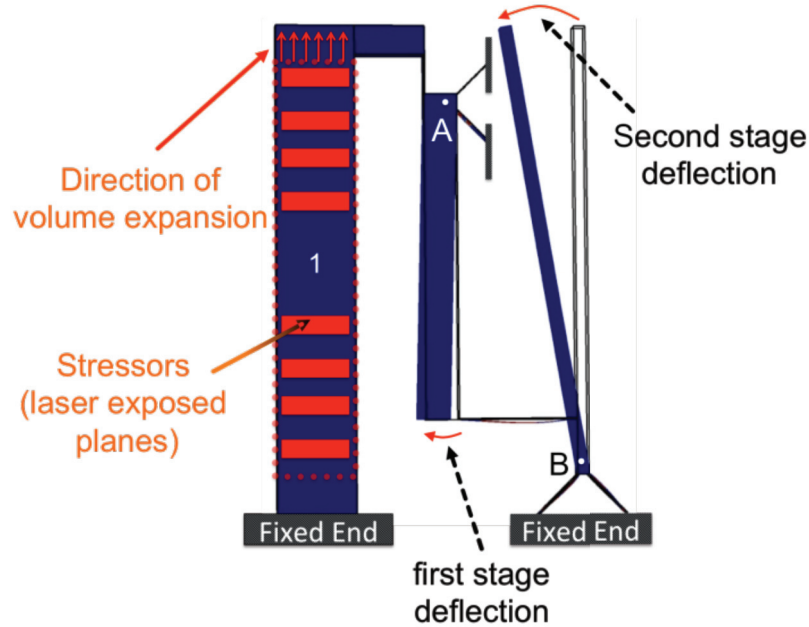


Fig. 26. A simulation of the deformed system is illustrated. The same mechanism used for the amplification of the strain in the tensile tester is also used stand-alone (attached only to bulk fused silica-bar 1) for the quantitative evaluation of the loading process. The red boxes in bar 1 represent the stressors.

This time, the mechanism is not attached to the load cell but to bar 1 (Fig. 26). Upon the writing of stressors, the response of the mechanism is studied. From this response, the induced displacements can be quantified.

The in-plane response of the mechanism is shown in Fig. 27. The volume variation values observed range between 0.11% and 0.05% and are consistent with the values previously reported in the literature for similar exposure conditions [39].

Based on these values we are able to estimate the displacement for a single stressor to be in nanometer range and more specifically 1 - 2 nm [41], which is essentially the resolution of the loading process.

The nonlinear response lead us to investigate possible out-of-plane actuation in the loading process that would be detrimental for a pure tensile test shown in Fig. 14. Indeed, as illustrated in Fig. 28, we observed a significant out-of-plane motion of the system. The profile of the moving bar (bar 1 in Fig. 26) revealed that 60% of the induced volume variation in the system was allocated to undesired out-of-plane displacement. Nevertheless,

the saturation values of volume expansion obtained after machining a number of stressors, originates in the stiffness of the stressors/loading bar assembly and is investigated in our paper [57].

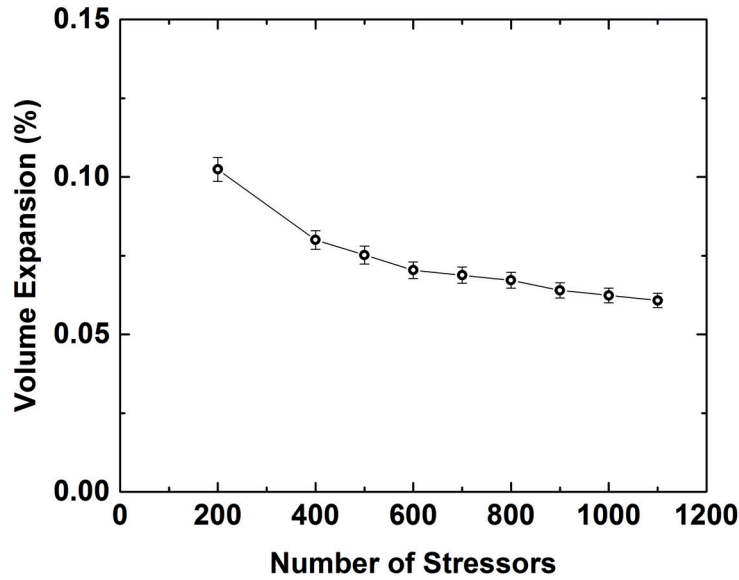


Fig. 27. In-plane volume variation (laser exposed planes) measurements for two exposure cases based on the elongation results measured with the two-stage amplification sensor (Fig. 27). These results are consistent with previous data where expansion in the order of magnitude of 0.01% - 0.05% is reported [61, 93].

To investigate the origin and eliminate the out-of-plane motion upon femtosecond laser machining in bulk fused silica, we use a method based on the deflection of micro-cantilevers [33, 34]. The working principle is outlined in Fig. 29. A cantilever, entirely made out of fused silica, is exposed locally to a laser beam, but only close to its anchoring point, and only in the upper part (just below the surface, so that the surface remains continuous and unaffected). In the cantilever portion exposed to the laser beam, the modified zones and the unaffected layers form a bimorph composite structure.

When a volume expansion occurs in the laser-affected zone, the bimorph element will bend down. Essentially, the bimorph zone forms a hinge. The cantilever arm amplifies any resulting displacement providing a simple and efficient method for increasing the variation's measurement range and achieving high-resolution measurement of laser-induced volume changes.

The fabrication parameters used are the same as the ones used to fabricate the tensile tester device are used. The etching step lasted twenty-five hours. The cantilever exposure is made by scanning adjacent lines (going back and forth) with $2 \mu m$ spacing. The amplification ratio for the dimensions of the cantilevers in this experiment ($L \times W \times D$) $20 mm \times 0.5 mm \times 0.25 mm$ is one-hundred-twelve (112) times.

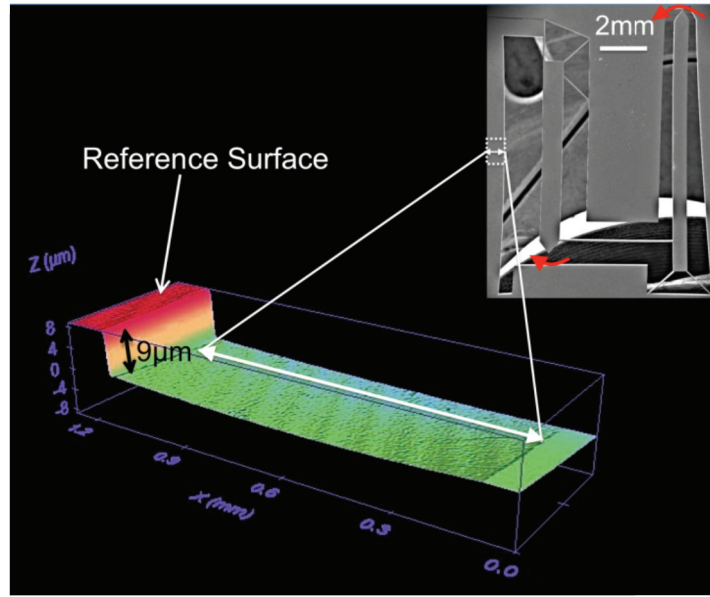


Fig. 28. Using white light interferometry for measuring the profile of the deformed stressed zone, a significant out-of-plane motion was found. A scanning electron microscope image of the device is shown on the top right.

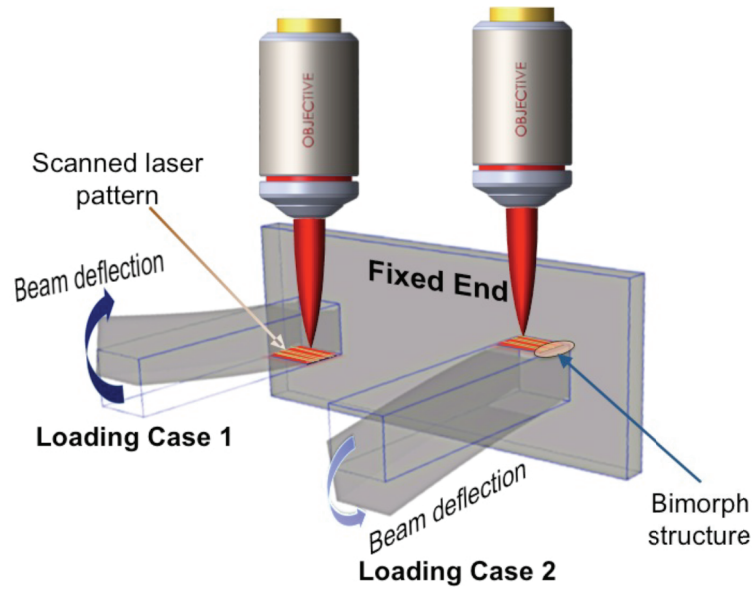


Fig. 29. Method for measuring laser-induced volume variation in fused silica using cantilever deflection. The laser exposure takes place only near the anchoring point of the cantilever and only in its upper-half thickness and forms a bimorph composite structure that induces local bending of the cantilever [75]. The deflection measured at the tip of the cantilever is effectively amplified by the length of the cantilever. The two different configurations result to different absolute values of induced volume variations, due to the spherical aberration effect.

The two different loading cases studied aimed at quantitatively evaluating the induced volume variation in the upper and the bottom part of the stressors in the bulk of the material.

The value of the strain is different for the two cases, as illustrated in Table 1, and is estimated by the relationship [94]:

$$\varepsilon(\delta) \simeq \left(\frac{d_s}{2w_{laz}} \right) \frac{\delta}{L} \quad (2.3)$$

where d_s is the thickness of the cantilever, w_{laz} is the width of the laser exposed area in a direction perpendicular to the cantilever, L is the length of the cantilever (measured from the end of the laser affected section to the tip of the beam), and δ is the deflection of the cantilever.

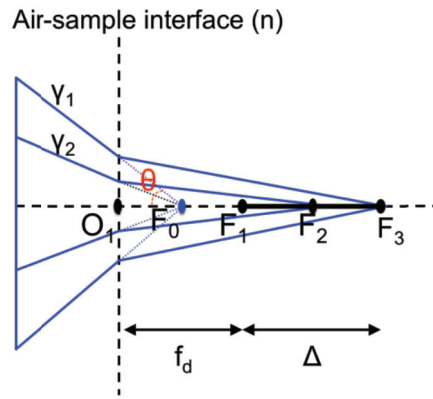


Fig. 30. A sketch showing the ray tracing for rays crossing a plane surface from air into the sample. O_1 is the crossing point of the light axis across the interface, F_0 is the geometrical focus in air, F_1 is the focus under the paraxial approximation, $f_d = |O_1F_1| = n|O_1F_0|$ is the focusing depth, F_3 is the focus of the marginal rays, and $\Delta = |F_1F_3|$ is the foci range (focal displacement) [95].

The deflections are measured using white light interferometry. The net volume variation induced by lines written at the bottom of the stressors is lower than the one induced by the one written at the top of the stressors, inducing a net bending moment.

For Given Exposure Conditions (NA), Pulse Energy + Writing Speed	Tip Deflection (μm)			Mean Value of the Volume Variation %
Loading case 1	42.0	41.5	42.0	0.0011
Loading case 2	53.0	52.5	53.0	0.0009

Table 1. Volume variation measured using the microcantilevers bending method. Three cantilevers were measured for each case. The error is considered negligible; the white light interferometry method has a resolution of a few tenths of nanometers.

The difference in volume variation observed between the two loading cases is attributed to a dispersion of the focus due to spherical aberration effects. In particular, as demonstrated in [95], the nonlinear interaction zone extends as the foci range, Δ , (Fig. 30) depends linearly on the focusing depth:

$$\Delta = \frac{f_d}{n} \left(\sqrt{\frac{n^2 - (NA)^2}{1 - (NA)^2}} - n \right) \quad (2.4)$$

where n is the refractive index of fused silica, NA is the numerical aperture of the objective, and f_d is defined as the focusing depth. This leads to lower intensity distribution in the laser-affected zone and finally a reduced volume variation.

By taking advantage of the difference in volume variation estimated by the cantilevers method, we optimize the shape of the laser-affected zones and achieve a uniform induced deformation to the system. Note that similar results that are acquired with the polygonal cross-sectioned stressors (Fig. 31) can also be reached by rectangular cross-sectioned stressors (as the ones applied in Fig. 21), as long as the laser power is modulated across the depth of the machined rectangle.

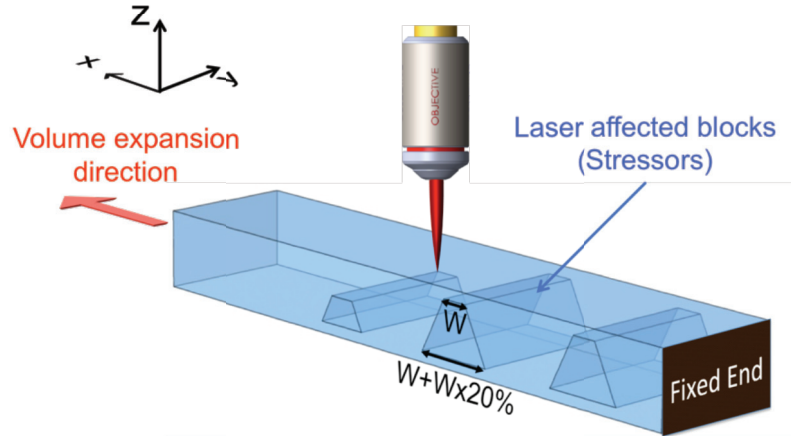


Fig. 31. Side view of the laser-affected bars that load the tensile tester. Optimized pattern structure of the sequential scanning of stressors for achieving uniform loading conditions.

The optimized pattern structure of the sequential scanning of stressors gives us the opportunity to refine the previously used loading scheme (discussed in Section C of this chapter) and avoid dealing with out-of-plane loading conditions.

iii) Third-harmonic generation (THG) as an *in situ* metrology tool

Various tools can perform spatial displacement measurements at the micro-scale. However, all the available techniques require repositioning of the device on the laser stages after each single measurement, which can eventually turn into a destructive process due to the difficulties when manipulating brittle micro-scale specimens. To overcome such

problems, the same laser as the one that fabricated and operated the device is used to measure the output displacements of the amplification sensor. Thanks to this method, the strain of the test beam is estimated without interacting mechanically with the specimen and without moving the tensile tester from the laser platform, after the stressors have been produced.

Third harmonic generation (THG) is a nonlinear process that occurs in all materials [96]. In general, THG is inhibited under tight focusing conditions because of a phase mismatch [96]. It is a surface-enhanced phenomenon due to its dependence on the different susceptibilities and/or refractive indices of the materials that form an interface. Its nature allows depth-resolved imaging and for this reason its use has been extensively reported for imaging and for obtaining structural information of a wide range of transparent materials from glass and laser-modified glass to biological specimens surface [77- 81].

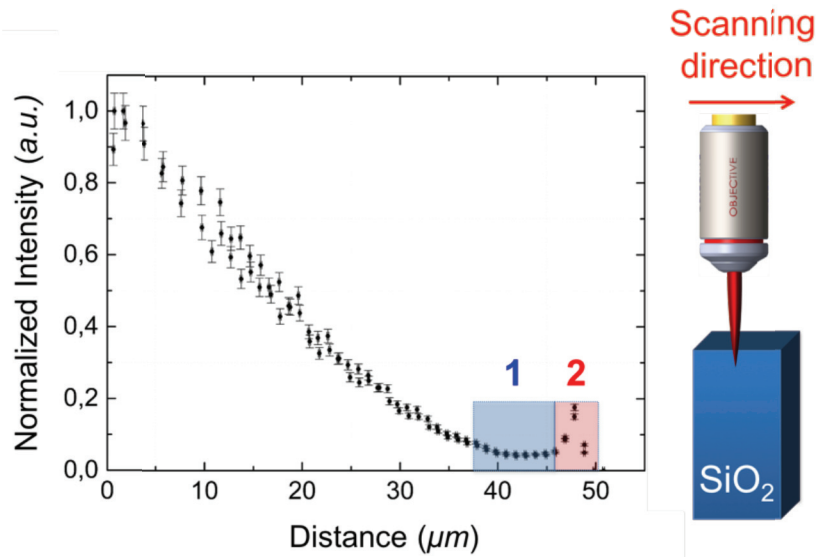


Fig. 32. Illustration of the formation of the third harmonic generation signal (THG) across the edge of a test sample. Regions one and two are close to the side edge of the material. In region one there is a decay of the signal, which is attributed to internal reflections. The spike in region two indicates reflection at the interface and thanks to it we can define the edge of the material.

Here, by taking advantage of the sensitivity of the THG process to interfaces, we adopt it for *in situ* metrology. For the measurements, the laser is operated at much lower pulse energy (energy per pulse of 70 nJ, 800 kHz), so that no modification is made in the material. Using the THG intensity peak (see Fig. 32) observed at air/material interfaces, we are able to define the edge positions. A proof-of-concept is given in Fig. 33 where predefined trenches of known spacial dimensions were fabricated in fused silica and were used to evaluate the THG measurement method. The measurement accuracy of this method is estimated to be less than 250 nm and in our case, depends on the laser spot size as well as the mechanical stages resolution.

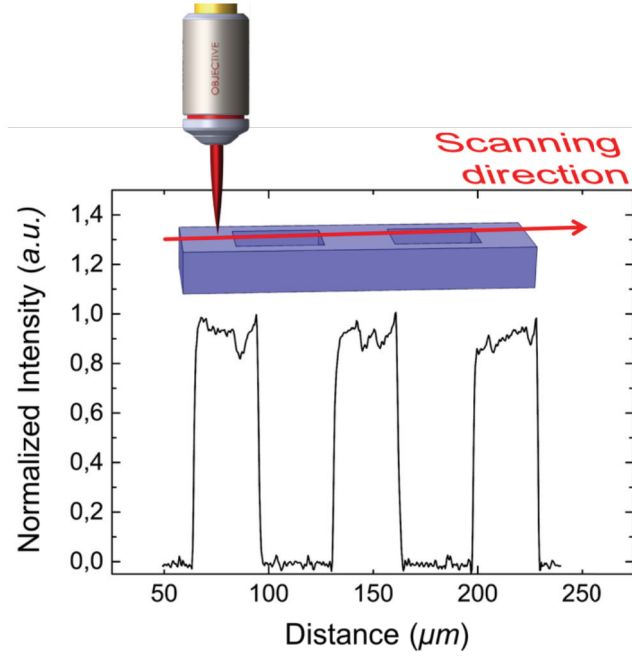


Fig. 33. Illustration of the THG signal across the surface of a calibration pattern made of known-size grooves.

iv) Stress monitoring through photoelasticity

Stress estimation is facilitated through photoelasticity, which gives a direct measurement of the induced stress in the test beam [27, 97]. False color intensity retardance maps (Fig. 19c) of the loaded test beam are generated with a standard microscope (Olympus BX51, Tokyo, Japan) fitted with a commercial system to measure optical retardance (LC-Polscope, CRI, Cambridge, MA, USA). The measured retardance of these patterns is directly related to the induced stress through a local change in the difference of the refractive index. Finally, the difference between the principal stresses is calculated using the following equation:

$$\sigma_1 - \sigma_2 = \frac{R_m}{T(C_1 - C_2)} \quad (2.5)$$

where $C_1 - C_2 = C = 3.55 \times 10^{-12} Pa^{-1}$ for fused silica at the microscope's operated wavelength of 546 nm and is related to the piezo-optical coefficients by [97]:

$$C = \left(\frac{n^3}{2} \right) (\pi_{11} - \pi_{12}) \quad (2.6)$$

where π_{11} and π_{12} are the piezo-optic constants for fused silica and n is the refractive index of the material at 546 nm (the wavelength used by the instrument). T is the thickness of the sample and R_m is the measured retardance.

Considering the operating wavelength of the instrument, the retardance measurement spans between 0 and 273 nm. At higher retardance levels higher orders of fringes are observed. The final retardance is calculated taking into account the higher orders and according to the equation:

$$R_f = R_m + k \frac{\lambda}{2} \quad (2.7)$$

where R_f is the final retardance, R_m is the retardance measured in the test beam, k is the number of orders, and λ is the wavelength at which the instrument operates. By substituting Eq. (2.5) into Eq. (2.7) the final stress state is obtained.

v) Stress measurement on silica micro-beam

The retardance map is used to extrapolate the stress seen through a small surface of $4 \mu m^2$ in the center of the test beam (Fig. 34). The test was performed in room environment (temperature $T = 23 \text{ }^\circ\text{C} \pm 1 \text{ }^\circ\text{C}$, relative humidity $RH = 53\% \pm 2\%$).

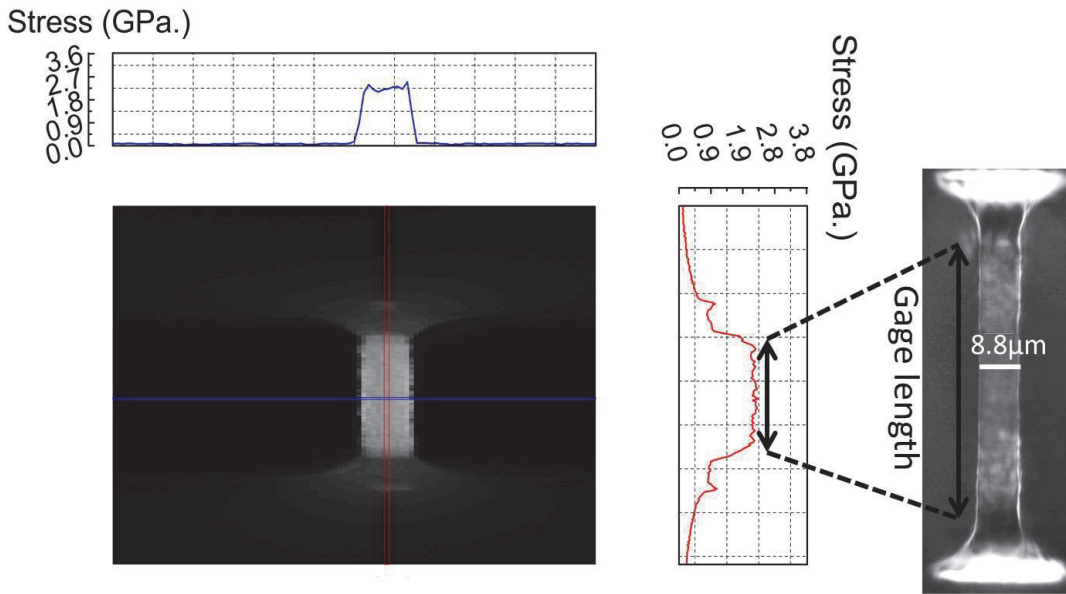


Fig. 34. Stress map of the test beam just before its failure. The stress is uniformly distributed along the length and the thickness of the test beam.

The stress level was calculated using Eq. (2.7) and taking into account the Poisson ratio of the material ($\nu = 0.165$). Indeed, if a material is stretched, it shrinks in the directions transverse to the direction of stretching. This has an impact on the measured stress, R_m , when using birefringence measurements to evaluate the stress as the stress is a function of the thickness of the material at the point of measurement. Note that due to the small strain values obtained in fused silica the Poisson effect may be neglected.

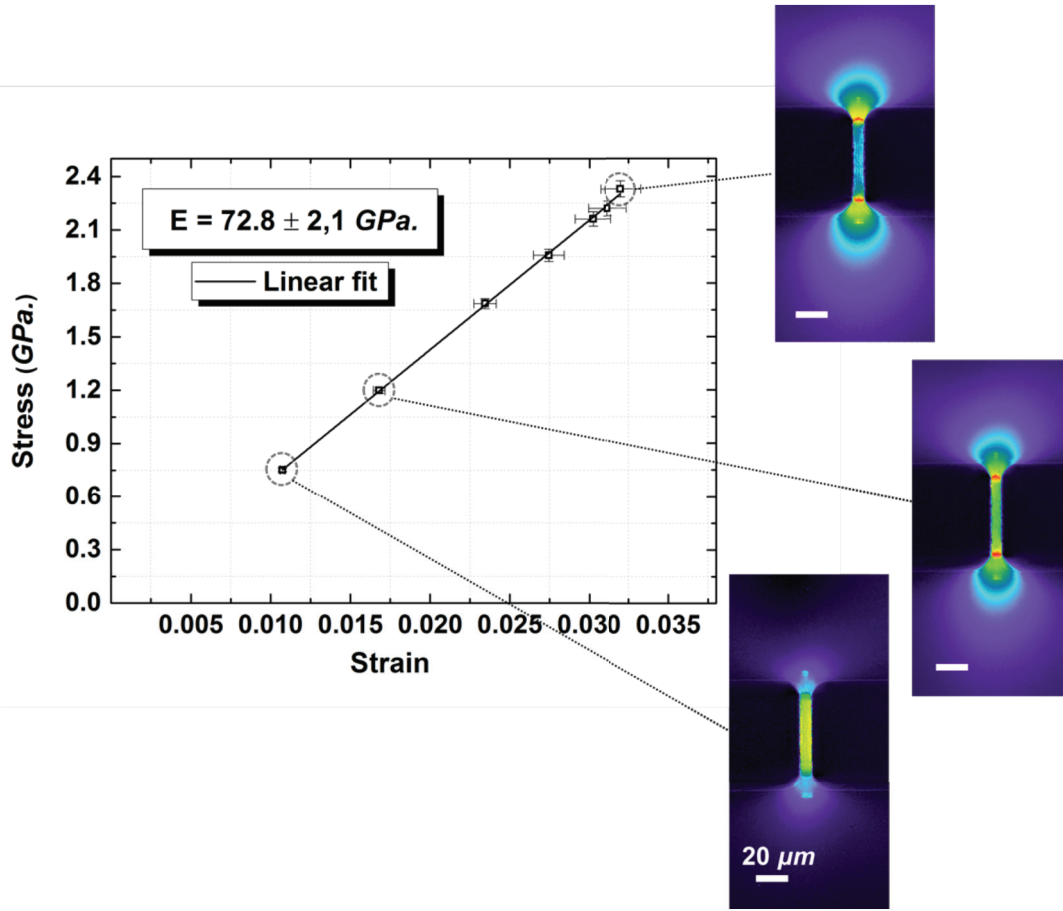


Fig. 35. A typical stress–strain curve is illustrated. The elastic modulus is estimated at 72.8 GPa with a relative error of 2.1 GPa. The scale bar is 20 μm in all the three photoelasticity images shown.

The bone-shaped specimen was designed with the dimensions of ($L \times W \times D$) 90 $\mu\text{m} \times 8 \mu\text{m} \times 53 \mu\text{m}$. Its in-plane dimensions were measured using third harmonics generation metrology, while its thickness was estimated by scanning electron microscopy measurements.

The strain of the test beam was based on the measured displacement of the amplification sensor. The amplification factor of the sensor was adjusted using finite element method simulations (COMSOL Multiphysics Software) using the post-etching dimensions of the device. The gage length of the test beam is calculated using the profile of the retardance values along the test beam and was verified by the stress profile simulated on the test beam.

As a proof of concept, the elastic modulus of fused silica is estimated (Fig. 35) and is consistent with the values commonly found in the literature, ranging between 72 and 73 GPa [46]. For the extrapolation of the elastic modulus, the slope of the stress-strain curve was used. The error values of the stress measurements in the first data points was low, therefore the error bars are not visible.

The fracture was brittle, and occurred at the end of the gage section [47] as indicated in Fig. 36, where stress-concentration is found at the location predicted by finite element method simulation (COMSOL). The stresses highest value is at the circled points being larger there by 15% than that in the central section. Although the fracture pattern morphology does not give a clear indication where the crack was first initiated, it seems likely and highly probable that the crack was initiated from this point. Nevertheless, this example suggests that we have not yet reached the point where the fracture is only governed by the inner strength of the material and not by material surface quality. Improving the surface quality further [48] could lead us closer to the actual fracture limit of the material.

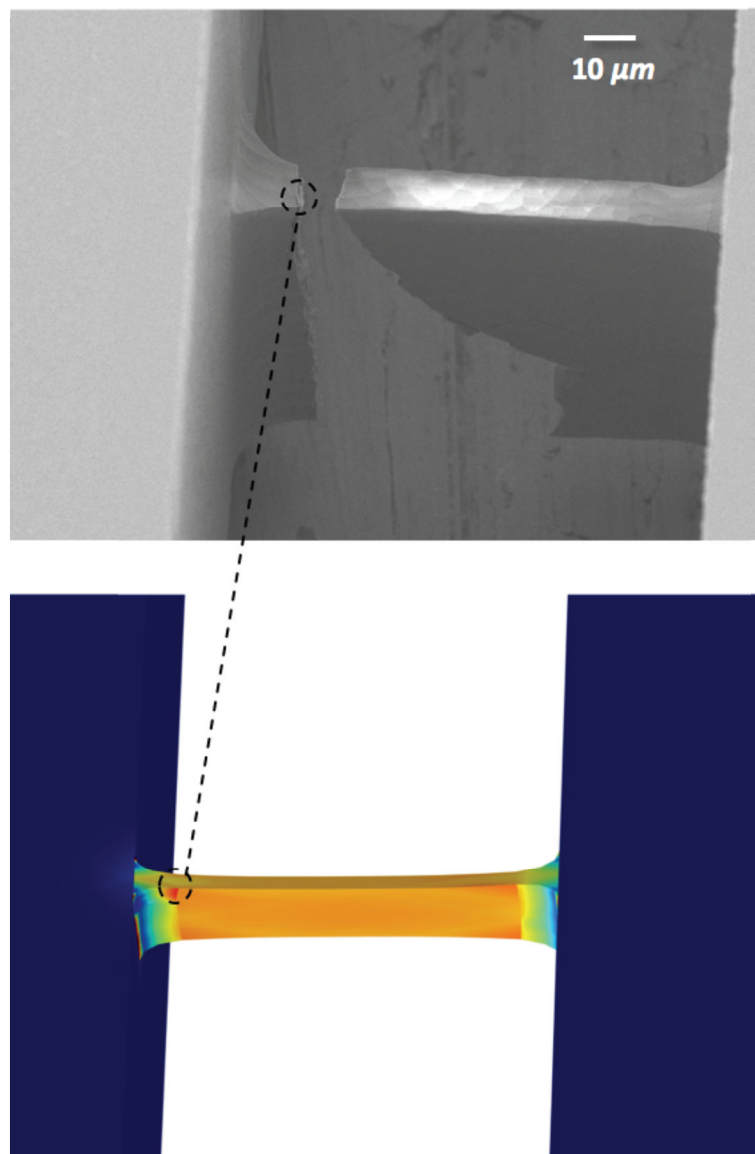


Fig. 36. Tested specimen under the scanning electron microscope (**Top**) and a virtual experiment using finite element analysis simulation software are illustrated (**Bottom**). The circled area has a stress concentration factor of 1.15.

vi) Weibull statistics of femtosecond laser processed fused silica loaded in uniaxial tension at the micro-scale

Using the tensile tester, uniaxial tests were performed on specimens of equal size in the same environment ($T = 23\text{ }^{\circ}\text{C} \pm 2\text{ }^{\circ}\text{C}$, $\text{RH} = 53\% \pm 5\%$). Nine devices were fabricated using the exact same laser parameters and etching time resulting to samples with similar surface quality.

As discussed in the previous section, in each test the load was increased up to the moment of failure. The strength values of each specimen are different, i.e., the strength is distributed. The fracture results are plotted according to the Weibull's two-parameter model [16, 101] following Eq. (1.1) (see Fig. 37).

The maximum measured stress was 2.7 GPa . The lowest stress value reported is 2.2 GPa which is at least 20 times above the recommended design value (typically 100 MPa [3]). At a stress level of 3.3 GPa the probability of failure is 99.9%. These values are consistent with the ones measured in [76].

Interestingly, the data are grouped around a straight line verifying that the Weibull theory is able to predict the failure of femtosecond laser processed fused silica. This provides an indication that the fundamental assumption of the Weibull theory [16, 102] the fact that the flaws are not linked with each other – is not violated for the processing method used here.

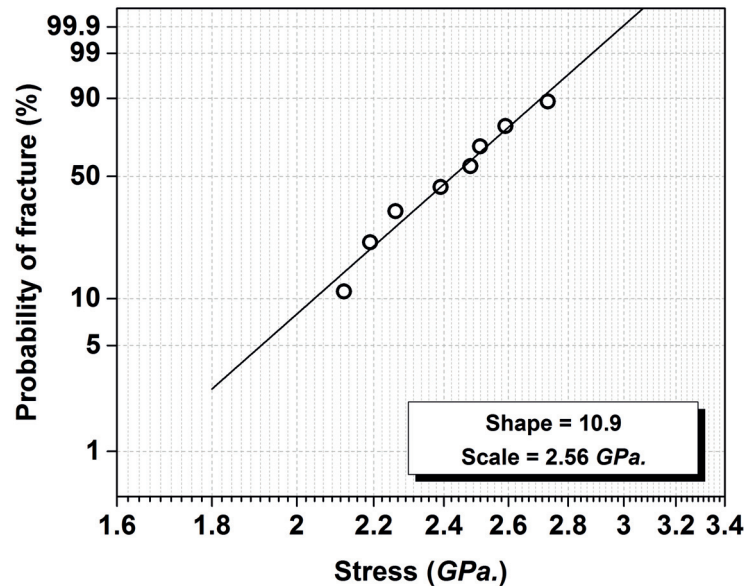


Fig. 37. Fused silica Weibull plot based on tensile test data. The circles represent the fracture data. The line is the Weibull fit to extract Weibull parameters shown in the inset.

The nominal stress, σ_N , and the shape parameter, m , are obtained ($m = 10.9 \pm 0.3$ and $\sigma_N = 2.56 \pm 0.1\text{ GPa}$). The shape parameter is relatively high indicating either a small flaw population or low flaw density (or a combination of both). For the sake of comparison,

ceramics and glasses with volumes less than $V = 10^{-4} \text{ mm}^3$ processed by advanced processing methods are reported to have an $m = [10-20]$ [51].

vii) Error analysis for the experimental technique

There are several contributing sources of error in the experimental procedure [104]. The first source originates in the stress measurements. The error in the thickness measurement introduced by the optical microscopy measurement of the test beam is significantly affecting the calculated stress of the test beam. The error of the retardance-measuring instrument (LC-Polscope) contributes, as well, in the stress calculation.

The stress uncertainty is calculated from the equation:

$$u_{\sigma} = \sqrt{\left(\frac{1}{Ct}\right)^2 u_R^2 + \left(\frac{R}{Ct^2}\right)^2 u_t^2} \quad (2.8)$$

where R is the measured retardance in the test beam, u_R is the uncertainty of the retardance measurement, t is the thickness of the test beam, u_t is the uncertainty of the thickness measurements, and is $C = 3.55 \times 10^{-12} \text{ Pa}^{-1}$.

The second source of error stems from the displacement amplification mechanism. Here, the main sources of uncertainty are the original measurement of the test beam's length and the output displacements of the displacement amplification sensor. Therefore, the error of the strain measurements is calculated as follows:

$$u_{\varepsilon} = \sqrt{\left(\frac{1}{L}\right)^2 u_{\varepsilon}^2 + \left(\frac{\Delta l}{L^2}\right)^2 u_L^2} \quad (2.9)$$

where L is the original length of the test beam, u_L is the uncertainty of the measured length, Δl is the output displacement of the displacement amplification sensor, and u_{ε} is the uncertainty of the measured displacement, normalized with the amplification factor of the sensor.

E. Discussion

The theoretical intrinsic strength of fused silica can be estimated from the relationship [105]:

$$\sigma_f = \frac{E\lambda}{\pi 2\alpha} \quad (2.10)$$

where E is the elastic modulus, α is the atomic separation, and λ is the period of the assumed interaction force. Assuming $\alpha = \lambda/2$, and $E = 72 \text{ GPa}$, the theoretical strength

limit of the material σ_f is evaluated to be as high as 24 *GPa*. Nevertheless, the maximum stress we achieved is 2.7 *GPa*. To further exploit the material's intrinsic mechanical strength, one needs to improve its surface quality. This can be achieved by post-processing methods, for instance, CO₂ laser processing which has been used to dramatically improve the surface quality of the produced structure as shown in Fig. 38. This would result to an increase of the shape parameter [100, 106].

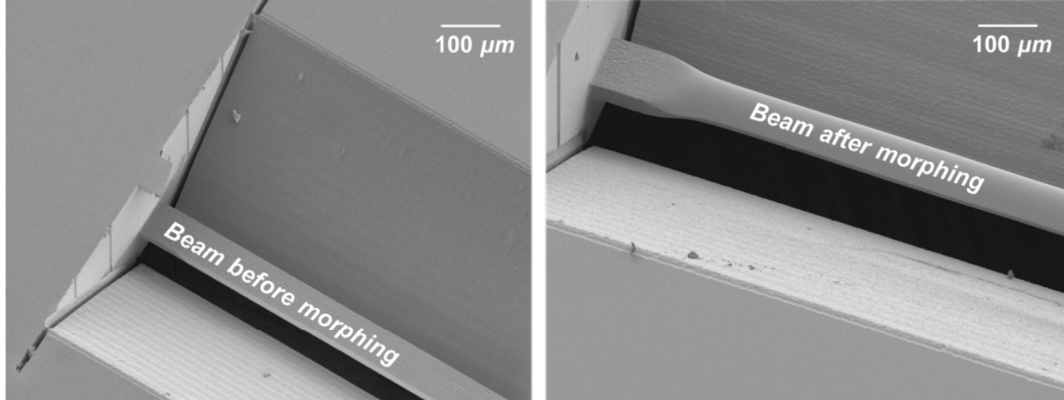


Fig. 38. Example of CO₂ laser post-processing of a suspended beam fabricated using femtosecond laser machining. The monolithic tensile tester provides the capability to investigate the mechanics of such high surface quality structures [107].

F. Conclusions and Outlook

In this chapter, a novel technique to perform micro-tensile testing was proposed in which the material under test is itself sculpted into a tensile tester. This configuration offers the capability to perform an experiment without mechanically interacting with the specimen and without the need of any assembly process. Along with the design of the instrument itself, the associated contactless measurement tools were proposed. High displacement resolution of 1 *nm* and minimizing of the bending stress level to less than 1% of the desired uniaxial stress were demonstrated.

As a proof of concept, we performed tensile testing of fused silica reaching stress levels up to 2.7 *GPa*. From the fracture mechanics point of view, in all of the nine specimens tested, fracture never appeared below 2.2 *GPa*. A shape parameter of $m = 10.9$ was extracted indicating that femtosecond laser machining combined with chemical etching can produce high performance mechanical parts with tensile strength at least 20 times above the recommended design value.

The instrument is not only applicable for uniaxial loading of fused silica; it can be adapted for testing other glasses, pending that an adequate specimen microstructuring process compatible with the instrument fabrication process itself is found.

The monolithic concept also offers a particularly suitable platform to explore the mechanical behavior of laser-induced composites in glass, which remain largely unexplored in the micro- and nano-scale. Indeed, it provides the opportunity to further

optically modify the test beam after fabrication, by using the same femtosecond laser that is used for the processing and operation of the device. By shaping the laser's pulses and/or parameters, different kinds of polymorphs can be embedded in the test beam, forming a laser-induced composite material that will ultimately be characterized.

A limitation of this instrument is that it can only be used for single cycle loading experiments due to the irreversibility of the loading process. Moreover, although the manufacturing process could be optimized to significantly reduce the manufacturing time, the loading process remains a time-consuming process not allowing the testing of a large number of specimens.

**Chapter III - RELAXATION PHENOMENA IN
FUSED SILICA SPECIMENS UNDER
CONSTANT TENSILE STRESS**

A. Introduction

In Chapter II we developed a micro-tensile tester to investigate fused silica's mechanics. By using this instrument, we presented results on the statistical fracture of the material.

In this chapter, we will make use of the micro-tensile tester- a simplified version of it- to investigate time dependent strength phenomena of fused silica. The results are of particular importance from a fundamental standpoint, as relaxation effects are inherently connected to the formation dynamics of glass. Moreover, our results provide a guideline to designers and engineers of fused silica-based devices to avoid unexpected mechanical performance or failure.

Fused silica's mechanical behavior and failure is known to be prone to environmental factors such as humidity and temperature [7-10, 108]. Here, we investigate the long-term mechanical behavior and delayed failure of fused silica under various stress levels and controlled environmental conditions. At high stress and humidity levels, the experimental data reveal a relaxation behavior of the material before its failure. Similar measurements at the same stress levels but significantly lower humidity levels show neither indication of relaxation behavior nor failure of the material.

In the first part of the chapter, we demonstrate the experimental setup used to perform tensile tests in controlled environments. In the second part, we present our results and review the existing fused silica failure models that could be used to interpret the results. Finally, we propose a plausible explanation for the origin of the relaxation.

B. Experimental procedure

i) Micro-tensile tester design and working principle

The principle of monolithic tensile testing is extensively discussed in Chapter II. Following the same approach, we design a simplified tensile testing device consisting of solely a loading cell and the sculpted test beam. This way, we can fit three testing devices in a single rectangular fused silica substrate ($25\text{ mm} \times 25\text{ mm}$) as shown in the Fig. 39.

For the three tensile testers in each substrate, the width of the loading bars is varying while the dimensions of the test specimens are of equal size. In this tensile testing design, the loading bars are working against the stiffness of the test beam. Therefore, as the test beam is being loaded, stress also develops in the loading bars. This stress might induce permanent relaxation effects in the loading bars themselves. To investigate the occurrence of any possible coupling phenomena originating from the loading bars that may affect the stress state in the test beam, we design the loading bars in each of the tensile testers with variable stiffness.

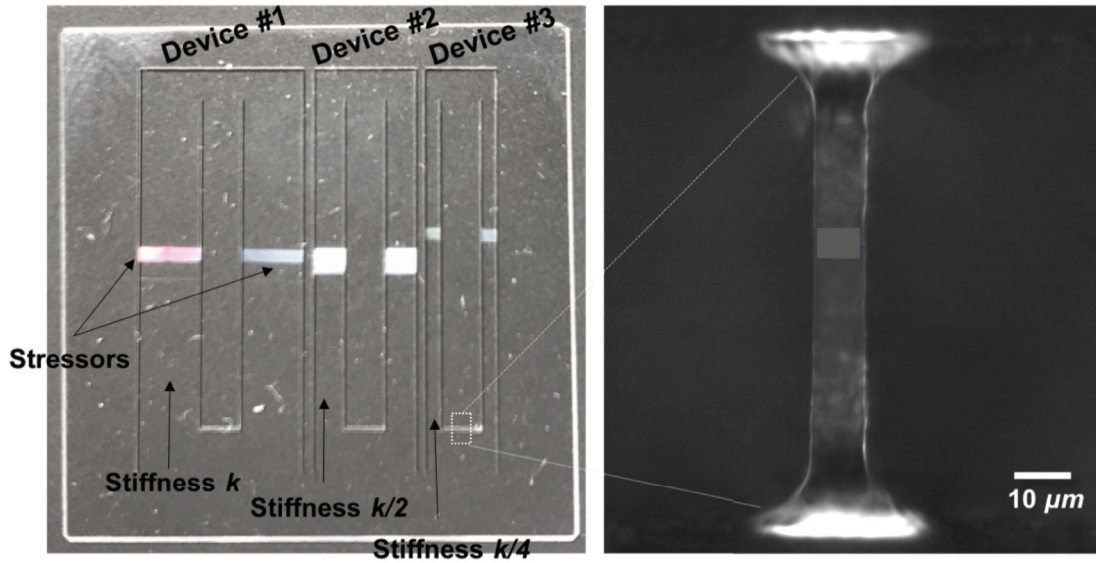


Fig. 39. (Left) Image of the silica specimen which consists of three tensile testers. The monolithic testing principle used in Chapter II is adopted for the design of the devices. (Right) Close-up view of a fused silica test beam.

ii) Manufacturing

We fabricate the devices using the femtosecond laser manufacturing process presented in the introductory chapter [71].

For the fabrication of this device, we use a scanning speed of 15 mm/s with a pulse energy of 250 nJ. The complete exposure step takes approximately one hour. After laser exposure, we etch the device for thirty hours in HF (2.5%). Twelve hours are essentially needed for the laser affected zones to be totally etched out; we let the device in the bath for another twelve hours to achieve better surface quality and therefore, enhanced mechanical strength [60] as discussed in Appendix C.

The re-exposure of the specimen to induce the desired volume variation is implemented by scanning adjacent lines at a writing speed of 12 mm/s and with an energy per pulse of 220 nJ. The re-exposure step requires four to eight hours depending on the stress levels to be achieved.

iii) Measurement setup

As part of another project in our lab a gas-shield chamber was designed. To control the environmental conditions during the loading of the specimen (the re-exposure step), we use the chamber (shown in Fig. 40b). A constant flow of nitrogen from the inlet to the outlet of the chamber ensures that the amount of water (H₂O) molecules within the chamber is limited. The chamber is designed with a transparent window which will allow a laser beam to pass through the test sample for the *in situ* non-contact stress monitoring.

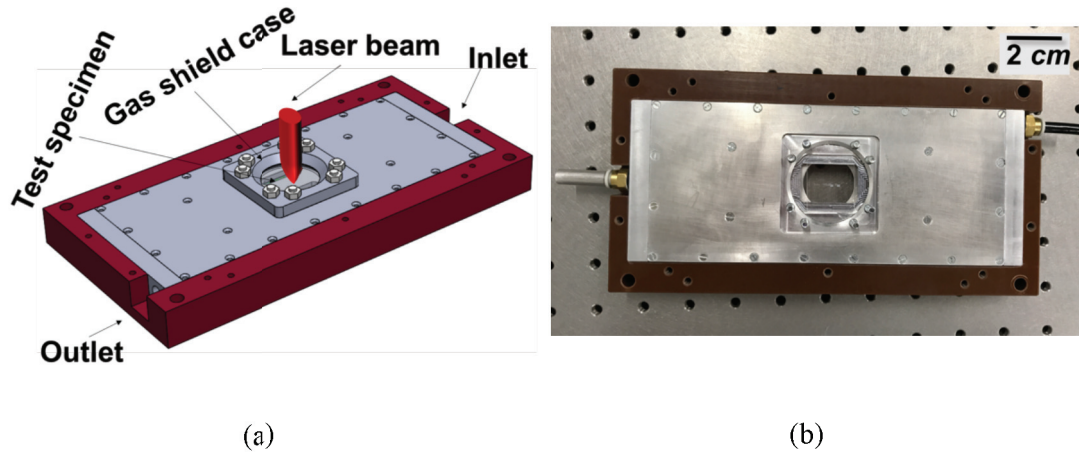


Fig. 40. (a) Computer-aided design (CAD) drawing of the gas shield chamber used to perform the experiments in a controlled environment. Nitrogen flows from the inlet to the outlet of the chamber drastically limiting the amount of water content within the chamber. (b) The manufactured chamber; the test specimen is placed in the middle of window so that the laser beam can pass through it and measure its stress state. The outlet is partly blocked with a metallic valve to eliminate the excessive flow of nitrogen.

Stress estimation is facilitated through photoelasticity, which gives a direct measurement of the induced stress in the test beam [27, 97]. In Chapter II, we used a commercial device (Polscope) to perform photoelastic measurements. For the purpose of this study, *in situ* long-term stress monitoring is needed. Thus, we have developed the specialized photoelasticity setup shown in Fig. 41 which is able to perform automated measurements on a specific point of the multiple test beams.

Let us briefly summarize its main features relevant for our practical case. We use a collimated laser beam emitted from a He-Ne laser source ($\lambda = 633 \text{ nm}$). The laser beam first passes through a polarizing beam splitter cube whose aim is to split the beam. One part of the beam is directed to a detector (Thorlabs PDA10A), which measures the fluctuation of the laser source. The second part of the beam passes through a half-waveplate that sets polarization at an angle β of 45° with respect to the flexure orientation.

After, the laser beam is expanded with a telescope, a lens ($f = 40.0 \text{ mm}$) is used to focus the beam tightly into the mechanical beam under stress (see Fig. 42). The width of the focal spot is calculated to be $8 \mu\text{m}$ while the depth of focus of the laser beam is $400 \mu\text{m}$.

A motorized linear actuator with an integrated controller (Newport – CONEX-TRA25CC) is used to control motion along one axis and thus to measure more than one device. The communication of the actuator is achieved via USB interface (Newport DC Servo Controller/Driver Model CONEX CC). The backlash of the actuator is less than 500 nm according to the manufacturer's datasheet.

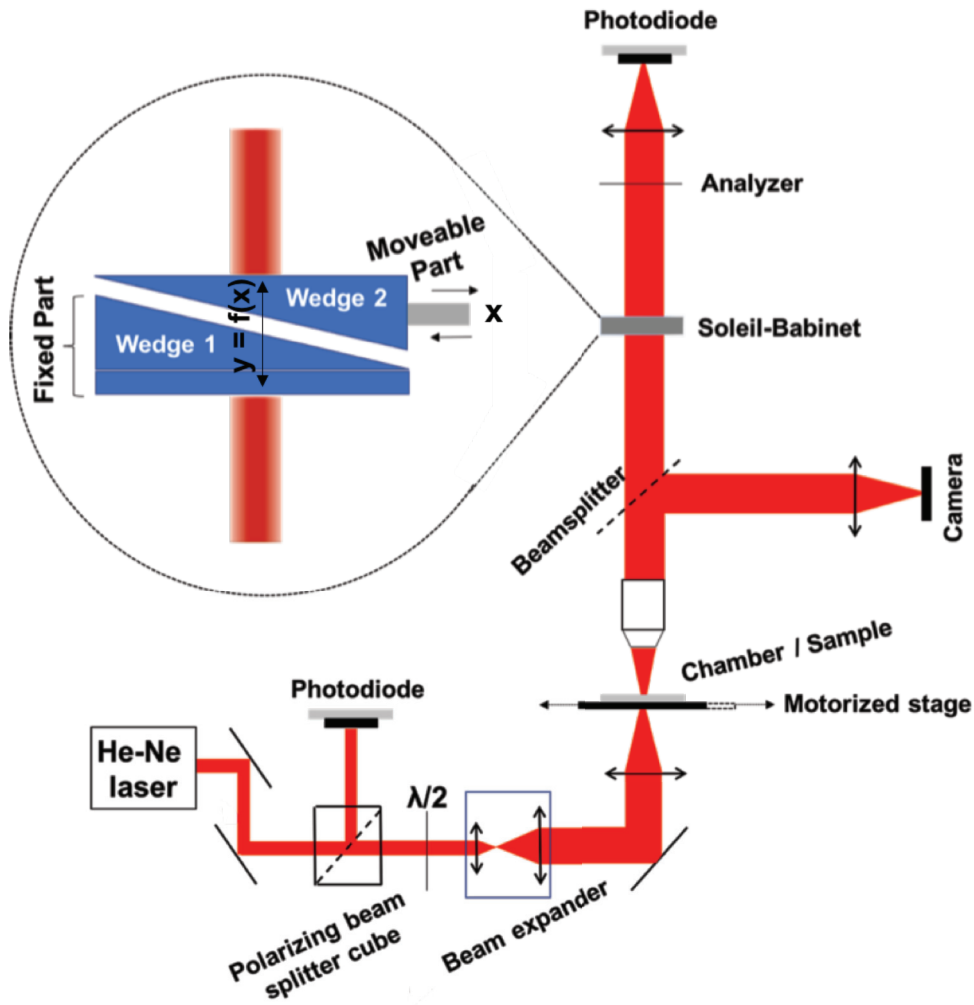


Fig. 41. Schematic of the optical setup used for monitoring stress in the fused silica test beams. A laser beam emitted from a He-Ne laser source passes through a half-waveplate to obtain the proper polarization state, and is focused in the test specimen. The beam is collimated again with an objective, passes through an analyser and is eventually driven into the imaging camera and measurement system. The inset illustrates the working principle of a Soleil-Babinet. The retardance is adjusted by moving the position of the long wedge relative to the short wedge using a precision digital micrometer. This allows the retardance to vary continuously as a function of the input displacement x .

After passing through the silica specimen, the beam goes through an objective (RMS20X) before splitting the beam into two paths. One path focuses the beam through a lens on a CCD camera (Thorlabs DCC1545M). The camera is needed to image the flexure for proper focusing of laser beam at the point of our interest. The second part of the beam passes through a variable retarder (Thorlabs SBC-VIS-Soleil-Babinet Compensator) and an analyzer (positioned at 90° with respect to the polarization state formed after the half-waveplate) and ends in an amplified photodetector (Thorlabs PDA100A-EC). The variable retarder shown in the inset of Fig. 41 consists of two wedges of the same wedge angle and a parallel plate. The optic axis of the two wedges have the same orientation and form a

variable thickness plate. In our case, we use it to offset the retardance level to zero so that only a difference of the intensity measurement is amplified. Finally, a detector is used to monitor the intensity of the laser beam.

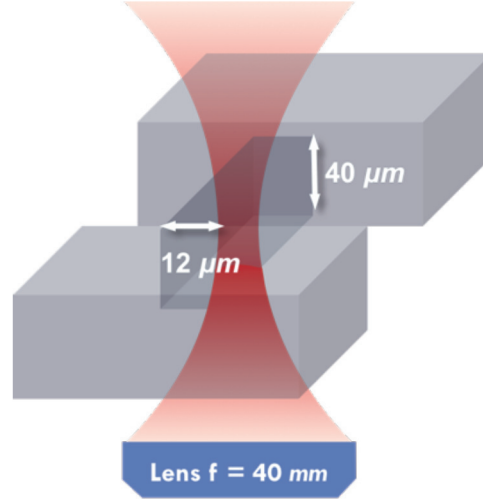


Fig. 42. Illustrative schematic of the tightly focused beam passing through the beam under stress. The dimensions of the test beam are $(L \times W \times D)$ $80 \mu m \times 12 \mu m \times 48 \mu m$.

The final retardance of the specimen, therefore, is given by the retardance offset as well as with the contribution of any difference in the amplified intensity:

$$R_{TOT} = R_{SB} + R_{DIF} \quad (3.1)$$

where R_{TOT} is the total retardance in the test specimen, R_{SB} is the retardance offset of the variable retarder, and R_{DIF} is the retardance difference. The intensity of light in the imaging plane is:

$$I(x, y) = I_0 \sin^2[2\beta(x, y)] \sin^2 \left[\frac{\varphi(x, y)}{2} \right] \quad (3.2)$$

in which β is the angle made between the birefringence axis and the analyzer. The intensity can be zero if this angle is 0 or $\pi/2$. The second sinus term describes the phase difference resulting from the stress-induced birefringence and can be expressed as:

$$\varphi = 2\pi C(\sigma_x - \sigma_y) \left(\frac{t}{\lambda_0} \right) = 2\pi \frac{R_{DIF}}{\lambda_0} \quad (3.3)$$

in which t is the thickness of the specimen, λ_0 is the wavelength of the light source, C is the Brewster constant, σ_x is the stress along the loading axis, σ_y is the stress perpendicular to the loading axis (negligible for the uniaxial loading conditions in our case), R_{DIF} is the retardance of the specimen [60].

C. Experimental results

The tensile testing devices are loaded to different stress levels. In Fig. 43 the stress over a time scale of approximately eighty days is shown. The loading of the device as well as the measurements are performed at room temperature and humidity levels ($T = 23\text{ }^{\circ}\text{C} \pm 2\text{ }^{\circ}\text{C}$, $\text{RH} = 53\% \pm 3\%$ for the red data points and $T = 21\text{ }^{\circ}\text{C} \pm 2\text{ }^{\circ}\text{C}$, $\text{RH} = 45\% \pm 3\%$ for the black data points in Fig. 43). Surprisingly, at higher stress levels ($>1.6\text{ GPa}$) we observe an evolution of the stress. At lower stress levels (1.1 GPa and less) the stress state remains the same. In all the cases marked with a cross, failure of the test specimens was observed. Based on the observations, the time dependent properties are described by an exponential function as follows:

$$y(t) = \exp\left[-\left(\frac{t}{\tau}\right)\right] \quad (3.4)$$

where t is the time (in seconds), and τ is a parameter associated with the rate of relaxation.

The overall time-dependent stress relaxation is therefore described by:

$$\sigma(t) = (\sigma_0 - \sigma_{\infty})y(t) + \sigma_{\infty} \quad (3.5)$$

where σ_{∞} is the stress level at the plateau before failure while σ_0 is the initial stress state.

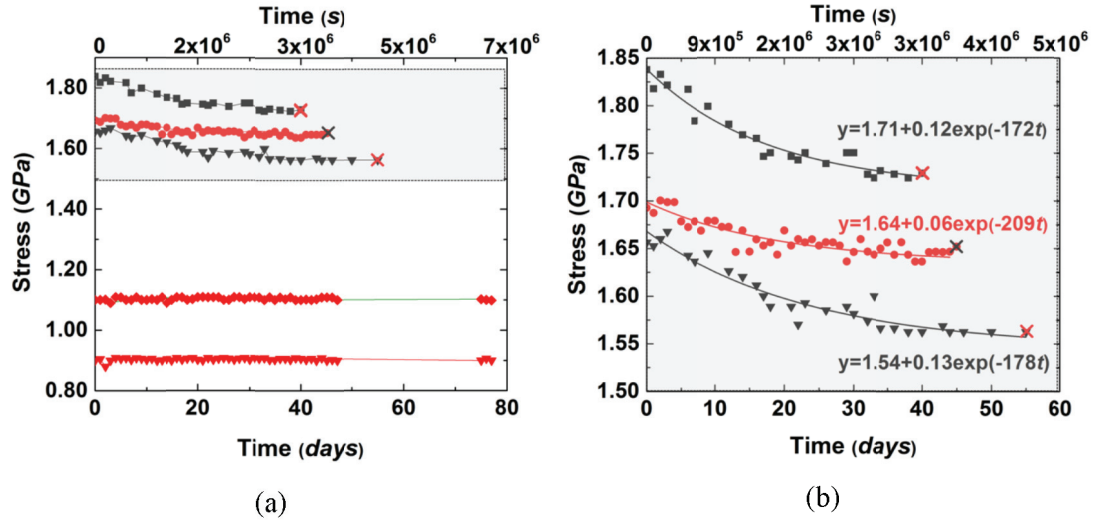


Fig. 43. (a) Stress vs. time measurements in fused silica at room temperature and humidity levels. The red data points are acquired by a commercial instrument (Polscope) at $T = 23\text{ }^{\circ}\text{C} \pm 2\text{ }^{\circ}\text{C}$, $\text{RH} = 53\% \pm 3\%$, while the black datapoints as obtained by the setup described in this chapter at $T = 21\text{ }^{\circ}\text{C} \pm 2\text{ }^{\circ}\text{C}$, $\text{RH} = 45\% \pm 3\%$. (b) Magnified view at higher stresses where the relaxation is observed. The fit is implemented using Eq. (3.5). The cross x represents the failure of the specimen.

Intrigued by these observations, we perform the same experiments at similar stress levels but at radically lower humidity levels ($T = 23\text{ }^{\circ}\text{C} \pm 2\text{ }^{\circ}\text{C}$, $\text{RH} < 1\%$) using the gas chamber illustrated in Fig. 44. Even at high stress states (1.6 GPa), there isn't any stress relaxation behavior observed. Furthermore, within this timescale, fracture of the test specimens did not occur. Note that in these measurements, both the measurement and the loading (exposure) steps are performed in low humidity levels.

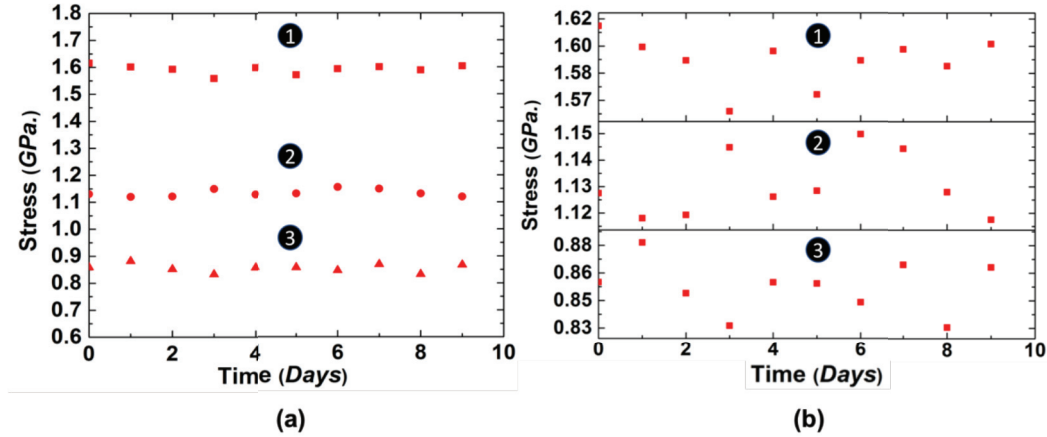


Fig. 44. (a) Stress vs. time measurements in fused silica at room temperature and low humidity levels ($T = 23\text{ }^{\circ}\text{C} \pm 2\text{ }^{\circ}\text{C}$, $\text{RH} < 1\%$). No relaxation behavior is observed. (b) High magnification of each of the three stress measurements revealing the experimental noise of the measuring process.

i) Stress evolution of fused silica, or the laser affected zones?

One may naturally raise this question since the observed change of stress state can arise either from the stressors (laser affected zones) or the test beam *per se*.

To clarify this issue, we varied the stiffness of the loading bars (Fig. 39). The two cases with the black data points in Fig. 43b correspond to different loading bar stiffness. The higher stress (1.85 GPa) is achieved with loading bars of stiffness k , while the lower one (1.65 GPa) to loading bars with stiffness $k/4$. If there were any influence from the loading bars, it would result in relaxation measurements of different rate. However, the rate of relaxation for the two cases does not vary significantly.

To further investigate this issue, we performed cantilevers experiments (the methodology is described in the previous chapter [61]). The loading of the cantilevers takes place with exposure parameters similar to the ones used to load the devices ($T = 23\text{ }^{\circ}\text{C} \pm 2\text{ }^{\circ}\text{C}$, $\text{RH} = 53\% \pm 3\%$). Although, the loading cases are not the same (the bending stiffness of the cantilevers is not identical to the stiffness that is seen by the laser affected zones when loading the tensile tester), these experiments provide a first insight towards the answer of this dilemma. As shown in Fig. 45, there is no change in the average stress of the cantilevers. Thus, we can assume that the stress in the laser affected zones remains the same.

Overall, based on both results we can safely assume that there is no major influence of the actuation (laser affected zones) in the evolution of the stress behavior in our measurements.

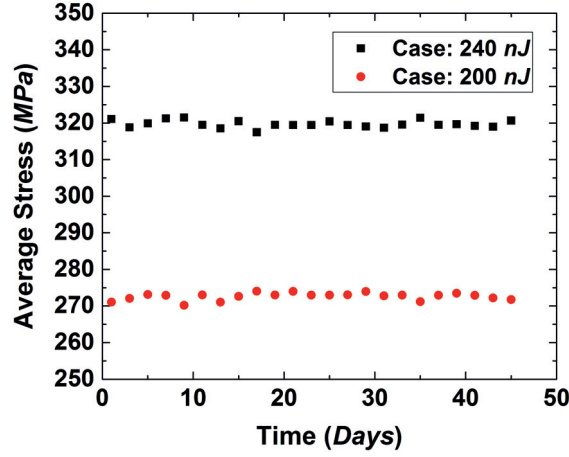


Fig. 45. Using cantilevers experiments (the method is described in the previous chapter), we are able to quantify whether the stress in the laser affected zones is evolving at room temperature and humidity ($T = 23\text{ }^{\circ}\text{C} \pm 2\text{ }^{\circ}\text{C}$, $\text{RH} = 53\% \pm 3\%$). There is no obvious change in the average stress of the cantilevers.

ii) Interpretation and discussion

Fracture of fused silica is often preceded by subcritical crack growth which results in delayed failure of the material. The exact mechanism by which water molecules break Si-O bonds has been largely investigated the last decades [7-10], yet a concrete model is still missing.

In our results, what triggers more our curiosity is not the delayed failure *per se*, but the mechanical relaxation behavior taking place before the failure. Based on the existing models of subcritical crack growth and glass fracture, we will propose a scenario to explain the relaxation behavior of the material.

The test beam shown in Fig. 39 is processed using the femtosecond laser micromanufacturing method described in Appendix B. Upon processing, surface flaws of different geometries are present which under high stress are stretched, and may be seen as cracks as illustrated in the schematic of Fig. 46 (further discussion on surface quality after processing can be found in Appendix C).

The stress intensity factor can be computed for a given crack size and geometry using Griffith's law expressed below:

$$K_I = Y\sigma\sqrt{a} \quad (3.6)$$

where Y is a crack geometry factor, σ is the nominal stress, and a is the flaw size. In our case, we can assume an elliptical “crack-like” defect of 100 nm under a stress of 1.8 GPa , taking $Y=1.1$. This results to stress intensity factor of $K_I = 0.7\text{ MPa m}^{1/2}$, which is close to the reported values [109] of K_{Ic} ranging between $K_I = 0.7 - 0.8\text{ MPa m}^{1/2}$.

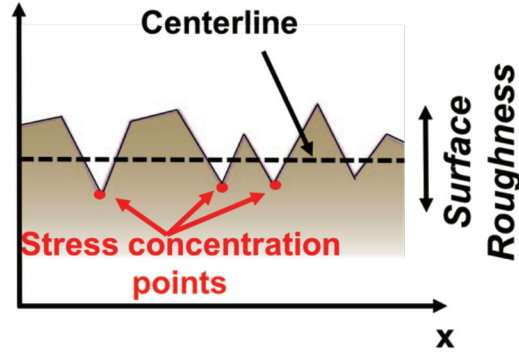


Fig. 46. Schematic illustrating the surface roughness of the material after femtosecond laser processing. The presence of stress-concentrating points in high water content environment can lead to subcritical crack growth.

In our experiment, we deal with two cases of environmental conditions: high and low water content. We will adopt a fracture mechanics point of view to describe the different behaviors observed.

In the case where very limited water content is present, cracks do not propagate [56] resulting in a stable stress vs. time behavior (Fig. 44).

In the case where high water content is present, the exact interaction of water molecules with Si-O bonds is unknown. In a classical picture proposed by Michalske and Bunker [111], water molecules break the Si-O bonds located exactly at the crack tip thanks to a hydrolysis reaction. However, more recent results from Bouchaud *et al.* [110] quantified an enhancement of the rate of diffusion of water into silica under high tensile stress. They suggest that water molecules diffuse within the material through the strained Si-O bonds. Due to heterogeneity of the glass, water starts breaking bonds and creates micro-cracks ahead of the crack tip. This in turn increases further the diffusion of water by leading to a substantial damaged zone and more favorable conditions for cracks to propagate (even below the K_{Ic} threshold). This model can explain the stress relief behavior that we observe as well the final failure of the specimen.

In this interpretation, the relaxation behavior and the fracture of the material are attributed to subcritical crack growth. Nevertheless, there are other existing models in the literature that may explain the relaxation behavior. Wiederhorn *et al.* [9] suggest water to be causing minor swelling of the material which in turn opposes the main driving force for crack growth. On the other hand, Tomozawa *et al.* [112] attribute the effect of water diffusion to be inducing a “plastic” zone in the outer layers of the material. However, both models fail to explain the failure of the specimen which is demonstrated in our results.

D. Conclusion

In what precedes, we investigated the behavior of fused silica at high stress levels under different humidity conditions. Using the monolithic tensile testing platform developed in the previous chapter, we loaded devices at varying stress levels. We have designed a photoelasticity setup to automatically measure stress in multiple devices for long time periods, which we have used to monitor the stress behavior of micro-scale fused silica test specimens. At low humidity conditions neither stress relaxation effects nor failure of the material was observed. At high humidity levels, we have observed a relaxation behavior and subsequent failure of the material.

The relaxation results are of great importance from the applications point of view since commercialization of mechanical devices made out of fused silica has recently started. From the fundamental point of view, further investigation of this puzzling phenomenon requires more experiments to get insight on the role of water molecules in crack initiation and propagation. A more systematic study at varying external loads and environmental conditions is needed to provide the basis for the development of a quantitative model.

Chapter IV - A FEMTOSECOND LASER TO INVESTIGATE FUSED SILICA FRACTURE MECHANICS

Based on the publication:

C.-E. Athanasiou, M.-O. Hongler and Y. Bellouard, "Unravelling Brittle-Fracture Statistics From Intermittent Patterns Formed During Femtosecond Laser Exposure" in *Physical Review Applied*, vol. 8, no. 5, p. 054013, 2017.

A. Introduction

In chapter II, we developed a micro-tensile tester, which we have used to investigate the fracture statistics of fused silica. This instrument offers significant improvements in testing the mechanics of glass in comparison to previously reported micro-tensile testers. Nevertheless, the operation of the instrument is time-consuming, limiting the number of specimens that can be tested.

In this chapter, we propose a femtosecond laser-based experimental method bypassing the need for many specimens to build-up statistically relevant ensembles of fracture tests in fused silica.

We investigate a peculiar phenomenon forming at the surface of fused silica when exposed to femtosecond laser irradiation. For the irradiation conditions for which nanogratings were expected to be found [83], two outcomes occur; periodic patterns with nanograting-like properties and chaotic patterns [113]. This shows a phenomenological analogy with idle and busy periods arising in queueing systems [114, 115]. Using queueing dynamics framework, we establish that these successive laser-generated cycles are statistically independent. Based on this analogy, and along with microscopic observations indicating that the transition carries fracture statistics information, we propose a novel fracture testing method for fused silica as well as other materials where this intermittent behavior can be found [58].

In the first part of this chapter, we report our results on the investigated pattern transitions and their link with mechanical stress. In the second part of this chapter, by applying queueing system theory in conjunction with a proposed mechanical model, we present a method to test the fracture mechanics of fused silica. Results showing the applicability of the method to other brittle materials are also presented.

B. Experimental observation of intermittent behavior

i) Experimental method

Using an Amplitude Systèmes' femtosecond laser with a pulse length of ~ 270 fs and a wavelength of 1030 nm, lines are written at the surface of fused silica glass as shown in Fig. 47. The repetition rate of the laser is 800 kHz. The velocity of writing is varied to achieve the desired energy deposition, or dosage, using high precision linear translation stages (PI Micos GmbH). The conditions of exposure are set by fixing the range of energy depositions (dosage) between 2 and 10 J/mm² for pulse energies of 184 , 188 , 191 , and 196 nJ that has previously been identified as likely to produce the most interesting results [113]. The laser is focused onto the specimen using a 40X objective lens (OFR/Thorlabs) that has an NA of 0.4 creating a maximum modification width of approximately 1.5 μ m as observed by the scanning electron microscopy (SEM) imaging. By varying the depth of laser tracks with respect to the surface of the specimen the modification is ensured to cross the surface plane. This method also allows the observation of the material modifications at different locations within the focal volume. For the analysis, the tracks, which are roughly 50% within the volume of the material, are used.

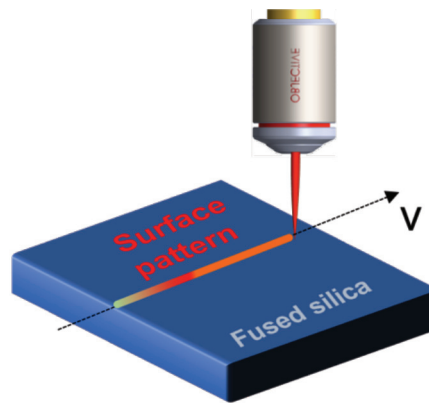


Fig. 47. Schematic of the laser processing the surface of fused silica glass. Vector (v) indicates the laser direction. The dashed line indicates the laser track and the red line the laser affected zone on the surface of fused silica.

Following the laser writing, the specimen is observed by a scanning electron microscope after a thin coating of gold ($\leq 30\text{ nm}$) was sputter-coated to create a conductive surface and avoid surface charging that can be induced by the electron microscope.

Note that for the statistical analysis of the laser tracks that follows, $500\text{ }\mu\text{m}$ are excluded from either ends to avoid possible changes due to the specimen's edge or stage acceleration/deceleration phases.

ii) Surface modification and observations

The surface of the laser modified lines are examined using the SEM to reveal the modification patterns.

Fig. 48 shows various SEM images of the different transitions. The transitions between organized parallel nanoplanes and erratic patterns ('chaotic like') occur abruptly and interestingly, alternate, displaying self-healing properties when apparent chaotic patterns reverse to highly organized ones (Fig. 48c). A single transition from self-organized to chaotic is displayed in Fig. 48b.

It is apparent that the chaotic structures contain cracks which is strong evidence that their formation is associated with mechanical stress. A higher magnification image at the location of the transition is shown in Fig. 49. Immediately after a crack is found, a chaotic sequence follows. Moreover, we observe that the formed cracks are oriented perpendicularly to the writing direction of the laser.

Note that in the first reported work studying the intermittent behavior [113], after the laser writing, the authors have used a chemical etching step dipping the specimen in aqueous hydrofluoric acid (with 2.5% concentration). The post-etched specimens reveal more clearly the details and orientation of the cracks (the modified track has much higher etching rate than the surrounding material as discussed in Appendix B). Images can be found in [113].

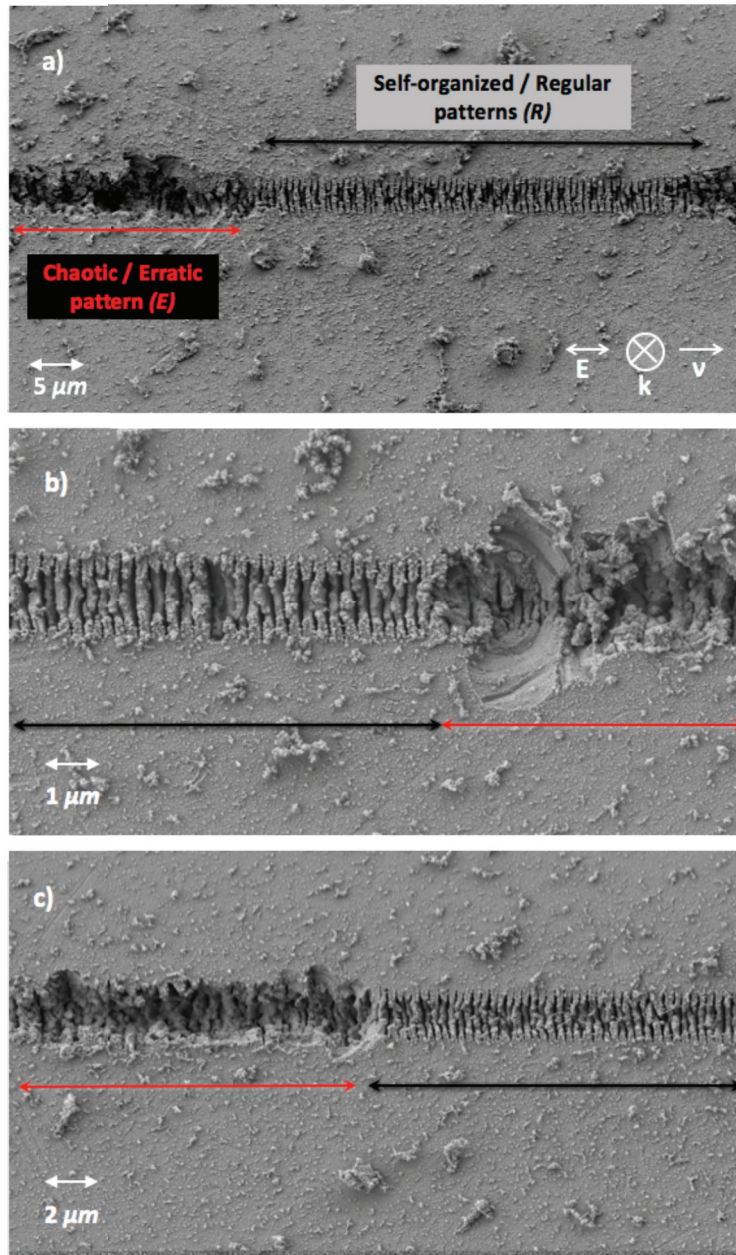


Fig. 48. (a) Scanning Electron Microscope image (SEM) of laser-processed lines indicating the scanning direction (v), the polarization (E) and the pattern that is written on the surface of a fused silica substrate. (b - c) shows magnified view of some line patterns transitions between regular structures and chaotic structures, and vice versa. The black double-arrows indicate regular patterns, while the red ones emphasize chaotic regimes. The pulse energy is 196 nJ. There are about 40 pulses overlapping each unit volume, producing a net fluence of 3 J/mm^2 . In all these experiments, the numerical aperture is 0.4.

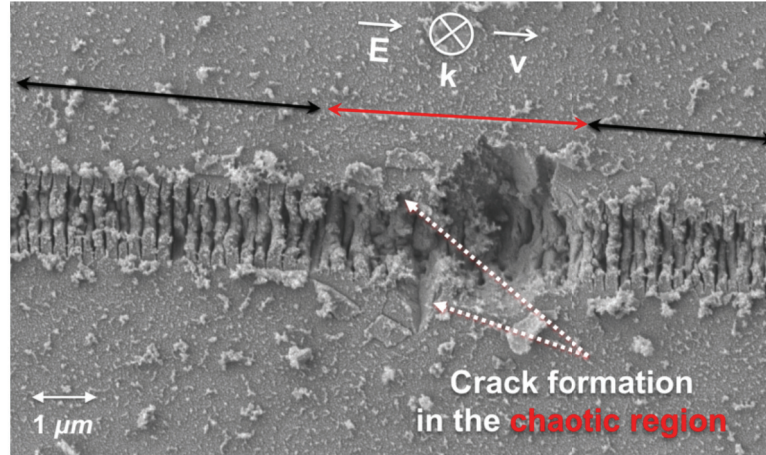


Fig. 49. High magnification SEM image of the transition from self-organized to chaotic, and vice versa. Of particular interest for this work is the presence of cracks in the chaotic region. Noteworthy, the cracks found are perpendicular to the laser's writing direction.

C. Modeling the intermittent behavior

In what follows, we explore how the intermittent phenomenon can be used to extract information about the fracture mechanics of fused silica.

i) Concept of nano-fracture experiments

As the transitions are linked to stress, we formulate the hypothesis that these events originate in the statistical nature of the fracture. Indeed, for brittle materials, one cannot define a precise elastic limit above which they rupture. Rather, their fracture behavior is usually described by a law that defines the probability of failure at a given stress level σ , well captured by a Weibull distribution [16] as follows:

$$P(m, \sigma_N; \sigma) = 1 - \exp \left[-\gamma \left(\frac{\sigma}{\sigma_N} \right)^m \right] \quad (4.1)$$

The above function is defined by three parameters: the nominal stress, σ_N , the exponential factor, m , and γ , a geometrical parameter fixed by the experimental conditions (in our case, the volume tested in comparison with a reference volume – as a reference volume we define the one obtained for the case of 184 nJ). The two main parameters, σ_N and m , are determined by fitting an experimental curve derived from the equation Eq. (4.1) [101].

In previous works [74, 75, 116], we have shown that self-organized patterns are associated with a significant amount of stress introduced in the material during laser exposure. Having in mind this observation, we formulate the general hypothesis that each single nanoplane is equivalent to loading the material to a certain stress level, and in other words, forms a single 'nano-fracture' test experiment.

The general hypothesis is based on two assumptions. First, each single ‘nano-fracture’ test is independent to the previous one; second, each nanoplane forming at a given and known deposited energy corresponds to a known stress loading level. The second point has been validated in reference [75]. Let us now establish the validity of the first one by examining the statistical nature of the intermittency.

To do so, a number of lines are written at the surface of three brittle materials using a femtosecond laser with varying deposited and pulse energies following a similar approach reported in [113].

As laser’s deposited energy we define the amount of energy passing through a given surface element equal to the spot area in the beam waist plane that can be estimated as follows:

$$\Phi_d = \left(\frac{4E_p}{\pi} \right) \left(\frac{1}{w_{LAZ}} \right) \left(\frac{f}{v} \right) \quad (4.2)$$

in which E_p is the energy deposited for a single pulse, w_{LAZ} is the non-linear absorption beam waist, f is the laser repetition rate, and v is the writing speed.

The deposited energy is governed by three parameters, namely the pulse energy, the writing speed (scanning), and the repetition rate of the laser (Fig. 50). Depending on the selection of parameters, both volume expansion and/or densification can be induced in fused silica.

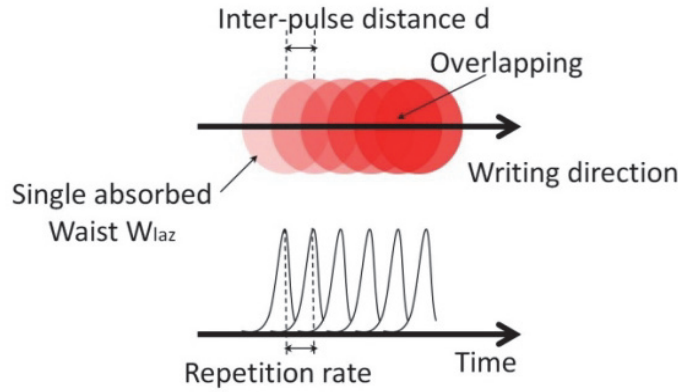


Fig. 50. Schematic illustrating the concept of energy deposition, as influenced by the laser process parameters. Repetition rate, f , is the rate at which pulses are emitted, writing speed and energy per pulse are the main parameters that can be tuned to control the energy deposition. Repetition rate and speed define the distance between pulses, d . The pulse energy defines the size of the laser affected zone [61].

Then, we measure the length of sections displaying chaotic and self-organized patterns. The results are shown in Fig. 51 where black and red domains represent self-organized

regimes (R) and chaotic regimes (E), respectively. We observe that as the deposited energy increases, both the length and frequency of erratic patterns increase. Likewise, the higher pulse energies also show the same trend, i.e., an increase in the length of the chaotic patterns. Eventually the laser tracks were dominated by chaotic structures for all the pulse energies.

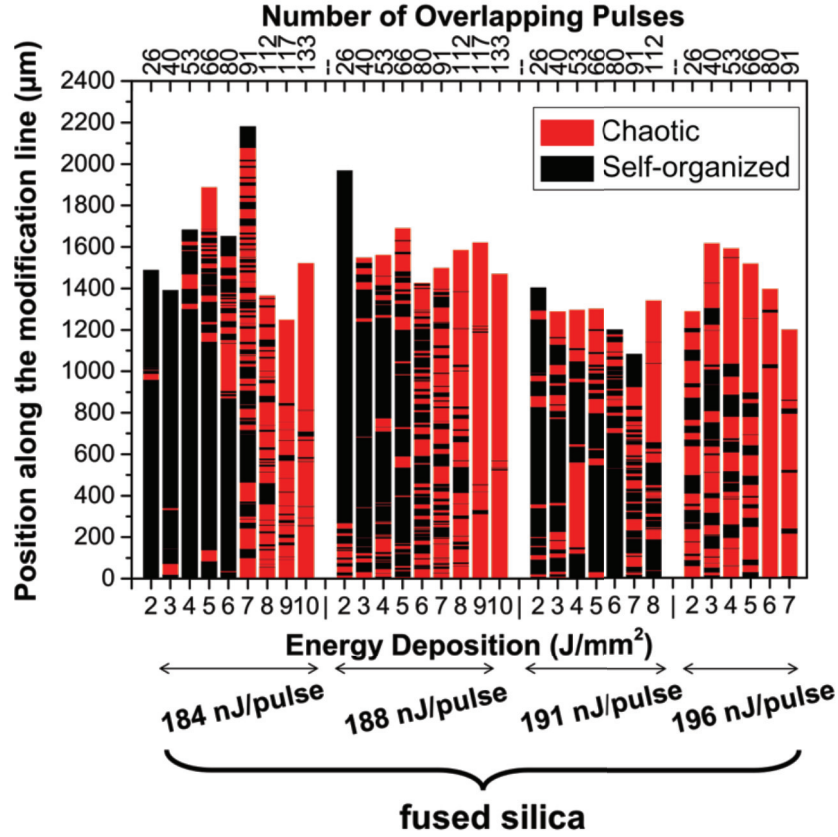


Fig. 51. Overview of the transitions for different energy depositions and pulse energies. Black regions represent the self-organized patterns and the red ones the chaotic patterns.

ii) Queuing system framework

In general, intermittency due to alternations between regular and erratic patterns may arise either in deterministic, nonlinear, dynamical systems (like Pomeau-Manneville [117]) performing transitions from periodic to chaotic evolutions or in stochastic storage systems, where an intrinsic randomness of the incoming and outgoing flows lead to an alternation between "busy" and "idle" periods in queuing theory [114].

Here, to phenomenologically model the regenerative alternation between self-organized patterns and chaotic ones, we adopt the point of view and analogy of a virtual queuing system (QS).

The laser/glass ensemble forms an open system in which the deposited energy is steadily dissipated via several distinct physical mechanisms, one of them being precisely the self-

generation of intermittent dissipative patterns. Let us now analyze this intermittency using queueing dynamics framework [118]. A single, cyclic alternation between the length E and R defines itself a cycle with random length $C = E + R$. Based on this observation, one may naturally raise the question: ‘are the successive cycles (C) statistically independent?’

Following this metaphor, laser pulses are steadily (separated in time by a fixed time interval) delivered in the system. A part of the energy is dissipated through different mechanisms in the material such as reflection, nanopores formation and other complex phenomena. However, part of the energy is stored into the glass and then released via the pattern generation mechanism. In this stylized view, ‘incoming customers’ are waiting to be served in a ‘storing’ room as shown in Fig. 52. From the general QS theory, we know that the queue content alternates between two states, the so-called idle periods (IP) and busy periods (BP). We shall call I , the time interval duration of an IP while θ of a BP. Both I and θ are random variables which, as we shall establish, are statistically independent, a fact that will actually be experimentally verified *a posteriori*.

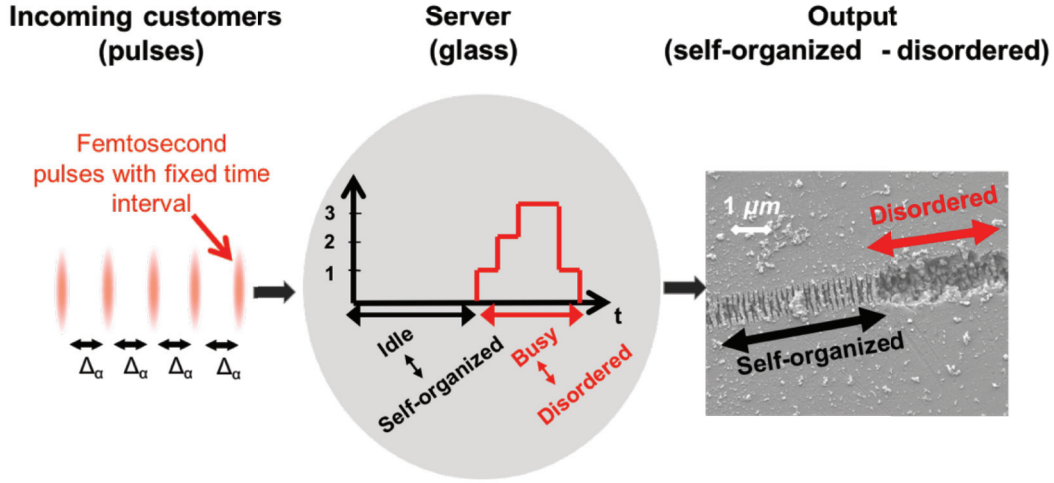


Fig. 52. Visualization of the queueing system analogy used to model the intermittent behavior. The steadily (separated in time by a fixed time interval Δ_α) derived femtosecond laser pulses into the glass may be seen in QS framework as ‘incoming customers’ waiting to be served by ‘a server’. The ‘server’ *per se* depending on the number of customers waiting (the queue content shown in the middle figure) can have two distinct states, the idle one corresponding to the production of self-organized patterns or the busy one corresponding to the production of chaotic patterns.

From microscopic observations, we note that the spacing between nanoplanes appearing in the regular portion of the patterns is independent to the energy delivered by the laser. Considering this spacing, we may now define a natural characteristic length scale and its related time scale $t_0 := w_L/v_0$, where v_0 is the translation velocity of the laser. Let us also introduce $\lambda \in [0, 1]$ to be the probability that a busy period starts (or equivalently, an idle period ends) in the next time slot t_0 . Accordingly, $Prob\{I = k\} = \lambda(1 - \lambda)^{k-1}$ stands for the geometric probability law to observe an idle period of duration k . For this

geometric probability law, the average idle period time is $E\{I\} = \lambda^{-1}$ and its variance reads $\sigma_a^2 = (1 - \lambda)/\lambda^2$.

Accordingly, we assimilate the beginning of the busy period start with the arrival of a virtual customer in an abstract discrete time queuing system belonging to the Geo/G/1 dynamics. The notation Geo stands for the geometric law governing the arrivals and G specifies the general service time distributions (let us write μ^{-1} and σ_s^2 , for the average and the variance, respectively). From [114], the first two moments of the busy period θ of the Geo/G/1 queue are explicitly known and read:

$$\begin{cases} E\{\theta\} = \frac{1}{\mu(1 - \rho)} \\ \sigma_\theta^2 = E\{\theta^2\} - [E\{\theta\}]^2 = \frac{\sigma_s^2}{(1 - \rho)^3} \end{cases} \quad (4.3)$$

where $\rho = \lambda/\mu \in [0, 1]$ is the QS offered traffic. Note that for the abstract QS, all times appearing in Eq. (4.3) are now expressed in the natural time units t_0 . As for an alternative stochastic process in general and hence for the Geo/G/1, the $E\{I\} = \lambda^{-1}$, we have [115]:

$$\rho = \frac{E\{\theta\}}{E\{I\} + E\{\theta\}} \quad (4.4)$$

Eq. (4.4) implies that ρ can be measured directly from the experimental patterns in Fig. 52. In addition, keeping μ fixed while varying the traffic r (i.e., the delivered deposited energy), the first line of Eq. (4.3) implies:

$$\frac{E\{\theta_1\}}{E\{\theta_2\}} = \frac{1 - \rho_2}{1 - \rho_1} \quad (4.5)$$

where θ_k and ρ_k for $k = 1, 2$ stand for two different BPs resulting from two different traffic loads.

Accordingly, whenever (up to experimental errors) the equality of Eq. (4.5) is satisfied for a set of experiments, one can conclude that the hypotheses underlying our abstract Geo/G/1 picture hold. If this is the case, the further conclusions can be drawn:

- a) a single μ exists and it characterizes the typical energy dissipation rate that can be associated to the R/E patterns generation.
- b) Most importantly, the basic hypothesis underlying the QS theory is realized. Since these conditions are fulfilled, the successive busy (BP) and idle periods (IP) as well as their alternation are statistically independent.

The experimental validity of Eq. (4.5) is summarized in Table 2. This validates our abstract QS metaphor explicitly and it is reasonable to assume that each nanoplane forms a statistically independent fracture experiment.

188 nJ			196 nJ		
0.34	0.48	0.14	0.59	0.65	0.06
0.81	0.76	0.05	0.77	0.69	0.08
0.58	0.55	0.03	0.24	0.25	0.01
0.73	0.37	0.36	0.50	0.60	0.10
0.62	0.74	0.12	$E\{\Theta_i\}/E\{\Theta_j\}$	$(1-\rho_i)/(1-\rho_j)$	Absolute difference
$E\{\Theta_i\}/E\{\Theta_j\}$	$(1-\rho_i)/(1-\rho_j)$	Absolute difference			

Table 2. Summary of the Geo/G/1 queuing theory results. For the calculations, measured values of $E\{\Theta_i\}$ and ρ_i are used to validate the left-hand and the right-hand side of Eq. (4.5). When these values coincide, the system follows the dynamics of the Geo/G/1 QS. Values within 0.15 range are represented in green colour while outliers are represented in red colour.

iii) Microscopic modelling

Let us now investigate the microscopic origin of the intermittency. More specifically, we examine the transition from the self-organized regime to the chaotic one and the underlying mechanism which triggers the transition to a chaotic regime.

In previous works, we have demonstrated that the formation of nanogratings is accompanied by net volume expansion. This volume expansion is attributed to the formation of a homogeneous, porous structure within the lamellae (shown in Fig. 53). Evidence of the porous structure can be found in these works [119, 120]. The result of this volume expansion is the generation of a significant amount of stress in the material and eventually the build-up of compressive stress around the laser affected zones.

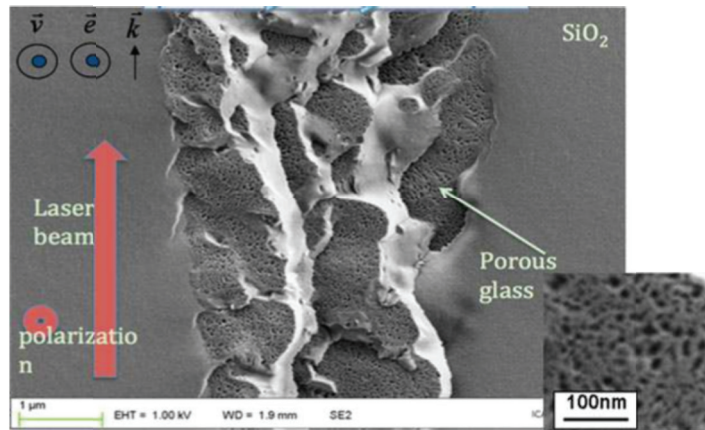


Fig. 53. Scanning electron microscope (SEM) image of the laser track cross section revealing the presence of porous material. The picture is adapted from [119].

Using the micro-cantilevers bending method (described in Section D of Chapter II, and in more details in these works [75, 76]) we investigate the link between the laser's deposited energy and the compressive stress in the laser affected zones for the specific exposure conditions we use. Indeed, as indicated by a previous work [75], there is a linear relationship between the deposited energy and the average compressive stress formed in-between the lamellae, as shown in Fig. 54. Note that experimentally the deposited energy is tuned by adjusting the writing velocity of the laser.

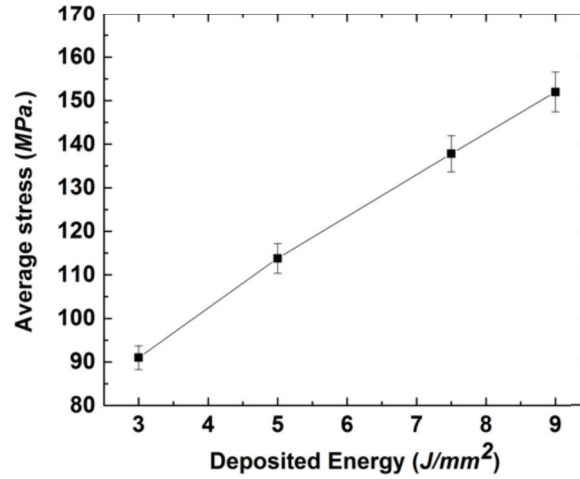


Fig. 54. The average stress between the nanoplanes in fused silica for the case of 196 nJ per pulse at 800 kHz . The deposited energy is tuned by changing the translation velocity of the laser.

The laser affected zone occupies an ellipsoidal volume stretched along the optical axis, as shown in Fig. 55.

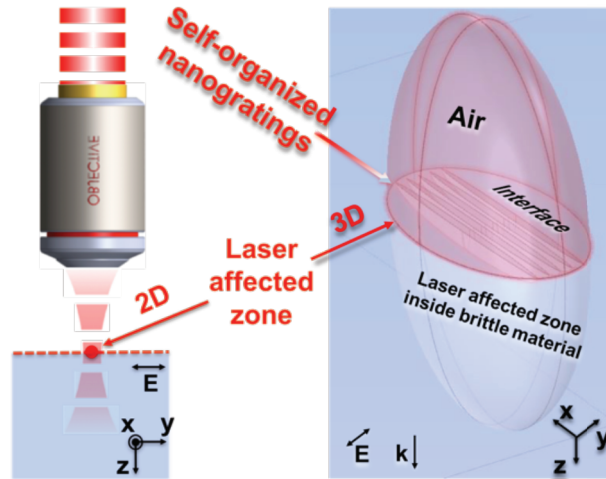


Fig. 55. Schematic illustration of the femtosecond laser ellipsoid which corresponds to the laser affected volume. The waist of the ellipsoidal is focused on the material-air interface, producing patterns on the surface of the material.

We can assume that the size of the nanogratings in the x and z dimensions follow the size of the ellipsoidal and can be approximated by the following equations [61, 76]:

$$z_0(I) = 2 \left(\frac{\pi \nu I^2}{\lambda} \right) \sqrt{\left(\frac{I_0}{I} - 1 \right)}, \quad x_0(I) = 2 \sqrt{\frac{I^2}{2} \log \left(\frac{I}{I_0} \right)}, \quad (4.6)$$

in which I is the focused laser peak intensity, I_0 is the threshold intensity for nonlinear absorption, ν is the refractive index of the media, λ is the wavelength of the laser, and l is the beam waist at the focus. The increase of the size of the lamellae as a function of the pulse energy can be seen in Fig. 56.

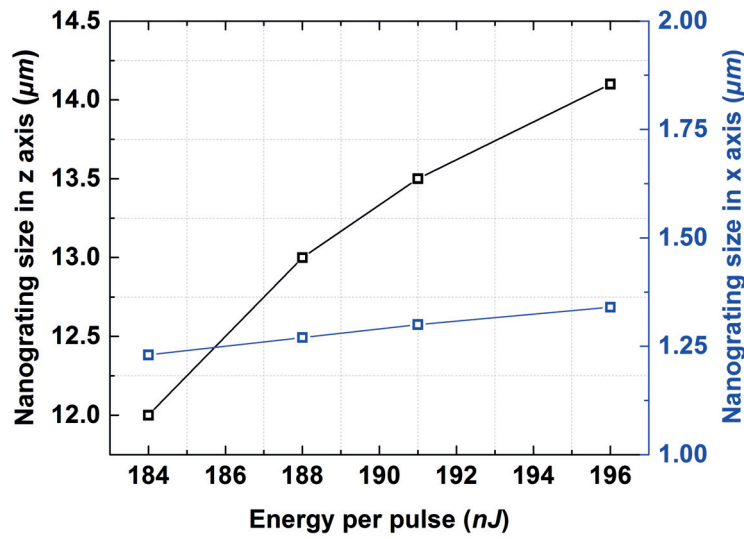


Fig. 56. Approximated dimensions of the lamellae for the pulse energies used in this work. The calculation is based on a simple beam propagation model using threshold intensity to capture the nonlinear absorption domain [61, 76].

Considering the shape of the nanogratings (Fig. 57 and Fig. 58), high stress concentration is found at the tip of these nanoplanes at the interface of the pristine glass with the laser affected material, where the stress gradient is the highest. This hypothesis is also supported by atomic force microscope measurements [116] indicating that the interface of the laser affected and unaffected zones as prone to crack nucleation and formation.

D. Experimental results

i) Nano-loading results on fused silica

The formation of individual elements of a pattern (nanoplane) is, essentially, a tensile test at the nano-scale. The maximum stress is found at the tip of the nanoplane, and in a first approximation, is given by Inglis formula [121]: $\sigma_{\max} = \sigma_{\text{AVG}} \left(1 + \frac{2a}{b} \right)$. The parameters

σ_{AVG} , a , b are the average stress between the lamellae, and geometrical factors, respectively (see Fig. 57).

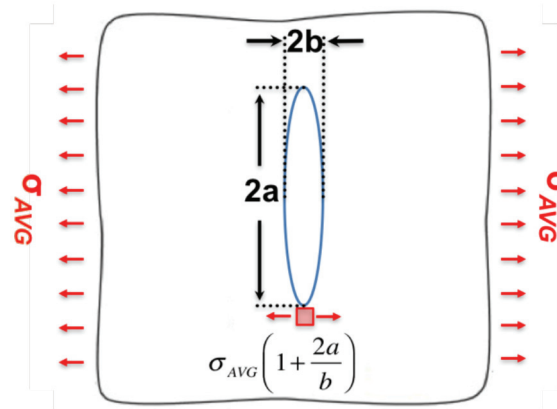


Fig. 57. Illustration of the loading conditions for a single nanoplane formalized as an Inglis fracture problem [121].

Note that the Inglis formula is a first order model to estimate the stress at the tip of the lamellae. The volume expansion along the modification line is also present and expected to build-up minor shear stress (mode II) near the interface of the laser affected zones with the pristine material due to sliding. To capture the effect of shear stress or even more complex stress states that may occur at the tip of the lamellae, more advanced models need to be employed. We refer the interested reader here [122].

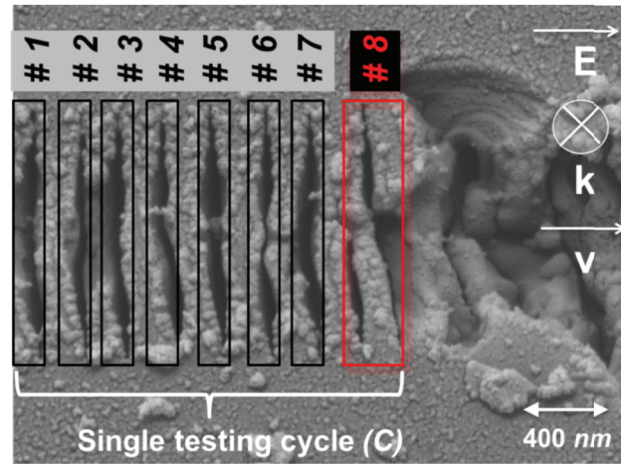


Fig. 58. Each element formation can be seen as an individual tensile-stress loading experiment. A testing cycle (C) is terminated when a fracture occurs.

Each single experiment *per se*, can have two outcomes: either one regular nanoplane formation or the nucleation of a crack.

The main outcome of the queuing model was that the lamellae as well as the cycles they are forming are statistically independent from each other. Thus, we safely assume a strict independence between loading events. The number of experiments taking place before

failure occurs can be formulated mathematically by the geometric distribution $Prob\{r = n\} = p(1 - p)^{n-1}$, where r is the number of experiments performed in one experimental cycle (defined as C in our QS model) and p is the probability of failure to happen.

In fused silica, one cannot precisely define the elastic limit above which the material ruptures. The probability of failure under a given stress is commonly described by the Weibull statistical law [16]. Combining Weibull law with the average of geometric distribution, we get the following equation:

$$\underbrace{\ln \left[-\ln \left(1 - \frac{1}{\bar{r}} \right) \right]}_{\gamma} = \underbrace{m \ln \sigma}_{mx} - \underbrace{\left[m \ln \sigma_N + \ln \left(\frac{V}{V_0} \right) \right]}_{\beta} \quad (4.7)$$

The equation is defined by two parameters: the scale parameter, σ_N , which has the same dimensions as a stress, and the dimensionless factor, m (also called Weibull modulus). The average number of nanoplanes, \bar{r} , is measured using the SEM images for the various deposited energies, like the ones shown in Fig. 48 and Fig. 49. The applied stress, σ , is extracted through cantilever experiments (methodology described in Chapter II). Parameters V , V_0 are used in order to take into account the different size of these stretched ellipsoidal nanoplanes as the energy per pulse increases and are obtained using the data of Fig. 56, though the contribution of this factor is minor.

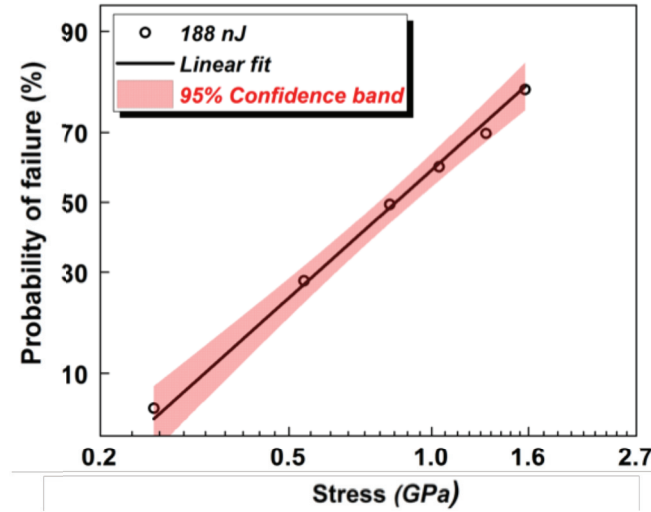


Fig. 59. The graph represents the probability of fused silica to fail under a certain stress level. The 95% confidence band is given by the equation $x \pm Z\sigma/\sqrt{n}$, where Z is the confidence level, σ is the standard deviation, and n the sample size. The relative error along the x-axis is 3% of the values and finds its origin in the evaluation of the average stress between the nanoplanes. The relative error along the y-axis is estimated to be 5% of the values and is related to the uncertainty of the start position of the transition towards a chaotic regime. For the sake of clarity, the error bars are not presented in the graphs.

By linearly fitting the data points, a visual assessment of the validity of the initial hypothesis – *nanoplanes form independent tensile tests* – is provided. As shown in Fig. 59, the experimental data form a single straight line in accordance with Eq. (4.7) with high level of confidence. The nominal stress σ_N and the shape parameter, m , are obtained ($m = 2.1 \pm 0.1$ and $\sigma_N = 1.1 \pm 0.1 \text{ GPa}$). The shape parameter is low, indicating the need of further calibration of the process. This can be achieved by testing a surface with known Weibull parameters.

The theoretical fracture value for bulk fused silica is estimated in the order of 21 GPa , indicating that it fails due to the presence of surface flaws on its surface. Here, the maximum stress obtained reaches 1.7 GPa with a corresponding 80% failure probability. This value is lower, yet in the same order of magnitude with the reported ones in Chapter II via the use of the tensile tester. Notwithstanding, in this case we test the surface of the pristine material; the tensile testing instrument is testing the surface of the laser processed material.

ii) Further validation: Effect of surface quality on mechanical strength

It has been reported by a plethora of works [60, 123, 124] that chemical etching of glasses in hydrofluoric acid (HF) improves the mechanical resistance of the material's surface. More specifically, for the case of fused silica it has been demonstrated that chemical etching in HF does not change the average surface roughness; yet it improves the so-called geometric average slope parameter, Δq [60]. This parameter indirectly provides information for the density of peaks contained in a given profile, and in this specific case, decreases as the etching time increases. More information about the surface parameters can be found in Appendix C.

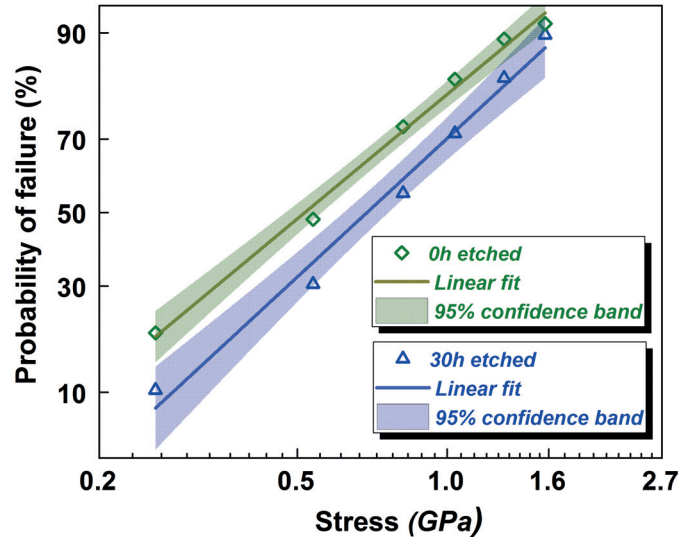


Fig. 60. The graph represents the probability of fused silica of two different surface qualities to fail under a certain stress level. The green line represents an un-etched specimen, while the blue one an etched one. The etched specimen is prone to fail at higher stresses indicating the significant impact of the surface quality in the mechanical tests.

To verify the effect of the bulk in our tests as well as further validate our experimental method, we chemically etch our specimen for thirty hours in low concentration 2.5% HF. This is expected to improve the mechanical resistance of the material and impact on its fracture statistics. After the etching and a subsequent rinsing step, we exposed the specimen under the similar conditions with the specimen tested in Fig. 59.

As shown in Fig. 60, the probability of failure in the case of the etched fused silica (represented by the blue line in the graph) is lower. The single datapoint (out of the six in total) at the highest stress level where the confidence bands of the two graphs coincide is an outlier since the traffic (ρ defined in our queuing system) cannot be defined at very high values, and therefore, strict independence of the lamellae is not guaranteed. Overall, this result provides firm validation that the surface of the material -and not the volume- is tested.

By comparing the two cases, the one shown in Fig. 59 and the un-etched one shown in Fig. 60, we observe that for higher pulse energy (Fig. 60) the probability of failure is decreasing, i.e., the probability of failure for a load of 1 *GPa* is 55% for the pulse energy of 188 *nJ* while 80% for the pulse energy of 196 *nJ*. The dependency on the pulse energy is attributed to the presence of minor ablation taking place at higher pulse energies.

iii) Testing other brittle materials: Sapphire and α -quartz

As a step towards exploring the genericity of the phenomenon, we postulate that it applies to a broad number of brittle materials that nanogratings may be found.

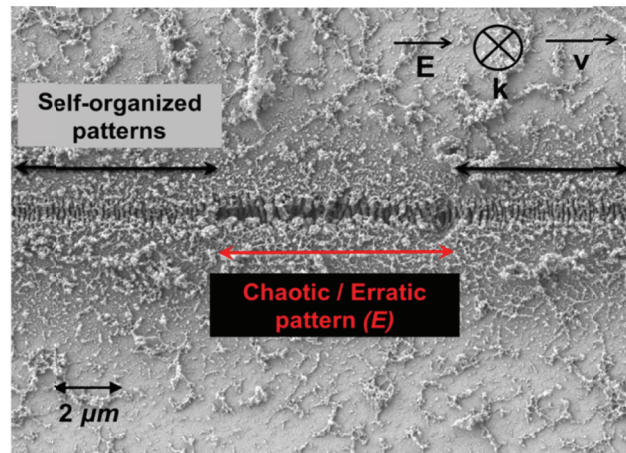


Fig. 61. Scanning electron microscope image of laser processed line indicating the scanning direction (v), the polarization (E), and the pattern written on a sapphire substrate. The black lines indicate regular patterns, while the red erratic ones. For producing this specific line, there are about 80 pulses overlapping each unit volume providing net fluence of 6 J/mm^2 . Note that close to the processed line a dense network of nano-scale particles that self-organize into semi-structured networks is formed.

We, therefore, investigate sapphire [125] and α -quartz [126] that combine the presence of nanogratings as well as may follow Weibull statistics in their fracture. The conditions of exposure are similar to the ones used for the case of fused silica. The pulse energies of 192 nJ and 188 nJ are found favorable for producing the most interesting results in α -quartz and sapphire, respectively.

Fig. 61 shows a scanning electron microscope image of the intermittency on a sapphire substrate. There is a firm distinction between the regimes where self-organized patterns and chaotic patterns appear. Nevertheless, in the case of sapphire a dense network of nano-scale particles that self-organize into semi-structured networks is formed within a few microns from the processed line which can open up perspectives for novel applications [127].

Similarly to the case of fused silica, we observe that for both sapphire and α -quartz, as the deposited energy increases, the length and frequency of erratic patterns increase as shown in Fig. 62. We investigate whether the QS metaphor may be validated.

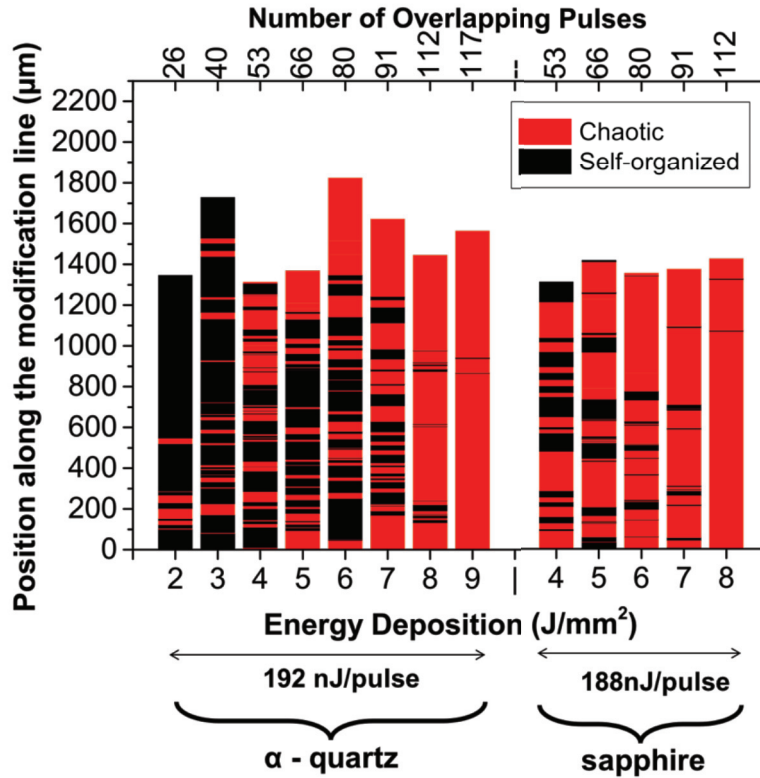


Fig. 62. Overview of the transitions for different energy depositions and pulse energies for sapphire and α -quartz. Black regions represent the self-organized patterns and the red ones the chaotic patterns.

As summarized in Table 3, both materials present a striking similarity to the Geo/G/I queuing system analogy. This result indicates that the technique may be generic and applicable to a broad range of materials, pending a method to link the stress and the deposited energy in each of them.

Sapphire			α -Quartz		
192nJ			188nJ		
0.94	0.89	0.05	0.68	0.68	0.00
0.70	0.73	0.03	0.85	0.99	0.14
0.77	0.66	0.11	0.62	0.84	0.22
0.24	0.15	0.09	0.68	0.60	0.08
$E\{\Theta_i\}/E\{\Theta_j\}$	$(1-\rho_i)/(1-\rho_j)$	Absolute difference	0.55	0.21	0.34
			0.22	0.14	0.08
			$E\{\Theta_i\}/E\{\Theta_j\}$	$(1-\rho_i)/(1-\rho_j)$	Absolute difference

Table 3. Summary of the queuing theory results for α -quartz and sapphire. In both cases, the system follows the dynamics of the Geo/G/1 QS. For the calculations, measured values of $E\{\Theta_i\}$ and ρ_i are used to validate the left and the right part of Eq. (4.7). Values within 0.15 range are represented in green colour, while outliers are represented in red colour.

E. State-of-the-art nanogratings formation models and discussion

Let us now discuss the state-of-the-art knowledge on the formation of the self-organized patterns *per se* (nanogratings), and the contribution of our discovery to their further understanding.

Since the initial observation of the nanogratings [83], the phenomenon has been widely investigated in numerous dielectrics. Nevertheless, a profound ambiguity still holds regarding the formation of these peculiar self-organized patterns. Two solid models have been proposed so far as tentative explanations of the nanogratings formation.

The first model [83] is based on the interference of the laser field with the field of the bulk electron plasma wave. More specifically, when femtosecond laser pulses interact with fused silica, multi-photon ionization takes place, producing high density of free electrons when the laser interacts with glass. A plasma (can be realized as an electrically conductive fluid) forms, which linearly absorbs the following laser light pulses through the inverse bremsstrahlung mechanism. The bulk electron plasma wave is excited by the absorption of the laser light in the electron plasma. A periodic structure is produced as a result of the interference of incident light and the excited bulk electrons of the electron plasma, leading to the modulation of the plasma's concentration, and subsequently resulting to structural changes in the material.

The second model [82] explains the nanogratings formation with a nanoplasmonic model based on the enhancement of the electric field due to inherent defects in the material, such as color centers. Electrons or holes are trapped in the point defects and their ionization potential is reduced so that they can be ionized easier than other electrons in the atoms. Eventually, this reduced ionization threshold at the defects at the defects sites leads to the production of nanoplasmas. The nanoplasmas locally enhance the electric field producing modulated structural changes.

The first model holds a valid explanation on the dependence of the nanogratings period from the irradiation wavelength. However, it does not explain why nanogratings are a cumulative phenomenon (present after tenths of pulses), while interference is present from the early start of the interaction. The second model does not provide solid arguments on how self-organized patterns appear based on the defects randomly distributed in the material. For a more detailed discussion and argumentation on the validity of the two models, we refer the interested reader here [61].

Studying the dynamics of the nanogratings formation would require experimentally demanding pump-probe experiments and is out of the context of this thesis. Our analysis on the intermittent behavior is based on observations of the laser written patterns. The bottom-line of our model, in the context of further understanding the nanograting formation, is the significant presence of mechanical stress very close to the nanogratings regions. Furthermore, previous works have revealed the presence of minor cracks forming at the tips of the nanogratings at pulse energies lower than the ones used in this work. These findings point out the necessity of the nanogratings models to take into consideration the presence of mechanical effects to fully capture their formation mechanism.

F. Conclusion

In what precedes, we investigated the intermittent behavior of self-organized nanopatterns and chaotic patterns on the surface of brittle materials (fused silica, sapphire, α -quartz) when exposed to femtosecond laser pulses. Using queueing theory, we unraveled striking similarities with the intermittency that we used to demonstrate that the formation of each nanoplane formed within the self-organized patterns is independent of each other. This key finding, in conjunction with our previous knowledge of the stress generation associated with the formation of these nanoplanes, lead us to conjecture that each single lamella formation is equivalent to a single ‘loading’ experiment.

We proved that the intermittent behavior finds its roots in the fracture mechanics of the material. From the number of nanoplanes formed before fracturing the material, one can extract important parameters of the glass’ surface mechanics, such as the Weibull parameters commonly used for defining the probability of rupture for brittle materials. Further calibration of the method is needed for the accurate extraction of the Weibull parameters. As a first step towards the calibration of the method is its comparison to established methods.

Overall, this methodology offers a *straightforward and contactless method* for extracting fracture data of surfaces and yet with minimal amount of material used, as the affected zones is of micro-scale and confined to a small surface. It opens new opportunities for rapid diagnosis of surface strength, for instance for quality control of consumer electronics and other fields, a quality control test that is currently hard to implement; but also for further analyzing the behavior of brittle materials at the nano-scale.

Chapter V - PROOF-OF-CONCEPT: STRESS-BASED POLARIZATION DEVICE

Based on the publication:

B. McMillen, C. Athanasiou and Y. Bellouard, "Femtosecond laser direct-write waveplates based on stress-induced birefringence" in *Optics Express*, vol. 24, no. 24, pp. 27239-27252, 2016.

A. Introduction

In Chapters II and IV, we have proposed methods to explore the mechanics of glass at small scales and, more specifically, we extracted the material's statistical fracture information.

In Chapter III, we have investigated the long-term stress behavior of fused silica under different loading and environmental conditions. The effect of humidity triggers stress relaxation phenomena at tensile stresses above 1.6 *GPa*. At lower stresses, there was no obvious change of the stress evolving over time.

In this chapter, we apply the knowledge we accumulated in the previous chapters on fused silica's mechanical behavior to demonstrate a technique for manufacturing polarization devices.

More specifically, we present a technique for manufacturing polarization devices by controlling the stress in the material. Once the device geometry is defined; we use a femtosecond laser to locally induce stress in specific regions within the bulk of the material. The action of the induced stress to a particular aperture of the material results to birefringence. Unlike other techniques, which rely on direct light interaction with form-birefringent nanogratings [128], this clear aperture is free from laser-modifications, potentially affording higher power handling capabilities, higher overall device transmission, and a cleaner undistorted beam profile. Additionally, the use of fused silica substrates provides a broad transmission window, potentially enabling a wide tuning range for the operating wavelength. With fast fabrication times and full control over the device retardance, broadband-like devices consisting of many waveplates on a single substrate are possible. Furthermore, by using the same femtosecond laser for both machining and subsequent loading, the device manufacturing process can be greatly simplified.

B. Waveplate concept

The principle of a laser-machined waveplate is shown in Fig. 63. A rectangular clear aperture (labeled as zone c) is defined by two cuts made through a fused silica substrate using the femtosecond laser manufacturing process presented in the introductory chapter [1].

After etching, a set of lines (which we call 'stressors') are machined in the bulk of the material at opposing ends of the rectangle (b), using writing parameters sufficient to generate nanogratings within the laser-affected zone [83]. These nanogratings are oriented parallel to the laser writing direction, such that the principal component of the stress tensor [74, 129] is directed perpendicular to the line orientation.

This arrangement of opposing stressors induces a quasi-uniaxial loading of the material in the center (as indicated by the red arrows in Fig. 63), generating a sizeable optical retardance within the clear aperture. In this simple arrangement, the cuts serve as a stress-free interface.

As a result, the action of the stressors is confined to the area of interest, in which the level of optical retardance can be tailored through careful control of the number, density, and exposure parameters of the stressors.

It should be noted that while the fabrication process presented here is done in multiple steps, the action of machining and device loading could be combined prior to etching, simplifying the production process even further.

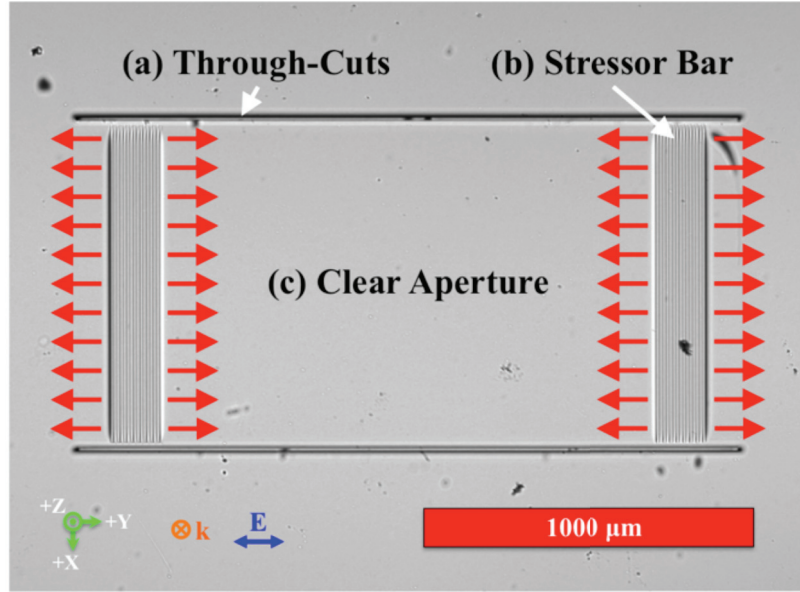


Fig. 63. Microscope image of a laser-machined waveplate. In this arrangement, a clear aperture (c) is defined by a pair of horizontal cuts (a), fabricated using the femtosecond laser machining process. Stress-induced birefringence is then generated in this aperture by writing a set of vertical lines (labelled ‘stressor bar’, (b)) within the bulk of the substrate at each end of the device, using exposure conditions sufficient to generate nanogratings. Here, the writing polarization, and hence the orientation of the nanogratings, is chosen such that the generated stress behaves like a quasi-uniaxial loading, as indicated by the red arrows.

C. Experimental procedure

i) Setup and measurement principle

Waveplates are fabricated in several steps, beginning with the machining of 20 blank devices (no stressors, each device $1 \times 2 \text{ mm}$, staggered on a 4 mm grid) in a $25 \text{ mm} \times 25 \text{ mm} \times 0.5 \text{ mm}$ fused silica substrate, using an amplified femtosecond laser system (Yb-fiber, Amplitude Systèmes), delivering 280 fs pulses at 1030 nm . Here, the laser is focused using a $20\times$ objective (NA 0.4). Following machining, the sample is etched in a

2.5% solution of hydrofluoric acid (HF) for eight hours. The repetition rate of the laser is set to 760 kHz during machining [1].

Using the same writing configuration, each device is loaded by incrementally forming stressors perpendicular to the cuts at both ends of the waveplate. The stressors are then arranged in blocks at each end of the waveplate at a fixed spacing of 5 or 10 μm , with the laser polarization set perpendicular to the writing direction in order to generate maximum stress along the long-axis of the waveplate (y -direction in Fig. 63) [74, 129]. Here, we define a single ‘stressor’ as a series of stacked discrete laser-modified regions with a z -spacing of 15 μm , forming a modified ‘sheet’ of material in the xz plane, for a total of 29 lines per sheet.

Each group of stressors is embedded in the bulk of the substrate and spaced 20 μm from all exterior surfaces to limit stress concentration and consequent crack formation. Additionally, each block is inset 100 μm from the ends of the device.

The resulting stress-induced birefringence was measured using an optical microscope (Olympus BX51) equipped with a liquid-crystal universal compensator for measuring birefringence (VariLC).

The measured retardance is a result of a change in dielectric permittivity due to applied stress, and is given by [130]:

$$\zeta_{ij} = \pi_{ijkl}\sigma_{kl}, \text{ where } i, j, k, l = 1, 2, 3 \dots \quad (5.1)$$

where π_{ijkl} is the fourth-rank piezo-optic tensor and σ_{kl} is the second rank stress tensor. The tensorial equation in matrix form for a biaxial planar stress in an isotropic material becomes:

$$\zeta_{(1..6)} = \begin{bmatrix} \pi_{11} & \pi_{12} & \pi_{12} & 0 & 0 & 0 \\ \pi_{12} & \pi_{11} & \pi_{12} & 0 & 0 & 0 \\ \pi_{12} & \pi_{12} & \pi_{11} & 0 & 0 & 0 \\ 0 & 0 & 0 & \pi_{14} & 0 & 0 \\ 0 & 0 & 0 & 0 & \pi_{14} & 0 \\ 0 & 0 & 0 & 0 & 0 & \pi_{14} \end{bmatrix} \begin{bmatrix} \sigma_1 \\ \sigma_2 \\ 0 \\ 0 \\ 0 \\ 0 \end{bmatrix} = \begin{bmatrix} \pi_{11}\sigma_1 + \pi_{12}\sigma_2 \\ \pi_{12}\sigma_1 + \pi_{11}\sigma_2 \\ \pi_{12}\sigma_1 + \pi_{12}\sigma_2 \\ 0 \\ 0 \\ 0 \end{bmatrix} \quad (5.2)$$

where the birefringence ellipsoid (Δn) view from the third axis (here the optical axis) is given in terms of ζ as:

$$(\Delta n)_3 = \left| \left(n_o - \frac{n_o^3}{2} \zeta_1 \right) - \left(n_o - \frac{n_o^3}{2} \zeta_2 \right) \right| \quad (5.3)$$

or

$$(\Delta n)_3 = \frac{n_o^3}{2} |(\sigma_1 - \sigma_2)(\pi_{11} - \pi_{12})| \quad (5.4)$$

and finally, the retardance is given by:

$$R = C |\sigma_1 - \sigma_2| t \text{ and } C = \frac{n_o^3}{2} (\pi_{11} - \pi_{12}) \quad (5.5)$$

where t is the thickness of the substrate, the value for C , the stress-optic coefficient for fused silica, is $3.55 \cdot 10^{-12} \text{ Pa}^{-1}$ [97].

Note that the above equations rely on the principal stresses found in the substrate, which for the case of the 2D analytical model must be computed from the x , y , and shear stress components using the following relation:

$$\sigma_1, \sigma_2 = \frac{\sigma_{xx} + \sigma_{yy}}{2} \pm \sqrt{\left(\frac{\sigma_{xx} - \sigma_{yy}}{2}\right)^2 + \tau_{xy}^2} \quad (5.6)$$

ii) Experimental results

We first examine the evolution of stress within the clear aperture of the waveplates as a function of deposited energy [92]. A pulse energy of 250 nJ is selected, corresponding to a laser-modification which lies solidly within the nanograting regime for optimal stress generation [74, 129]. The speed was varied from 1700 to $170 \text{ } \mu\text{m/s}$, resulting in a deposited energy range of 10 to 100 J/mm^2 . The results of this experiment are shown in Fig. 64 below.

For this experiment, the line spacing of individual stressors is fixed at $10 \text{ } \mu\text{m}$, with a total of 16 stressors per side (32 per device). According to Fig. 64, the developed stress peaks around 20 J/mm^2 , giving a maximum retardance of just over 15 nm . Above this point the retardance begins to decay, which we interpret as a consequence of stress-relaxation due to crack formation within the nanogratings. This measurement not only serves as a calibration to develop maximum stress during the writing process, but also confirms previous findings for stress evolution in the nanograting regime [75]. For reference, the phase shift at 546 nm (the wavelength used by the VariLC measurement system) is given on the right-hand side of the graph.

While the peak retardance developed in Fig. 64 is only on the order of $\sim 15 \text{ nm}$, this plot serves as a calibration for process control to determine the best writing conditions for generating stress in a single line. For further optimization of the developed stress, we now turn our attention to the lateral spacing of the stressors.

Based on the results shown in Fig. 64, a deposited energy target of 20 J/mm^2 is chosen to fabricate three additional devices: one with a stressor spacing of $10 \text{ } \mu\text{m}$ and 64 total stressors, and two with a reduced spacing of $5 \text{ } \mu\text{m}$, each with 64 and 128 total stressors, respectively. The results are shown in Fig. 65 below. The device in Fig. 65a is the same displayed in Fig. 64, and is used as a reference (20 J/mm^2 , $\sim 15 \text{ nm}$ max retardance).

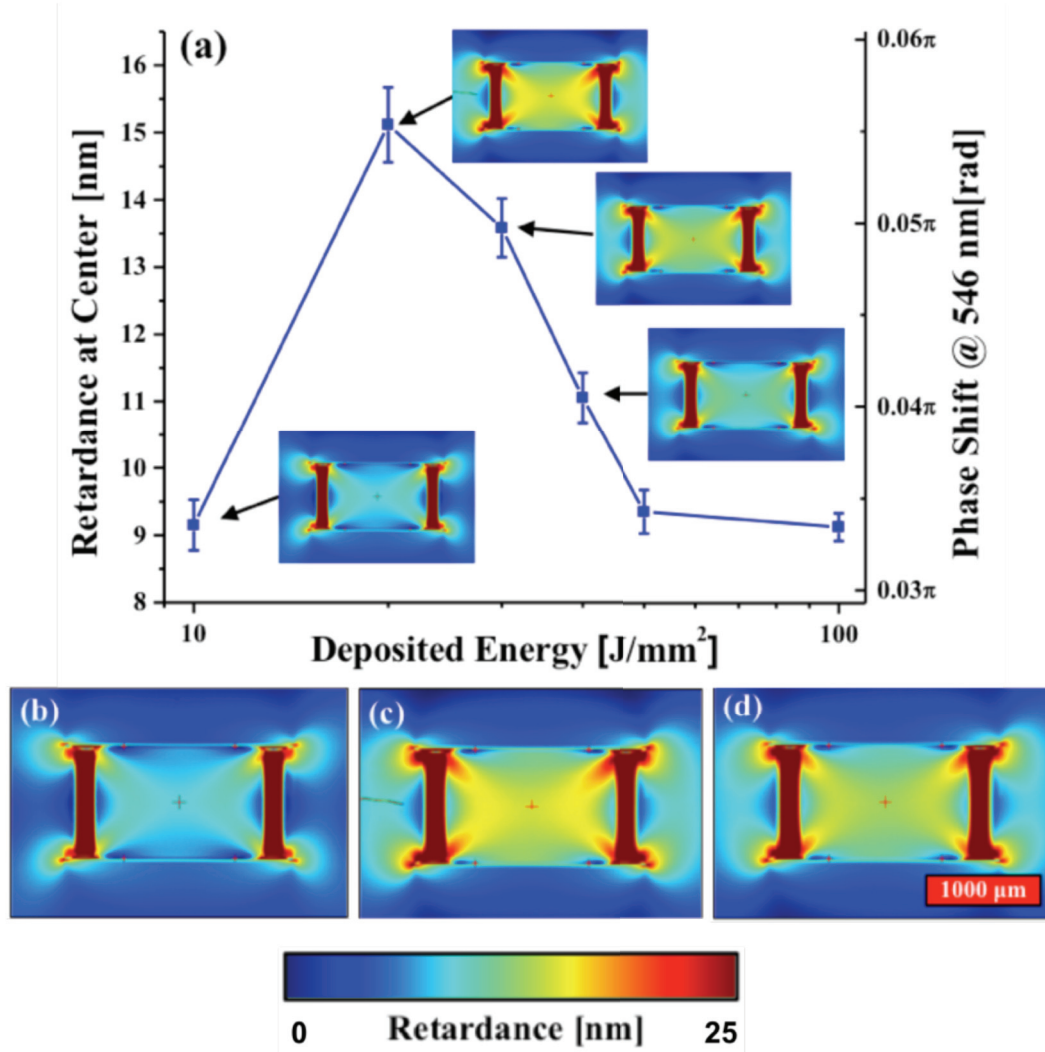


Fig. 64. Retardance as a function of the energy deposited for a pulse energy of 250 nJ and a line spacing of 10 μm . All devices are written with 16 stressors per side (32 stressors total per device). For these writing conditions, it is found that the stress peaks for a deposited energy of 20 J/mm². The images in (b - d) show a magnified view of the retardance map for three waveplates spanning the range over the peak shown in (a), with deposited energy values of 10, 20, and 30 J/mm², respectively.

Here we measure the developed retardance at the center of the clear aperture as a function of the spacing and number of lines in each stressor. Note that the retardance scale has a maximum retardance of 100 nm. For the device shown in Fig. 65d, a maximum retardance of ~ 55 nm is developed. This retardance map will be used as a comparison and calibration in the following section on device modeling.

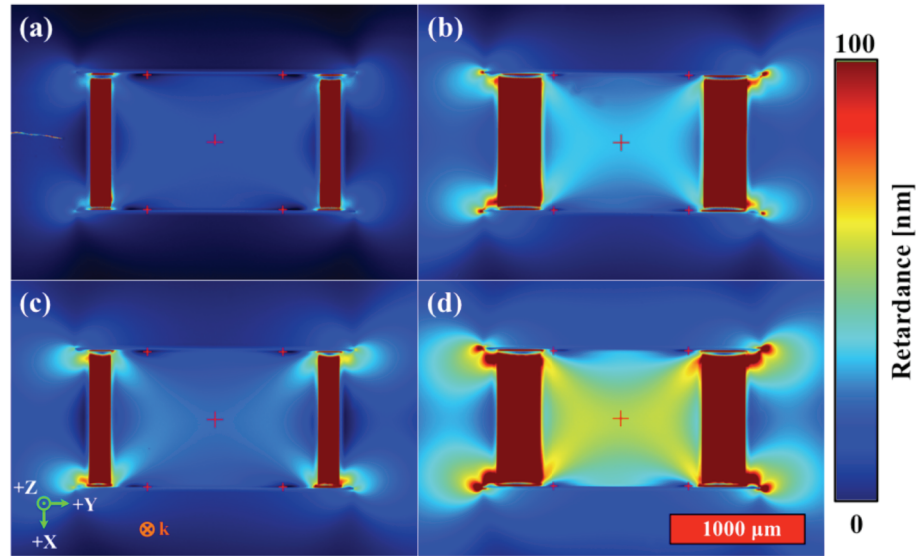


Fig. 65. Waveplate retardance as a function of the number of stressors and stressor spacing. (a) and (b) show retardance maps for a stressor spacing of $10\ \mu\text{m}$ with 16 and 32 stressors per side, respectively. Devices (c) and (d) are similar, but for a stressor spacing of $5\ \mu\text{m}$ with 32 and 64 stressors per side, respectively. All devices were written with a deposited energy of $20\ \text{J}/\text{mm}^2$, with the laser polarization fixed parallel to the long axis of each device. For comparison, the device shown in (a) has a peak centre retardance of $\sim 15\ \text{nm}$, while the device in (d) is considerably higher at $\sim 55\ \text{nm}$.

D. Modelling and Discussion

We now set out to describe the behavior of the developed stress in the waveplates in terms of a set of design parameters, such as the device geometry and the number and density of the stressors. These models may then be used as a set of design rules, giving full control over the stress field under different geometrical and loading conditions.

i) One-dimensional analytical model

As a first approximation, we consider a one-dimensional lumped model (illustrated in Fig. 66 below). Here the modified and unmodified regions of the material are represented by springs, for which an equivalent stiffness is derived.

In this model, the geometry of the waveplate is broken down into several distinct regions, as shown in Fig. 66a. These regions are labeled as the stressors (composite laser modified volume), the un-affected sidebars, and the clear aperture of the waveplate. Each of these regions may then be represented by an equivalent stiffness as shown in Fig. 66c.

The model is built by first considering the composite region containing each stressor block, which is treated as a parallel and series combination of springs and assigned an equivalent

stiffness, K_D , as illustrated in Fig. 66c. This assembly is then placed in series with the clear aperture of the waveplate, K_{WP} .

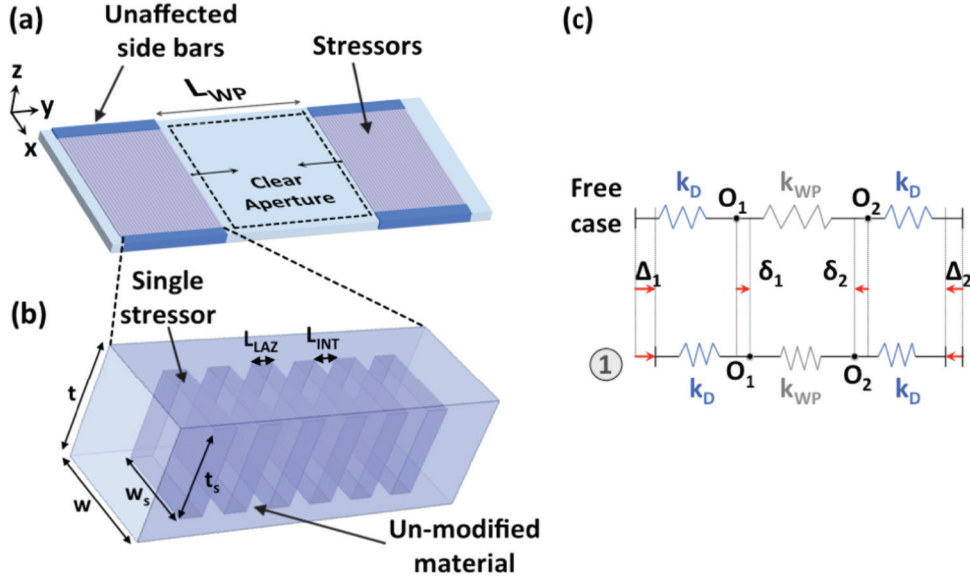


Fig. 66. (a) 3D visualization of a waveplate, highlighting the various regions taken into consideration in the 1D spring model. (b) Expanded view of the stressor region, showing the composite nature of the structure. (c) Lumped spring model used to predict the retardance in the centre of the clear aperture as a function of the number of stressors.

After formulation of the total stiffness of the system, and taking into account stress-induced birefringence, we arrive at the following expression for calculating the retardance in terms of the number of stressors, n :

$$R = C\sigma t = \underbrace{\left(\frac{E_{SiO_2}}{\text{Material}}\right)}_{\text{Material}} \underbrace{\left(\frac{\epsilon_{LAZ}}{\text{Laser}}\right)}_{\text{Laser}} \underbrace{\left[nt \frac{\alpha}{\left(1 + \frac{L_{WP}}{L_{INT}}\lambda\right)}\right]}_{\text{Geometry}} \quad (5.7)$$

where the factor λ is given by:

$$\lambda = \frac{1}{n} \left[\frac{2(1-\beta)}{\alpha + \left(1 - \frac{1}{n}\right)} + \frac{\beta}{\kappa\alpha\gamma + \left(1 - \frac{1}{n}\right)} \right] \cong \frac{1}{n} \left[\frac{2(1-\beta)}{\alpha + 1} + \frac{\beta}{\kappa\alpha\gamma + 1} \right] \quad (5.8)$$

The parameters α , β , and γ are dimensionless ratios, defined as $\alpha = L_{LAZ}/L_{INT}$, $\beta = t/t_s$, and $\gamma = w/w_s$, respectively, while κ is the ratio of the Young's modulus of pristine SiO_2 to that of laser modified SiO_2 . The quantities w_s , t_s , w , and t are the width and length of a stressor and surrounding material, respectively, while the quantities L_{INT} and L_{LAZ}

correspond to the spacing between laser-modified regions (vertical sheets) and the thickness of these regions (along the y -direction), respectively. C is the stress-optic coefficient, L_{WP} is the initial length of the clear-aperture, E_{SiO_2} is the elastic modulus of fused silica, and ϵ_{LAZ} is the net volumetric expansion induced during laser exposure [75].

From a design point of view, Eq. (5.7) gives an overview of the tuning parameters available to the user. The choice of Young's modulus is fixed by the choice of fused silica (material component), while the induced strain (laser-induced component) is also relatively fixed for optimized stress generation, as demonstrated by the waveplates shown in Fig. 65. This leaves device geometry as the main parameter, and we note that, for large numbers of stressors, the parameter λ converges to zero, leaving only the ratio of the stressor spacing, material thickness, and the number of stressors.

It should be noted that this model is a simplification, as the interfacial energy between the various domains (laser-affected, pristine, etc.) is not considered. However, so long as we assume that the behavior of these regions is governed by linear elasticity, this approximation remains valid. Despite these subtleties, the mechanical behavior of the system is reasonably well predicted using this approach.

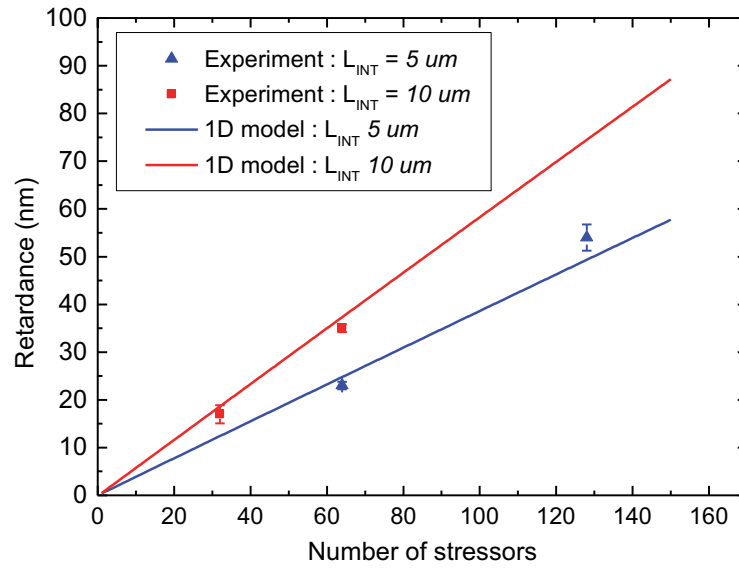


Fig. 67. Prediction of waveplate retardance as a function of the number and spacing of machined stressors using the 1D stiffness model. Here, the individual data points the developed retardance in each waveplate (measured in the centre of the clear aperture for each device shown in Fig. 65), while the curves are the predicted values based on the model. For each measured data point, the error was estimated from the measurement noise, which on average was not greater than $\pm 1 \text{ nm}$. The reader should note that the measured data points shown in the above graph compare different sizes of clear aperture. The devices written with 32 stressors $10 \mu m$ spacing and 64 stressors $5 \mu m$ spacing have the same clear aperture size, while conversely the second two data points are also comparable.

In addition to the simplifications mentioned, we make the following assumptions:

- Fine structures within the laser-modified composite are ignored, and instead treated as a homogeneous material with a lower density than the surrounding, unmodified bulk. An average elastic modulus of 34 GPa was chosen for this region, which was reported in [57].
- For the particular arrangement of embedded stressors used here, a certain portion of the device loading is transferred to the bulk as shear stress; in this case along the regions label ‘unaffected sidebars’. We consider this shear low and negligible.

Fig. 67 plots the developed retardance as a function of the number of stressors, comparing the predicted retardance based on the 1D model with the measured values from the center of each waveplate shown in Fig. 65.

Overall, the model is in good agreement for low and high numbers of stressors, however there is some deviation for higher numbers of stressors. While this model provides a reasonable estimation, the accuracy it provides is limited, as we do not consider the 2D interaction of stress present in the waveplate. For an improved model, we now examine the full 2D structure, which we cover in the next section.

ii) Two-dimensional analytical model

While the simplified 1D model discussed in the previous section provides an adequate approach to predicting stress evolution from the number and density of machined stressors, it does little to describe the full contour of the induced retardance field.

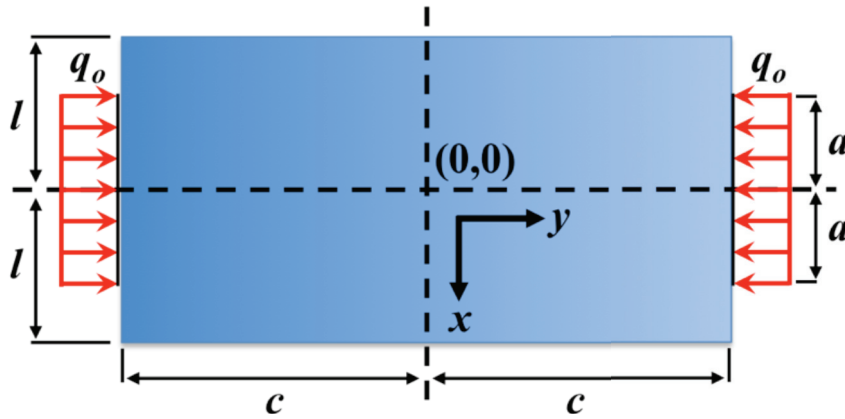


Fig. 68. Schematic representation of the loading case considered for the two-dimensional model. The terms here represent the dimensions of the waveplate (c, l), as well as the applied stress (q_0) and the area over which it is distributed (a).

For an analytical derivation of this full contour, we use a more refined model based on Airy stress functions [131-135]. In this model, the waveplate is treated as a two-

dimensional body (finite rectangular domain) with a continuously distributed load along the width (provided by the action of the stressors), as depicted in Fig. 68.

While a full derivation on the use of Airy stress functions is beyond the scope of this work, we will briefly outline the process here, referring to the notation used in Fig. 68. Here, we assume a right-handed coordinate system, the origin of which is taken to be in the center of the rectangle defining the clear aperture. Following the work in [134], a general solution to the stress developed in the waveplate is found by defining a stress function $\varphi(x, y)$, which satisfies the biharmonic equation:

$$\frac{\partial^4 \varphi}{\partial x^4} + 2 \frac{\partial^4 \varphi}{\partial x^2 \partial y^2} + \frac{\partial^4 \varphi}{\partial y^4} = 0 \quad (5.9)$$

The equation $\varphi(x, y)$ is of the form:

$$\varphi(x, y) = \sin \frac{m\pi x}{l} f(y) \quad (5.10)$$

where m is an integer, and y is the only independent variable of $f(y)$. Substituting Eq. (5.10) into Eq. (5.9), and making the substitution $\alpha = m\pi/l$, leads to the following equation for determining $f(y)$:

$$\sin(\alpha x)[f^4(y) - 2\alpha^2 f^2(y) + \alpha^4 f(y)] = 0. \quad (5.11)$$

The stress function then becomes, after integration of Eq. (5.11):

$$\varphi(x, y) = \sin(\alpha x)[C_1 \cosh(\alpha y) + C_2 \sinh(\alpha y) + C_3 y \cosh(\alpha y) + C_4 y \sinh(\alpha y)] \quad (5.12)$$

where the coefficients $C_1 - C_4$ are computed using the boundary conditions of the substrate at the upper and lower edges ($y = \pm c$). In order to accommodate generalized representations of the load applied to one edge of the substrate, a Fourier series is used, as follows:

$$q(x) = A_o + \sum_{m=1}^{\infty} A_m \sin(\alpha x) + \sum_{m=1}^{\infty} A'_m \cos(\alpha x), \quad (5.13)$$

with an additional loading term computed for the lower edge. For our case of symmetrical loading, the terms containing $\sin(\alpha x)$ vanish from Eq. (5.13), and the coefficients A_o and A'_m may be computed by:

$$A_o = \frac{q_o a}{l}, A'_m = \frac{1}{l} \int_{-a}^a q_o \cos(\alpha x) dx = \frac{2q_o}{m\pi} \sin(\alpha a). \quad (5.14)$$

Here, A_o represents the uniform load applied to the right-hand edge. Finally, the 2D stress tensor is related to the stress function by:

$$\sigma_{xx} = \frac{\partial^2 \varphi}{\partial y^2}, \sigma_{yy} = \frac{\partial^2 \varphi}{\partial x^2}, \text{ and } \tau_{xy} = \frac{\partial^2 \varphi}{\partial x \partial y} \quad (5.15)$$

where σ_{xx} , σ_{yy} , and τ_{xy} are the x , y , and shear components of stress, respectively. Computing the derivatives of Eq. (5.12), we arrive at the solutions that satisfy the biharmonic equation, giving a full tensorial description of the stress field in the clear aperture of the waveplate:

$$\begin{aligned} \sigma_{xx} &= \frac{q_o a}{l} + \frac{4q_o D}{\pi} \sum_{m=1}^{\infty} \frac{\sin(\alpha a)}{m} \frac{[ac \operatorname{ch}(ac) - sh(ac)]ch(\alpha y) - \alpha y sh(\alpha y)ch(ac)}{sh(2ac) + 2ac} \cos(\alpha x) \\ \sigma_{yy} &= -\frac{q_o a}{l} + \frac{4q_o D}{\pi} \sum_{m=1}^{\infty} \frac{\sin(\alpha a)}{m} \frac{[ac \operatorname{ch}(ac) - sh(ac)]ch(\alpha y) - \alpha y sh(\alpha y)ch(ac)}{sh(2ac) + 2ac} \cos(\alpha x) \\ \tau_{xy} &= \frac{q_o a}{l} + \frac{4q_o D}{\pi} \sum_{m=1}^{\infty} \frac{\sin(\alpha a)}{m} \frac{ac \operatorname{ch}(ac)sh(\alpha y) - \alpha y ch(\alpha y)sh(ac)}{sh(2ac) + 2ac} \sin(\alpha x) \end{aligned} \quad (5.16)$$

Where $\alpha = \frac{m\pi}{l}$, q_o is the applied stress, D is a calibration factor whose presence will be explained in the next paragraph, $ch = \cosh$, and $sh = \sinh$.

Finally, for the equations shown above, we compute the stress components for the first fifty orders of the Fourier series, which we find adequately describes the stress-field developed in the clear aperture.

iii) Comparison with experimental results

Fig. 69 illustrates a comparison between experimental data and the analytical model for line profiles taken along the x and y directions through the center of the clear aperture. For reference, the retardance map for the peak device in Fig. 65d is shown in Fig 69a.

We first examine the prediction of the shape of the stress field. Qualitatively, the 2D model Fig. 69b is in good agreement with the contour of the measured retardance. While the 2D model performs well for the contour, the overall magnitude variation is not properly estimated, as shown by the line profile plots for the y and x directions in Fig. 69c and Fig 69d, respectively. The upper insets show the analytical model prediction, and while the shape of the profile closely follows the measurement, the overall magnitude is incorrect.

We attribute this to a slight out-of-plane deformation, suggesting that the loading induced by the stressors requires further optimization. Indeed, no compensation for spherical aberration was used during the writing process, as discussed for the tensile tester in Chapter II. This can account for a decrease of localized intensity with increased writing depth, resulting in a slightly unequal distribution of stress across the substrate thickness.

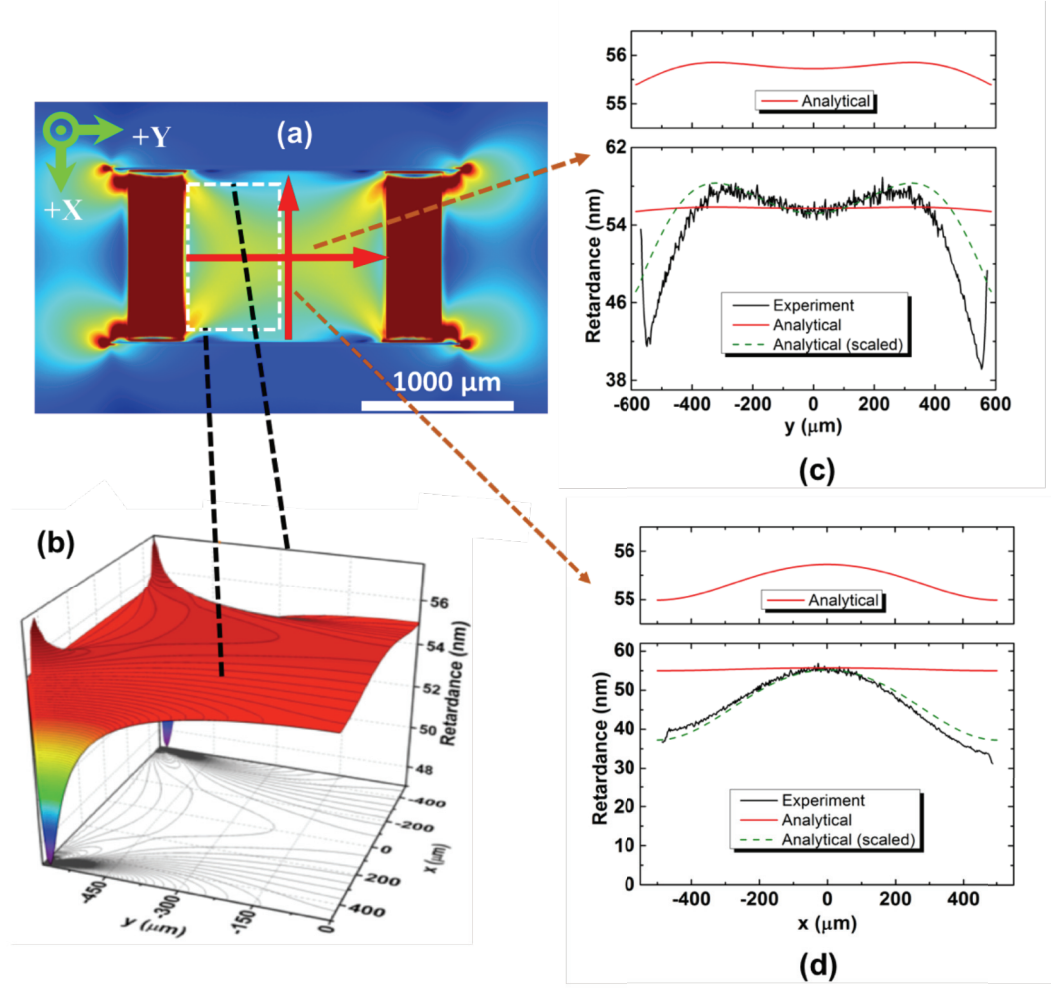


Fig. 69. (a) Retardance map for the peak device shown in Fig. 65(d) (55 nm, 128 stressors, 5 μm spacing). (b) 3D view of the retardance profile calculated using the 2D analytical model (only half the computed map is shown). (c - d) comparison between retardance data obtained for experimental measurements and the 2D analytical model for the y and x profile directions, respectively.

The stress gradient generates a net moment, and in turn favors out-of-plane bending. To adjust the analytical model, we have included a scaling factor (labeled as the variable D in Eq. (5.16), which is shown here for a value of 25, indicating that the overall prediction of the 2D model is in agreement with the measurement, provided that this adjustment is made. We call the reader's attention to the fact that this is an artifact for curve fitting. The exact physical meaning of the parameter D in terms of stress remains unclear at this stage.

E. Conclusion

In this chapter, based on the knowledge we developed on the mechanics of fused silica (its fracture statistics and relaxation behavior) in the previous chapters, we have proposed a

methodology to design compact stress-based polarization devices. As an example, a basic geometry was used, consisting of a series of vertical, laser-written planes arranged in a perpendicular fashion (similar loading scheme with the one used to load tensile testing device in Chapters II and III), creating a rectangular region under uniaxial compressive stress of 260 MPa .

From the design perspective, the results presented in this chapter are not fully optimized. Nevertheless, we have provided a generalized framework for manufacturing complex polarization devices. The flexibility of the direct-write process allows for virtually infinite combinations of cuts and stressors, opening up new design opportunities for more complex polarization devices with clear apertures. For example, one could consider devices based on two-dimensional stress states (as demonstrated in [136] at the macro-scale), leading to the creation of optical vortices. The technique we have introduced here allows for such a concept to be implemented at the micro-scale, and may be tailored to a variety of complex stress states.

Further development of the technique requires extensive knowledge of the properties of the material used as a substrate. Thus, the necessity of using the mechanical testing methods proposed in Chapters II and IV for extracting material information is unraveled.

Chapter VI - CONCLUSIONS & DISCUSSION

A. Retrospective

Until recently, suitable methods and available instrumentation for investigating the mechanical properties of glass in arbitrary shapes were missing, hampering the development of glass-based microdevices as well as the investigation of fundamental challenges of glass mechanics in small scales. In this thesis, we made use of femtosecond laser processing which proved to be a unique platform to explore fundamental and unresolved issues related to the study of the strength of glass. Two novel experimental approaches were proposed: one based on a novel concept of a monolithic tensile tester, and a second one, based on statistical observations of an intermittent behavior occurring during laser exposure.

The main advantage of the monolithic tensile testing method in comparison to the existing methods is the *contactless* fabrication and operation of the instrument. Therefore, a full test is performed without the need to physically interact with the test specimen, overcoming the problems of manipulation and alignment.

The intermittent methodology offers a straightforward and contactless way for extracting fracture data of surfaces and yet with minimal amount of material used, as the affected zones is of micro-scale and confined to a small surface.

Using these two approaches, we were able to: firstly, observe a linear mechanical response of fused silica at the micro-scale, secondly, load it to unprecedented level of stress, thirdly, to measure relaxation effects of the material at high stress level, and finally to explore its fracture statistical behavior.

In the *first chapter* of the thesis, the existing experimental methods for mechanical characterization of materials at small scale were reviewed. The advantages and drawbacks of each method, in the context of micro/-nano- characterization of glass, were discussed.

In the *second chapter*, a novel technique to perform micro-tensile testing was proposed in which the material under test was itself sculpted into a tensile tester. The micro-tensile tester was fabricated by a femtosecond laser; yet, the same femtosecond laser was used as a loading tool to accurately apply a force to the test specimen and as a diagnostic tool allowing us to measure the generated displacements. The stress on the specimen was observed via photoelastic measurements. Therefore, fabrication, loading, and characterization of the device were performed without physically interacting it. As a proof of concept, we performed tensile testing of fused silica reaching stress levels up to 2.7 GPa. Furthermore, we extracted a shape parameter of $m = 10.9$ for the femtosecond laser processed silica. These results indicate that femtosecond laser machining combined with chemical etching can produce high performance mechanical parts with tensile strength at least 20 times above the recommended design value.

In the *third chapter*, we used the monolithic tensile tester to investigate relaxation phenomena in fused silica. We investigated the long-term mechanical behavior of the material under various stress levels and under controlled environmental conditions. At high stress and humidity levels, we revealed a relaxation behavior and subsequent failure of the material. We performed similar measurements at the same stress, yet lower humidity

levels. Neither any indication of relaxation behavior nor failure of the material was observed in this case. We used models from the literature to try to understand the relaxation behavior of the material; we attributed the effect to the influence of water molecules in the strained silica bonds and the subcritical crack growth.

In the *fourth chapter*, we investigated the intermittent behavior of self-organized nanopatterns and chaotic patterns on the surface of fused silica when exposed to femtosecond laser pulses. Using queueing theory, we unraveled similarities with the intermittency, which we used to demonstrate that the formation of each nanoplane formed within the self-organized patterns is independent of each other. From the number of nanoplanes formed, one can extract important parameters of the glass' surface mechanics, such as the Weibull parameters commonly used for defining the probability of rupture for brittle materials.

In the *fifth chapter*, based on the statistical fracture results as well as the relaxation behavior of fused silica we obtained in the previous chapters, we designed a polarization device which is fabricated and operated by a femtosecond laser. Though a simple geometry is used in this example, we provided a generalized framework for manufacturing complex polarization devices in glass. The direct-write process is contactless allowing easy manipulation and loading of the device. An additional laser exposure step can allow the integration of further functionalities on the same substrate. In comparison with the existing methods, the one introduced here, can potentially provide higher power handling capabilities and higher overall device transmission.

B. Future work

This work is expected to set the scene for the investigation of the mechanical properties of glass at small scales and serve as the backbone for future innovations in the use of glass in microdevices. In this subsection, the author provides a guideline for future work.

- *Provide the necessary design criteria to engineers/designers regarding the statistical failure of femtosecond laser processed fused silica.*

A novel technique to perform micro-tensile testing was proposed. As a proof-of-concept, we measured the stress-strain response of the material and extracted the Weibull parameters for a fixed set of exposure and etching parameters. For providing the design criteria needed for full exploitation of the material's properties, a parametric analysis (varying the exposure conditions and the etching time) is required to identify the optimal window of mechanical performance. Furthermore, more than thirty specimens need to be tested each time to provide adequate Weibull strength distribution.

- *Diversify the monolithic micro-tensile testing concept for various glasses and ceramics.*

The instrument is not only applicable for testing fused silica; it can be adapted for testing other materials, pending that an adequate specimen microstructuring process, compatible with the instrument fabrication process itself, is found. Thus, future works requires

identifying adequate exposure conditions and etching processes in the materials that may be of interest from the device development perspective.

- *Making use of the micro-tensile tester to characterize femtosecond laser-affected zones in glass.*

The femtosecond laser fabricated and operated micro-tensile tester offers a suitable platform for the investigation of the mechanics of femtosecond laser affected zones in glass with a simple additional exposure step. Indeed, the mechanical properties of femtosecond laser-induced polymorphic in silica are largely unknown which is a bottleneck into involving new material phases embedded in complex systems made of glass.

- *Quantify “pseudoplastic” deformation of glass at the nano-scale.*

At the nano-scale, silica glass is found to exhibit unconventional behavior such as “pseudoductility” [11-13]. Due to the lack of appropriate experimental tools this peculiar behavior could be identified, yet not quantified. The monolithic approach offers a suitable platform to explore glass mechanics at the nano-scale.

- *Investigation of stress relaxation behavior of fused silica under various experimental / loading conditions.*

In this work, first results were provided on the mechanical behavior of fused silica glass under high stress. To obtain these results, besides the tensile tester *per se*, an experimental setup where the user can tune the water content and automatically test more than one specimens for a long period of time was built. To further explore the rich topic of glass static fatigue under varied experimental conditions, investigation of the temperature dependence of this phenomenon needs to be investigated. Therefore, additional temperature control needs to be incorporated in the measurement platform.

- *Verification of the subcritical crack growth model resulting in the relaxation behavior and failure of fused silica.*

From the fused silica relaxation results perspective, mechanical testing in a heavy water environment would allow a further insight on whether the relaxation behavior originates on the surface or the bulk of the material. Furthermore, CO₂ laser morphing of the test specimen will allow an insight of whether the subcritical crack growth model is valid.

- *Investigation of crack propagation phenomena occurring during the intermittent behavior.*

The energy deposited is governed by three parameters, namely the pulse energy, the writing speed (scanning) and the repetition rate of the laser. A same level of deposited energy can be achieved by an ad-hoc selection of writing speeds and repetition rates. However, considering the crack propagation dynamics different patterns of alternating sequences of erratic and organized nanoplanes can be achieved for different pairs of

scanning speed / repetition rates, although they yield to identical amount of deposited energy into the material. A follow-up study may provide more information on the complex phenomenon of crack propagation in conjunction with the feed rate of pulses as well as the scanning velocity.

- *Calibration of the nanogratings technique using existing methods and investigation of the applicability of the model on sapphire and α -quartz*

Since there are not any reported results on the statistical fracture mechanics of fused silica specimens with the exact surface quality that we tested here, we cannot compare our statistics results. Nevertheless, calibrating the method is an important step for future studies. Furthermore, we were not able to explore further if the method is applicable to sapphire and α -quartz since we were not equipped with the proper equipment for producing the cantilevers required to evaluate the stress level between the nanogratings.

- *Development of monolithic glass optical and optomechanical devices at the micro-scale*

The flexibility of the femtosecond direct-write process demonstrated by the development of a polarization device, allows for virtually infinite combinations of cuts and stressors, opening up new design opportunities for more complex all-glass polarization devices with clear apertures and potentially zero transmission losses. The generic mathematical framework used can be exploited for developing devices based on two-dimensional stress states (as demonstrated in [136] at the macro-scale), leading to the creation of optical vortices.

APPENDIX

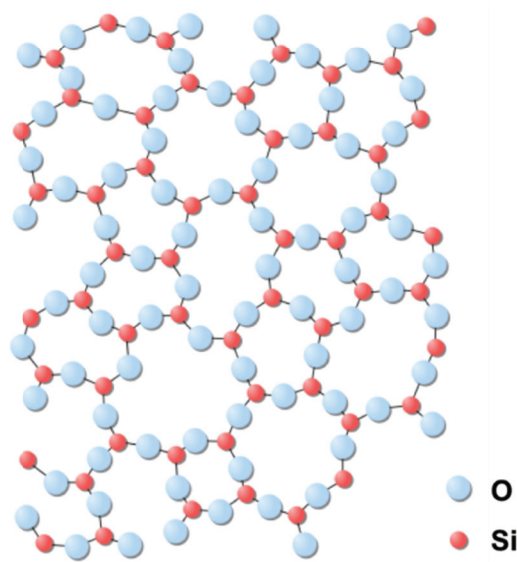
Appendix A: Fused silica properties

Fused silica, the non-crystalline form of silicon dioxide (SiO_2), differs from traditional mixed composition glasses (Pyrex, borosilicate, soda-lime etc.), which in addition to SiO_2 include ingredients such as Na_2O , CaO , and B_2O_3 . In contrast to them, fused silica is pure SiO_2 [137]. It offers another important advantage in comparison with other mixed composition glasses: there is no cluster formation of metals upon its processing.

Its purity is determined by the raw material, the manufacturing method and the subsequent handling procedures. Different types of fused silica exist [138]: natural silica glass with high levels of impurities (the most common impurities are metals – Al, Na and Fe or water which is present as OH groups and chlorine) as well as synthetic silica glass, manufactured from extremely pure precursors, with almost no impurities [3].

Synthetic fused silica	
Mechanical Properties*	
Elastic modulus	71.2 GPa.
Poisson's ratio	0.18
Optical Properties	
Refractive index	1.45 @ 580 nm
Transmission range	0.18 - 2.20 μm
Thermal properties	
Thermal conductivity	1.38 W/m $^\circ\text{K}$ @ 25 $^\circ\text{C}$
Thermal expansion coefficient	$0.48 \times 10^{-6}/\text{K}$ @ [-100,30] $^\circ\text{C}$

(a)



(b)

Fig. 70. (a) Basic optical, mechanical, thermal properties of synthetic fused silica. (b) Simplified two-dimensional representation of fused silica's structure. Its structural matrix consists of tetrahedral arrangement of oxygen (O) atoms and silicon (Si) atoms which form rings of varying sizes. As typical glass, it lacks long-range order (schematic adapted from Wikipedia/glass).

Fused silica consists of SiO_4 tetrahedral linked to each other to form rings of varying sizes (Fig. 70b). The basic optical, mechanical, and thermal properties of the material are illustrated in Fig. 70a.

Let us briefly review fused silica's properties that are relevant to microsystems technologies.

The fracture toughness K_{Ic} of the material (which measures its resistance against crack propagation) is low: between 0.5 to 1 $MPa\ m^{1/2}$, i.e., about 20 to 50 times less than that of common metals [10, 108]. Like other glasses, fused silica is also prone to static fatigue under constant loading due to stress-corrosion effects, i.e., spontaneous crack growth leading to a reduction of the fracture strength in the presence of water molecules.

Fused silica is clustered as *dielectric* [98] as it can hardly conduct current. Therefore, it can be used as an insulator with dielectric loss factor as low as 0.0004 at 1 MHz . Notwithstanding, unlike other insulators it does have second order electric characteristics since it can be polarized under an electric field. In other words, its atoms form dipoles which do interact with an electric field.

Its *thermal properties* include a remarkably low coefficient of thermal expansion ($0.48 \times 10^{-6}/K$ over the $-100^{\circ}C$ to $35^{\circ}C$ temperature range) and a high resistance to thermal shocks, which make it an excellent material for applications that require the utmost in dimensional stability over a large temperature range [98]. For comparison, the INVAR (nickel-iron alloy), which has the lowest thermal expansion among all metals and alloys near room temperature, has a mean coefficient of thermal expansion that is more than twice that the one of fused silica ($1.3 \times 10^{-6}/K$ over the $20^{\circ}C$ to $100^{\circ}C$ temperature range). Furthermore, it has one of the lowest thermal conductivities among solids ($1.38\ W/mK$ at $25^{\circ}C$), 100 times lower than that of silicon ($148\ W/m.K$ at $25^{\circ}C$).

Fused silica offers *optical properties* that compare favorably with other optical materials [98]. It is transparent from the deep ultraviolet (UV) to the infrared making it a very suitable material for high-end optical components and optical fibers.

Appendix B: Types of modifications in fused silica

Three types of structural modifications have been reported as a function of energy per pulse and pulse duration in fused silica. These regimes are labelled as Type I, II, and III [139] as shown in Fig. 71.

The *first regime* (Type I) is the one that homogeneous modifications take place within the laser affected zone (LAZ). In this regime, the material undergoes a slight increase of refractive index ($\Delta n = 5 \times 10^{-3}$) [140] and shows an increased etching rate [73]. The positive index variation makes waveguide fabrication possible [140].

The *intermediate regime* (Type II) is where self-organized patterns consisting of adjacent nanoplanes are formed (also called nanogratings) [82, 83, 141]. These structures are radically different than those found in the Type I regime as they are polarization dependent. They also present interesting optical properties such as form-birefringence [128], giving the possibility to create novel photonics devices such as polarization converters [142]. The presence of these nanostructures leads to strongly enhanced etching rates [143]. Moreover, nanogratings exhibit useful mechanical properties such as controlled volume expansion [75, 144]. The combination of the chemical and the mechanical properties found in the Type II regime leads us to use only this type of modification for all the devices presented in this thesis.

The *third regime* (Type III) is an inhomogeneous regime where the self-organized structures (nanogratings) collapse and become disorganized [145, 146]. At higher pulse energies, the ablation process starts.

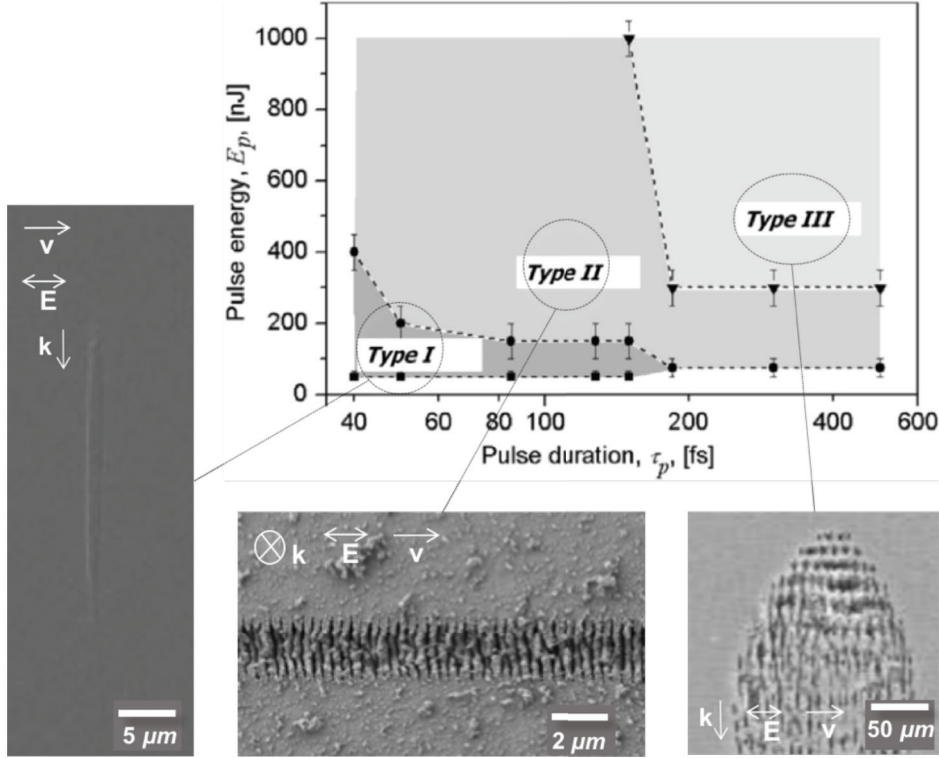


Fig. 71. The three regimes of structural modification that can be achieved by exposing fused silica with femtosecond laser pulses [139]. At low pulse duration (less than 200 fs), and low pulse energy (below 200 to 400 nJ) the homogeneous modifications (Type I) take place. At higher pulse energies, self-organized patterns form (Type II). At even longer pulse durations (more than 200 fs) and pulse energies (higher than 300 nJ) one can reach the inhomogeneous third regime (Type III). In the three insets, scanning electron microscope images of the three types of modifications are shown. The third inset showing the Type III regime was adapted from [147], while the first and the second are taken from our own data.

Femtosecond laser exposure in the Type I and II modification regimes can be used to machine transparent to the laser's wavelength materials like fused silica. This manufacturing method consists of two steps: the first one is the femtosecond laser exposure inducing modifications (described in the previous section) and a subsequent wet chemical etching step (in our case hydrofluoric acid – HF [72]), to dissolve the laser modified zones accessible to the acid [71, 73]. Following the etching part the sample is rinsed in de-ionized water and dried.

The typical etching rate of pristine fused silica is approximately 1 μm per hour for hydrofluoric acid of 2.5% [72]. The femtosecond laser exposure accelerates the etching

process up to typically a factor of 100 (in the Type II regime) and depending on the laser parameters.

For estimating the final shape of a designed contour the ratio of the modified fused silica to the surrounding pristine fused silica should be taken into account. This process has the capability of producing three-dimensional devices with aspect ratio typically of 1:100, or even higher when using KOH etchant.

Appendix C: Parameters influencing the femtosecond laser processing method

There are several parameters that influence the processing method, and therefore, the mechanical performance of the produced devices [61]. The major ones are discussed below:

- Pulse energy

Owing to the nonlinearity of the interaction, the energy per pulse defines the size of the interaction zone (Fig. 72). A simplified model describing this dependence can be found here [76].

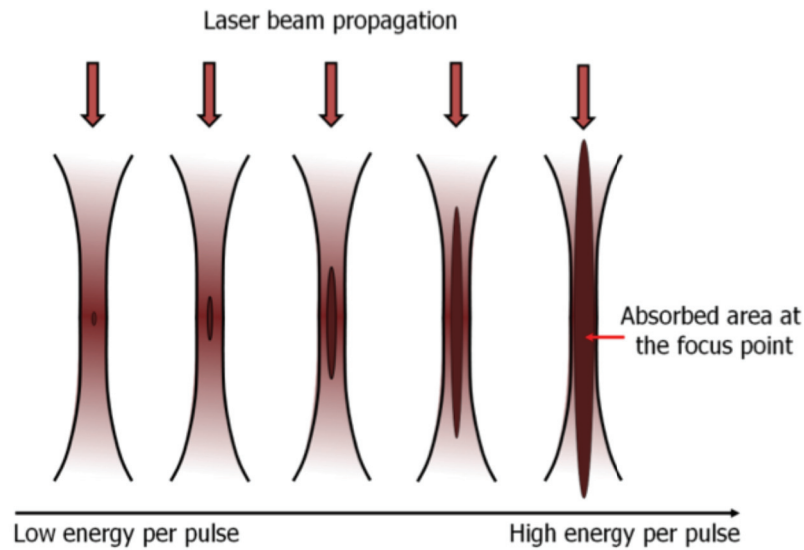


Fig. 72. Schematic on the evolution of the laser absorbed area according to the energy per pulse [61]. This is a simplistic view for the sake of understanding. As the pulse energy keeps increasing, further non-linear effects come into play resulting in a distorted laser modified zone along the propagation direction. However, the pulse energies considered in this work were such that it is reasonable to consider that the laser affected zone keeps an ellipsoid shape as depicted here.

- Deposited energy

The deposited energy (or net fluence) represents the total amount of energy deposited per unit surface in the material by the laser source [92]. It depends on the energy per pulse and the laser scanning speed as described by Eq. (4.2) in Chapter IV. Note that this formula provides a simplified view for conveniently comparing data. It does not describe the actual absorbed energy by the material (includes different coupled absorption mechanisms) which is challenging to be measured.

- Numerical aperture (NA) of the objective

The numerical aperture of the objective defines the size of the spot, and therefore, determines the focused peak power. The higher NA is, the higher the peak power will be.

- Polarization of the laser in respect to writing direction

Propagating light is a pulsating electric and magnetic field. The electric and magnetic components are oriented perpendicular to one another and can be spatially described by a triad of orthogonal vectors.

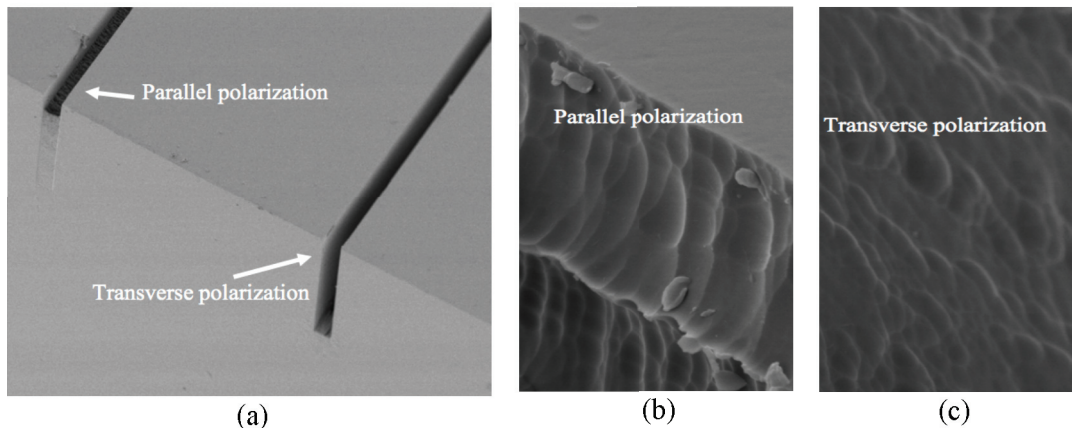


Fig. 73. (a) Effect of the polarization: the two trenches are exposed with the same energy and writing speed parameters but with two different polarizations. (b - c) Magnified view of the cut surface demonstrating the difference of surface quality in the two cases. In the case of the transverse the surface quality is higher [148].

The polarization defines the electrical vector's angle with respect to the unit vectors attached to the coordinate frame in a plane perpendicular to the propagation direction of the light. For a random polarization, the electric field is randomly oriented as the light propagates. For a rectilinear one, the electric field keeps the same angle while propagating. For circular polarization, the electric field turns around the optical axis as the light propagates.

The laser polarization parameter is crucial for achieving high performance mechanical devices in the Type II regime of structural modification in fused silica, since the presence of nanogratings and their orientation strongly affects the etching process (Fig. 73). For achieving optimal surface quality, the laser polarization is required to be transverse to the scanning direction as shown in Fig. 73b and 73c. Average surface quality of 200 nm can be achieved [60]. This value can be further improved using post-processing methods, i.e., CO₂ laser polishing [100, 106, 149, 150].

- Surface roughness

The etching time is an import parameter of the process affecting the mechanical properties of fused silica glass. Based on a previous work [116], the mean peak-to-valley roughness of the surface, R_{tm} , (measured 200 nm via atomic force microscopy) seems not to be influenced by the etching time. Nevertheless, the geometric average slope, Δq , a parameter that indirectly provides information of the density of peaks contained in a given profile, decreases as the etching time increases. Δq is defined by:

$$\Delta q = \sqrt{\frac{1}{L} \int_0^L \left(\frac{dy}{dx} \right)^2 dx} \quad (\text{Appendix 1.1})$$

in which the $y(x)$ defines the topology profile along the x axis and L is the length of the dataset considered (Fig. 74).

The decrease of Δq is consistent with the decrease of local stress concentrators intensities on the micromachined surface and, therefore, leads to higher mechanical strength of the material [60].

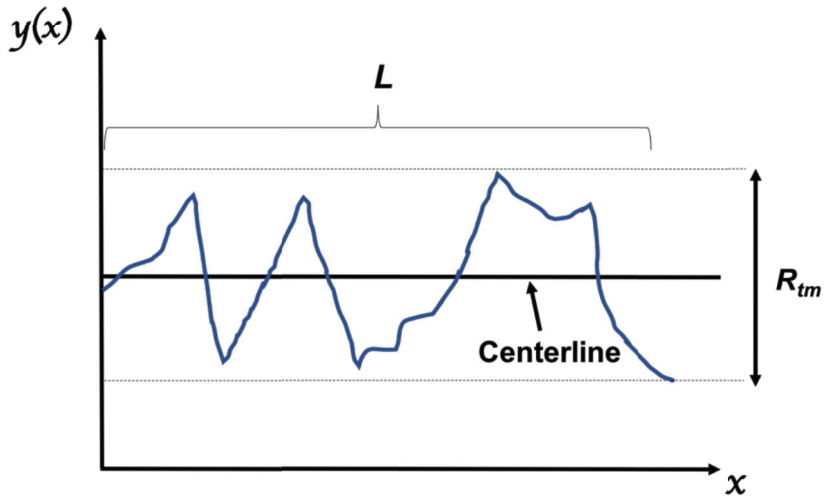


Fig. 74. Illustration of surface quality parameters. The peak-to-valley roughness is indicated by R_{tm} . The geometric average slope, Δq , is a parameter that indirectly provides information of the density of peaks contained in a given profile dataset L .

BIBLIOGRAPHY

- [1] Y. Bellouard, A. Said and P. Bado, "Integrating optics and micro-mechanics in a single substrate: a step toward monolithic integration in fused silica," *Optics Express*, vol. 13, no. 17, pp. 6635-6644, 2005.
- [2] K. Sugioka and Y. Cheng, "Ultrafast lasers—reliable tools for advanced materials processing," *Light: Science & Applications*, vol. 3, no. 149, 2014.
- [3] A. Said, Translume Inc., 2018. [Online]. Available: <http://www.translume.com/index.php/resources/item/186-fused-silica-material-properties>.
- [4] V. Tielen and Y. Bellouard, "Three-dimensional glass monolithic micro-flexure fabricated by femtosecond laser exposure and chemical etching," *Micromachines*, vol. 5, no. 3, pp. 697-710, 2014.
- [5] T. Yang and Y. Bellouard, "Monolithic transparent 3D dielectrophoretic micro-actuator fabricated by femtosecond laser," *Journal of Micromechanics and Microengineering*, vol. 25, no. 10, p. 105009, 2015.
- [6] T. Yang and Y. Bellouard, "Laser-Induced Transition between Nonlinear and Linear Resonant Behaviors of a Micromechanical Oscillator," *Physical Review Applied*, vol. 7, no. 6, p. 064002, 2017.
- [7] S. Wiederhorn and L. Boltz, "Stress corrosion and static fatigue of glass," *Journal of the American Ceramic Society*, vol. 53, no. 10, pp. 544-548, 1970.
- [8] S. Wiederhorn, "Influence of water vapor on crack propagation in soda-lime glass," *Journal of the American Ceramic Society*, vol. 50, no. 8, pp. 407-414, 1967.
- [9] S. Wiederhorn, T. Fett, G. Rizzi, M. Hoffmann and J. Guin, "The effect of water penetration on crack growth in silica glass," *Engineering Fracture Mechanics*, vol. 100, pp. 3-16, 2013.
- [10] M. Tomozawa, "Fracture of glass," *Annual Review of Material Science*, vol. 26, pp. 43-74, 1996.
- [11] D. Marsh, "Plastic flow and fracture of glass," *Proceedings of the Royal Society of London*, vol. 282, no. 1388, 1964.
- [12] J. Custers, "Plastic Deformation of Glass during Scratching," *Nature*, vol. 164, pp. 627-627, 1949.
- [13] F. Célarié, S. Prades, D. Bonamy, L. Ferrero, E. Bouchaud, C. Guillot and C. Marlière, "Glass Breaks like Metal, but at the Nanometer Scale," *Physical Review*

Letters, vol. 90, p. 075504, 2003.

- [14] C. Rountree, R. Kalia, E. Lidorikis, A. Nakano, L. V. Brutzel and P. Vashishta, "Atomistic Aspects of Crack Propagation in Brittle Materials: Multimillion Atom Molecular Dynamics Simulations," *Annual Review of Material Science*, vol. 32, pp. 377-400, 2002.
- [15] M. Pantano, H. Espinosa and L. Pagnotta, "Mechanical characterization of materials at small length scales," *Journal of Mechanical Science and Technology*, vol. 26, no. 2, pp. 545-561, 2012.
- [16] W. Weibull, "A statistical Distribution Function of Wide Applicability," vol. 18, pp. 293-297, 1951.
- [17] A. Jayatilaka and K. Trustrum, "Statistical approach to brittle fracture," *Journal of Materials Science*, vol. 12, no. 7, pp. 1426-1430, 1977.
- [18] C. Kurkjian, R. Albarino, J. Krause, H. Vazirani, F. DiMarcello, S. Torza and H. Schonhorn, "Strength of 0.04-50-m lengths of coated fused silica fibers," *Applied Physics Letters*, vol. 28, no. 10, p. 588, 1976.
- [19] Corning, "HPFS® Fused Silica Standard Grade," Corning, 2003. [Online]. Available: <http://www.valleydesign.com/Datasheets/Corning-Fused-Silica-7980.pdf>.
- [20] V. Srikar and S. Spearing, "A critical review of microscale mechanical testing methods used in the design of microelectromechanical systems," *Journal of Experimental Mechanics*, vol. 43, no. 3, pp. 238-247, 2003.
- [21] O. Kraft and C. Volkert, "Mechanical Testing of Thin Films and Small Structures," vol. 3, no. 3, p. 99-110, 2001.
- [22] D. Zhang, *A Nano-Tensile Testing System for Studying Nanostructures inside an Electron Microscope: Design, Characterization and Application*, Lausanne: Ecole Polytechnique Fédérale de Lausanne (PhD Thesis), 2010.
- [23] W. Oliver and G. Pharr, "Measurement of hardness and elastic modulus by instrumented indentation: Advances in understanding and refinements to methodology," *Journal of Materials Research*, vol. 19, no. 1, pp. 3-20, 2004.
- [24] C. Schuh, "Nanoindentation studies of materials," *Materials Today*, vol. 9, no. 5, pp. 32-40, 2006.
- [25] K. Yoder and D. Stone, "Load and depth sensing indentation tester for properties measurement at non-ambient temperatures," in *Materials Research Society*, San Francisco, California, United States, 1993.

- [26] W. Oliver and G. Pharr, "An improved technique for determining hardness and elastic modulus using load and displacement sensing indentation experiments," *Journal of Materials Research*, vol. 7, no. 6, pp. 1564-1583, 1992.
- [27] Y. Bellouard, T. Colomb, C. Depeursinge, M. Dugan, A. Said and P. Bado, "Nanoindentation and birefringence measurements on fused silica specimen exposed to low-energy femtosecond pulses," *Optics Express*, vol. 14, no. 18, pp. 8360-8366, 2006.
- [28] C. Charitidis and D. Dragatogiannis, "Finite element analysis, stress-strain distribution and size effects rise during nanoindentation of welded aluminum alloy," *International Journal of Structural Integrity*, vol. 4, no. 1, pp. 78-90, 2013.
- [29] J. Freeman, "Mathematical Theory of Deflection of Beam," *The London, Edinburgh, and Dublin Philosophical Magazine and Journal of Science*, vol. 37, no. 275, pp. 855-862, 1945.
- [30] H. Conway, "The large deflection of simply supported beams," *The London, Edinburgh, and Dublin Philosophical Magazine and Journal of Science*, vol. 38, no. 287, pp. 905-911, 1946.
- [31] P. Theocaris, S. Paipetis and S. Paolinelis, "Three-point bending at large deflections," *Journal of Testing and Evaluation*, vol. 5, no. 6, pp. 427-436, 1977.
- [32] T. Warwick, "Blue Scientific," 03 2015. [Online]. Available: <http://www.blue-scientific.com/fracture-behaviour-in-situ-sem/>.
- [33] R. Hibbeler, *Mechanics of Materials*, 8e ed., Prentice Hall PTR, 1991.
- [34] N. Evanno and D. Mendels, "Four Point Bending Test of Thin Films in the nm Through to μm Range," in *MicroNano Integration*, Springer, pp. 185-191, 2004.
- [35] B. Varghese, Y. Zhang, L. Dai, V. Tan, C. Lim and C. Sow, "Structure-Mechanical Property of Individual Cobalt Oxide Nanowires," *Nanoletters*, vol. 8, no. 10, p. 3226-3232, 2008.
- [36] H. Hencky, "On the stress state in circular plates with vanishing bending stiffness," *Zeitschrift für Mathematik und Physik*, vol. 63, no. 1, pp. 311-317, 1915.
- [37] J. Campbell, "On the theory of initially tensioned circular membranes subjected to uniform pressure," *The Quarterly Journal of Mechanics and Applied Mathematics*, vol. 9, no. 1, p. 84-93, 1956.
- [38] J. Beams, W. Walker and H. Morton, "Mechanical properties of thin films of gold and silver," *Physical Review*, vol. 87, no. 3, p. 524, 1952.

- [39] E. Bromley, J. Randall, D. Flanders and R. Mountain, "A technique for the determination of stress in thin-films," *Journal of Vacuum Science & Technology B*, vol. 1, no. 4, p. 1364–1366, 1983.
- [40] P. Lin, *The In-Situ Measurement of Mechanical Properties of Multilayered-Coatings*, Cambridge: Massachusett Institute of Technology (PhD Thesis), 1990.
- [41] J. Vlassak and W. Nix, "A new bulge test technique for the determination of the young's modulus and poisson's ratio of thin films," *Journal of Materials Research*, vol. 7, no. 12, pp. 3242-3249, 1992.
- [42] K. Petersen, "Dynamic Micromechanics on Silicon: Techniques and Devices," *IEEE Transactions on Electron Devices*, vol. 25, no. 10, pp. 1241-1250, 1978.
- [43] K. Petersen and C. Guarnieri, "Young's modulus measurements of thin films using micromechanics," *Journal of Applied Physics*, vol. 50, no. 11, pp. 6761-6766, 1979.
- [44] Y. Kim and M. Allen, "In Situ Measurement of Mechanical Properties of Polyimide Films using Micromachined Resonant String Structures," *IEEE Transactions on Components and Packaging Technology*, vol. 22, no. 2, pp. 282-290, 1999.
- [45] J. Manceau, L. Robert, E. Bastien, C. Oytana and S. Biwersi, "Measurement of Residual Stresses in a Plate using a Vibrational Technique: Application to Electrolytic Nickel Coatings," *Journal of Microelectromechanical Systems*, vol. 5, no. 4, pp. 243-249, 1996.
- [46] T. Ikehara, R. Zwijze and K. Ikeda, "New Method for an Accurate Determination of Residual Strain in Polycrystalline Silicon Films by Analyzing Resonant Frequencies of Micromachined Beams," *Journal of Micromechanics and Microengineering*, vol. 11, no. 1, pp. 55-60, 2001.
- [47] S. Timoshenko, D. Young and W. Weaver, *Vibration Problems in Engineering*, New York: Wiley, 1974.
- [48] X. Wang, N. Li, T. Wang, M. Liu, Wang and L. Wang, "Dynamic characteristic testing for MEMS micro-devices with base excitation," *Measurement Science and Technology*, vol. 18, no. 6, p. 1740–1747, 2007.
- [49] M. Haque and M. Saif, "A review of mems-based microscale and nanoscale tensile and bending testing," *Journal of Experimental Mechanics*, vol. 43, no. 3, pp. 248-255, 2003.
- [50] M. Haque and M. Saif, "Microscale materials testing using MEMS actuators," *Journal of Microelectromechanical Systems*, vol. 10, no. 1, pp. 146-152, 2001.

- [51] I. Chasiotis and W. Knauss, "A new microtensile tester for the study of MEMS materials with the aid of atomic force microscopy," *Journal of Experimental Mechanics*, vol. 42, no. 1, pp. 51-57, 2002.
- [52] R. Liu, H. Wang, X. Li, G. Ding and C. Yang, "A micro-tensile method for measuring mechanical properties of MEMS materials," *Journal of Micromechanics and Microengineering*, vol. 18, no. 6, p. 065002, 2008.
- [53] H. Huang and F. Spaepen, "Tensile testing of free-standing Cu, Ag and Al thin films and Ag/Cu multilayers," *Acta Materialia*, vol. 48, no. 12, pp. 3261-3269, 2000.
- [54] S. Greek and F. Ericson, "Young's Modulus, Yield Strength and Fracture Strength of Microelements Determined by Tensile Testing," in *Microelectromechanical Structures for Materials Research*, Warrendale, Pennsylvania, United States, 1998.
- [55] Y. Zhu, A. Corigliano and H. Espinosa, "A thermal actuator for nanoscale in situ microscopy testing: design and characterization," *Journal of Micromechanics and Microengineering*, vol. 16, no. 2, pp. 242-253, 2006.
- [56] S. Lu, Z. Guoa, W. Ding and D. Dikin, "In situ mechanical testing of templated carbon nanotubes," *Review of Scientific Instruments*, vol. 77, no. 12, p. 125101, 2006.
- [57] C.-E. Athanasiou and Y. Bellouard, "A Monolithic Micro-Tensile Tester for Investigating Silicon Dioxide Polymorph Micromechanics, Fabricated and Operated Using a Femtosecond Laser," *Micromachines*, vol. 6, no. 9, pp. 1365-1386, 2015.
- [58] C.-E. Athanasiou, M.-O. Hongler and Y. Bellouard, "Unravelling Brittle-Fracture Statistics from Intermittent Patterns Formed During Femtosecond Laser Exposure," *Physical Review Applied*, vol. 8, no. 5, pp. 0540013, 2017.
- [59] B. McMillen, C. Athanasiou and Y. Bellouard, "Femtosecond laser direct-write waveplates based on stress-induced birefringence," *Optics Express*, vol. 24, no. 24, pp. 27239-27252, 2016.
- [60] Y. Bellouard, "On the bending strength of fused silica flexures fabricated by ultrafast lasers [Invited]," *Optical Materials Express*, vol. 1, no. 5, p. 151037, 2011.
- [61] A. Champion, *Local effective volume changes in fused silica induced by femtosecond laser irradiation*, Eindhoven: Eindhoven University of Technology (PhD Thesis), 2015.
- [62] M. Malinauskas, A. Zukauskas, S. Hasegawa, Y. Hayasaki, V. Mizeikis, R. Buividas and S. Juodkazis, "Ultrafast laser processing of materials: from science to industry," *Light: Science & Applications*, vol. 5, 2016.

- [63] N. Bloembergen, "Laser-Induced Electric Breakdown in Solids," *IEEE Journal of Quantum Electronics*, vol. 10, no. 3, pp. 375-386, 1974.
- [64] G. Zverev and V. Pashkov, "Self-focusing of laser radiation in solid dielectrics," *Soviet Physics JETP*, vol. 30, no. 4, pp. 616-621, 1970.
- [65] A. Vorobyev and C. Guo, "Femtosecond laser nanostructuring of metals," *Optics Express*, vol. 14, no. 6, pp. 2164-2169, 2006.
- [66] S. Kang, K. Vora, S. Shukla and E. Mazur, "Femtosecond Laser Nanofabrication of Metal Structures Through Multiphoton Photoreduction," in *Nano-Optics for Enhancing Light-Matter Interactions on a Molecular Scale*, Dordrecht, the Netherlands, 2013.
- [67] M. Barberoglou, D. Gray, E. Magoulakis, C. Fotakis, P. A. Loukakos and E. Stratakis, "Controlling ripples' periodicity using temporally delayed femtosecond laser double pulses," *Optics Express*, vol. 21, no. 15, pp. 18501-18508, 2013.
- [68] Q. Sun, S. Juodkasis, N. Murazawa, V. Mizeikis and H. Misawa, "Freestanding and movable photonic microstructures fabricated by photopolymerization with femtosecond laser pulses," *Journal of Micromechanics and Microengineering*, vol. 20, no. 3, p. 035004, 2010.
- [69] L. Luo, C. Li, S. Wang, W. Huang, C. Wu, H. Yang, H. Jiang, Q. Gong, Y. Yang and S. Feng, "Optical microstructures fabricated by femtosecond laser two-photon polymerization," *Journal of Optics A: Pure and Applied Optics*, vol. 3, no. 6, p. 489–492, 2001.
- [70] B. Amos, 2016. [Online]. Available: <http://www.strathclydemesolab.com/>.
- [71] Y. Bellouard, A. Said, M. Dugan and P. Bado, "Fabrication of high-aspect ratio, micro-fluidic channels and tunnels using femtosecond laser pulses and chemical etching," *Optics Express*, vol. 12, no. 10, pp. 2120-2129, 2004.
- [72] G. Spierings, "Wet chemical etching of silicate glasses in hydrofluoric acid based solutions," *Journal of Material Science*, vol. 28, no. 13, p. 6261–6273, 1993.
- [73] A. Marcinkevicius, S. Juodkasis, M. Watanabe, M. Miwa, S. Matsuo, H. Misawa and J. Nishii, "Femtosecond laser-assisted three-dimensional microfabrication in silica," *Optics Letters*, vol. 26, no. 5, pp. 277-279, 2001.
- [74] A. Champion, M. Beresna, P. Kazansky and Y. Bellouard, "Stress distribution around femtosecond laser affected zones: effect of nanogratings orientation," *Optics Express*, vol. 21, no. 21, pp. 24942-24951, 2013.

- [75] A. Champion and Y. Bellouard, "Direct volume variation measurements in fused silica specimens exposed to femtosecond laser," *Optics Express*, vol. 2, no. 6, pp. 789-798, 2012.
- [76] Y. Bellouard, A. Champion, B. McMillen, S. Mukherjee, R. Thomson, C. Pépin, P. Gillet and Y. Cheng, "Stress-state manipulation in fused silica via femtosecond laser irradiation," *Optica*, vol. 3, no. 12, pp. 1285-1293, 2016.
- [77] Y. Barad, H. Eisenberg, M. Horowitz and Y. Silberberg, "Nonlinear scanning laser microscopy by third harmonic generation," *Applied Physics Letters*, vol. 70, no. 8, pp. 922-924, 1997.
- [78] J. Squier and M. Muller, "Third-harmonic generation imaging of laser-induced breakdown in glass," *Applied Optics*, vol. 38, no. 27, p. 5789-5794, 1999.
- [79] G. Marshall, A. Jesacher, A. Thayil, M. Withford and M. Booth, "Three-dimensional imaging of direct-written photonic structures," *Optics Letters*, vol. 36, no. 5, p. 695-697, 2011.
- [80] T. Tsang, "Optical third-harmonic generation at interfaces," *Physical Review A*, vol. 52, no. 5, pp. 4116-4125, 1995.
- [81] J. Schins, T. Schrama, J. Squier, G. Brakenhoff and M. Muller, "Determination of material properties by use of third-harmonic generation microscopy," *Journal of the Optical Society of America B*, vol. 19, no. 7, pp. 1627-1634, 2002.
- [82] V. Bhardwaj, E. Simova, P. Rajeev, C. Hnatovsky, R. Taylor, D. Rayner and P. Corcum, "Optically produced arrays of planar nanostructures inside fused silica," *Physical Review Letters*, vol. 96, no. 5, p. 057404, 2006.
- [83] Y. Shimotsuma, P. Kazansky, J. Qiu and K. Hirao, "Self-organized nanogratings in glass irradiated by ultrashort light pulses," *Physical Review Letters*, vol. 91, no. 24, p. 247405, 2003.
- [84] S. Richter, M. Heinrich, S. Döring, A. Tunnermann, S. Nolte and U. Peschel, "Nanogratings in fused silica: Formation, control and applications," *Journal of Laser Applications*, vol. 24, no. 4, p. 042008, 2012.
- [85] A. Mermillod-Blondin, J. Bonse, A. Rosenfeld, I. Hertel, Y. Meshcheryakov, N. Bulgakova, E. Audouard and R. Stoian, "Dynamics of femtosecond laser induced voidlike structures in fused silica," *Applied Physics Letters*, vol. 94, no. 4, p. 041911, 2009.
- [86] J. Reif, O. Varlamova and F. Costache, "Femtosecond laser induced nanostructure formation: self-organization control parameters," *Applied Physics A: Material*

Science & Processing, vol. 92, no. 4, pp. 1019-1024, 2008.

- [87] J. Sears, "A symmetrically opening optical slit," *Journal of Scientific Instruments*, vol. 10, no. 12, p. 376–377, 1933.
- [88] S. Smith, *Flexures: Elements of Elastic Mechanisms*, FL: CRC Press: Boca Raton, 2000.
- [89] Y. Bellouard, *Microrobotics: Methods and Applications*, FL: CRC Press: Boca Raton, 2010.
- [90] L. Howell, *Compliant Mechanisms*, NJ: John Wiley & Sons: Hoboken, 2001.
- [91] S. Henein, *Conception des structures articulées à guidages flexibles de haute précision*, Lausanne : Ecole Polytechnique Fédérale de Lausanne (Phd Thesis), 2000.
- [92] S. Rajesh and Y. Bellouard, "Towards fast femtosecond laser micromachining of fused silica: The effect of deposited energy," *Optics Express*, vol. 18, no. 20, p. 21490, 2010.
- [93] Y. Bellouard, "Non-contact sub-nanometer optical repositioning using femtosecond lasers," *Optics Express*, vol. 23, no. 22, pp. 29258-29267, 2015.
- [94] G. Stoney, "The Tension of Metallic Films Deposited by Electrolysis," *Proceedings of the Royal Society A: Mathematical, Physical and Engineering Sciences*, vol. 82, no. 553, 1909.
- [95] Q. Sun, H. Jiang, Y. Liu, Y. Zhou, H. Yang and Q. Gong, "Effect of spherical aberration on the propagation of a tightly focused femtosecond laser pulse inside fused silica," *Journal of Optics A: Pure and Applied Optics*, vol. 7, no. 11, p. 655–659, 2005.
- [96] Y. Shen, *The Principles of Nonlinear Optics*, New York: Wiley-Interscience, 1984.
- [97] T. Vasudevan and K. Krishnan, "Dispersion of the stress-optic coefficient in glasses," *Journal of Physics D: Applied Physics*, vol. 5, no. 12, p. 2283, 1972.
- [98] N. Bansal and R. Doremus, *Handbook of Glass Properties*, Orlando: Academic Press, Inc, 1986.
- [99] B. Lawn, *Fracture of brittle solids*, Cambridge: Cambridge University Press, 1975.
- [100] J. Drs, K. Tetsuo and Y. Bellouard, "Laser-assisted morphing of complex three dimensional objects," *Optics Express*, vol. 23, no. 12, pp. 17355-17366, 2015.

- [101] C. Klein, "Characteristic strength, Weibull modulus, and failure probability of fused silica glass," *Optical Engineering*, vol. 48, no. 11, p. 113401, 2009.
- [102] R. Danzer, P. Supancic, J. Pascual and T. Lube, "Fracture statistics of ceramics - Weibull statistics and deviations from Weibull statistics," *Engineering Fracture Mechanics*, vol. 74, no. 18, pp. 2919-2932, 2007.
- [103] R. Danzer, "Some notes on the correlation between fracture and defect statistics: Are Weibull valid for very small specimens?," *Journal of the European Ceramic Society*, vol. 26, no. 15, pp. 3043-3049, 2006.
- [104] W. Gabauer, "The Determination of Uncertainties in Tensile Testing," VOEST-ALPINE STAHL LINZ GmbH, Linz, 2000.
- [105] C. Kurkjian, J. Krause and U. Paek, "Tensile strength characteristics of perfect silica fibers," *Journal de Physique Colloques*, vol. 43, pp. 585-586, 1982.
- [106] M. Serhatlioglu, B. Ortac, C. Elbuken, N. Biyikli and M. Solmaz, "CO₂ laser polishing of microfluidic channels fabricated by femtosecond laser assisted carving," *Journal of Micromechanics and Microengineering*, vol. 26, no. 11, p. 115011, 2016.
- [107] T. Yang, *3D Monolithic Dielectrophoretic Actuators and Resonators Written by Femtosecond Laser*, Lausanne: Ecole Polytechnique Fédérale de Lausanne (PhD Thesis), 2017.
- [108] R. Charles, "Static fatigue of glass," *Journal of Applied Physics*, vol. 29, no. 11, p. 1549, 1958.
- [109] P. Agee and J. Hay, "Stiffness Mapping and the Calculation of Fracture Toughness of Fused Silica," Agilent Technologies, 2011.
- [110] F. Lechenault, C. Rountree, F. Cousin, J. Bouchaud, L. Ponson and E. Bouchaud, "Evidence of Deep Water Penetration in Silica during Stress Corrosion Fracture," *Physical Review Letters*, vol. 106, no. 16, p. 165504, 2011.
- [111] T. Michalske and C. Bunker, "Slow fracture model based on strained silicate structures," *Journal of Applied Physics*, vol. 56, no. 26, p. 2686, 1984.
- [112] P. Lezzi and M. Tomozawa, "An Overview of the Strengthening of Glass Fibers by Surface Stress Relaxation," *International Journal of Applied Glass Science*, vol. 6, no. 1, pp. 34-44, 2015.
- [113] N. Groothoff, M. Hongler, P. Kazansky and Y. Bellouard, "Transition between self-healing process between chaotic and self-organized patterns observed during femtosecond laser writing," *Optics Express*, vol. 23, no. 13, pp. 16993-17007, 2015.

- [114] H. Takagi, *Queueing analysis: a foundation of performance evaluation*, vol. 1, North-Holland, 1991.
- [115] J. Medhi, *Stochastic Models in Queueing Theory*, San Diego, CA: Elsevier Science , 1991.
- [116] Y. Bellouard, E. Barthel, A. Said, M. Dugan and P. Bado, "Scanning thermal microscopy and Raman analysis of bulk fused silica exposed to low-energy femtosecond laser pulses," *Optics Express*, vol. 16, no. 24, pp. 19520-19534, 2008.
- [117] Y. Pomeau and P. Manneville, "Intermittent transition to turbulence in dissipative dynamical systems," *Communications in Mathematical Physics*, vol. 74, no. 2, pp. 189-197, 1980.
- [118] P. Glansdorff and I. Prigogine, *Thermodynamic Theory of Structure, Stability and Fluctuations*, Wiley-Interscience , 1971.
- [119] J. Canning, M. Lancry, K. Cook, A. Weickman, F. Brisset and B. Poumellec, "Anatomy of a femtosecond laser processed silica waveguide [Invited]," *Optical Materials Express*, vol. 1, no. 5, pp. 998-1008, 2011.
- [120] S. Richter, A. Pleich, M. Steinert, M. Heirich, S. Doring, F. Zimmermann, U. Peschel, E. Kley, A. Tunnermann and S. Nolte, "On the fundamental structure of femtosecond laser-induced nanogratings," *Laser Photonics Review*, vol. 6, no. 6, pp. 787-792, 2012.
- [121] C. Inglis, "Stresses in a plate due to the presence of cracks and sharp corners," *Transactions of the Institute of Naval Architects* , vol. 55, pp. 219-230, 1913.
- [122] C. Sun, *Fracture Mechanics*, Elsevier, 2011.
- [123] N. Ray and M. Stacey, "Increasing the strength of glass by etching and ion-exchange," *Journal of Materials Science*, vol. 4, no. 1, pp. 73-39, 1969.
- [124] L. Baikova and V. Pukh, "The effect of the type of chemical treatment on the strength of silica and silicate glasses," *Glass and Ceramics*, vol. 30, no. 12, pp. 834-836, 1973.
- [125] D. Wortmann, J. Gottmann, N. Brandt and H. Horn-Solle, "Micro- and nanostructures inside sapphire by fs-laser irradiation and selective etching," *Optics Express*, vol. 16, no. 3, p. 1517, 2008.
- [126] J. Gottmann, M. Hermans, N. Repiev and J. Ortmann, "Selective Laser-Induced Etching of 3D Precision Quartz Glass Components for Microfluidic Applications—Up-Scaling of Complexity and Speed," *Micromachines*, vol. 8, no. 4, 2017.

- [127] Y. Bellouard, E. Block, J. Squier and J. Gobet, "Plasmon-less surface enhanced Raman spectra induced by self-organized networks of silica nanoparticles produced by femtosecond lasers," *Optics Express*, vol. 25, no. 9, pp. 9587-9594, 2017.
- [128] E. Bricchi, B. Klappauf and P. Kazansky, "Form birefringence and negative index change created by femtosecond direct writing in transparent materials," *Optics Letters*, vol. 29, no. 1, pp. 119-121, 2004.
- [129] B. McMillen and Y. Bellouard, "On the anisotropy of stress-distribution induced in glasses and crystals by non-ablative femtosecond laser exposure," *Optics Express*, vol. 23, no. 6, pp. 86-100, 2015.
- [130] J. Nye, *Physical Properties of Crystals*, Oxford University, 1985.
- [131] E. Mathieu, *Théorie de l'Elasticité des Corps Solides*, Paris: Gauthier-Villars, 1980.
- [132] M. Ribière, *Sur divers cas de la flexion des prismes rectangles*, Université de Bordeaux, 1889.
- [133] L. Filon, "On an approximate solution for the bending of a beam of rectangular cross-section under any system of load, with special reference to points of concentrated or discontinuous loading," *Philosophical Transaction of the Royal Society A*, vol. 201, pp. 63-155, 1903.
- [134] S. Timoshenko and J. Goodier, *Theory of Elasticity*, 3rd Edition ed., McGraw-Hill, 1970.
- [135] M. Sadd, *Elasticity: Theory, Applications, and Numerics*, Elsevier Butterworth-Heinemann, 2005.
- [136] A. Spilman and T. Brown, "Stress birefringent, space-variant wave plates for vortex illumination," *Applied Optics*, vol. 46, pp. 61-66, 2007.
- [137] M. Haldimann, *Fracture strength of structural glass elements - Analytical and numerical modelling, testing and design*, Lausanne: Ecole Polytechnique Fédérale de Lausanne (PhD Thesis), 2006.
- [138] R. Bruckner, "Metastable equilibrium of hydroxyl-free synthetic vitreous silica," *Journal of non-crystalline solids*, vol. 5, no. 4, pp. 281-285, 1971.
- [139] C. Hnatovsky, J. Taylor, P. Rajeev, E. Simova, V. Bhardwaj, D. Rayner and P. Corcum, "Pulse duration dependence of femtosecond laser fabricated nanogratings in fused silica," *Applied Physics Letters*, vol. 87, no. 1, p. 014104, 2005.
- [140] K. Davis, K. Miura, N. Sugimoto and K. Hirao, "Writing waveguides in glass with a

- femtosecond laser," *Optics Letters*, vol. 21, no. 21, pp. 1729-1731, 1996.
- [141] P. Rajeev, M. Gertsvolf, C. Hnatovsky, E. Simona, R. Taylor, P. Corkum, D. Rayner and V. Bhardwaj, "Transient nanoplasmonics inside dielectrics," *Journal of Physics B: Atomic, Molecular and Optical Physics*, vol. 40, no. 11, pp. 273-282, 2007.
 - [142] M. Beresna, M. Gecevicius, P. Kazansky and T. Gertus, "Radially polarized optical vortex converter created by femtosecond laser nanostructuring of glass," *Applied Physics Letters*, vol. 98, no. 20, p. 201101, 2011.
 - [143] C. Hnatovsky, R. Taylor, E. Simova, V. Bhardwaj, D. Rayner and P. Corkum, "Polarization-selective etching in femtosecond laser-assisted microfluidic channel fabrication in fused silica," *Optics Letters*, vol. 30, no. 14, pp. 1867-1869, 2005.
 - [144] C.-E. Athanasiou and Y. Bellouard, "Investigation of the micro-mechanical properties of femtosecond laser-induced phases in amorphous silica," in *Proc. SPIE 9740, Frontiers in Ultrafast Optics: Biomedical, Scientific, and Industrial Applications XVI, 97401E*, San Francisco, California, United States, 2016.
 - [145] E. Glezer and E. Mazur, "Ultrafast-laser driven micro-explosions in transparent materials," *Applied Physics Letters*, vol. 71, no. 7, pp. 882-884, 1997.
 - [146] L. Lucas and J. Zhang, "Industrial Laser Solutions for Manufacturing," 06 01 2012. [Online]. Available: <http://www.industrial-lasers.com/articles/2012/06/femtosecond-laser-micromachining-a-back-to-basics-primer.html>.
 - [147] R. Taylor, C. Hnatovsky and E. Simova, "Applications of femtosecond laser induced self-organized planar nanocracks inside fused silica glass," *Laser & Photonics Reviews*, vol. 2, no. 1-2, pp. 26-46, 2008.
 - [148] Y. Bellouard, "Monolithic Multifunctional Integration in Fused Silica," in *Proc. SPIE 6400, Femtosecond Phenomena and Nonlinear Optics III*, Stockholm, Sweden, 2006.
 - [149] C. Ross, D. MacLachlan, D. Choudhury and R. Thomson, "Towards optical quality micro-optic fabrication by direct laser writing and chemical etching," in *Proc. SPIE 10094, Frontiers in Ultrafast Optics: Biomedical, Scientific, and Industrial Applications XVII*, San Francisco, California, United States, 2017.
 - [150] C. Buerhop, B. Blumenthal and R. Weissmann, "Glass surface treatment with excimer and CO2 lasers," *Applied Surface Science*, vol. 46, no. 4, pp. 430-434, 1990.

Author Contributions

Chapter II: Christos Athanasiou designed, fabricated and characterized the device. Yves Bellouard proposed the concept of the monolithic tensile-tester and supervised the research.

Chapter III: Christos Athanasiou designed the tensile testing device, built the optical setup and performed the experiments. Pieter Vlugter designed the gas-shield chamber as part of another project. Yves Bellouard supervised and coordinated the research.

Chapter IV: Christos Athanasiou performed the experiments and derived the microscopic model. Max Hongler proposed and derived the queuing model. Yves Bellouard proposed the concept, supervised and coordinated the research.

Chapter V: Christos Athanasiou derived the 1D and 2D analytical models. Ben McMillen performed the experiments. Yves Bellouard proposed the concept of waveplates and supervised the research.

Acknowledgements

The research of thesis was carried out at the Galatea Lab at the Institute of Microtechnique at EPFL in Neuchâtel. A significant part also took place in the Microsystems group at the Mechanical Engineering department of TU/e. Many thanks go to:

Prof. Yves Bellouard for directing the project first in TU/e and then at EPFL, for his stimulation, encouragement and support throughout the thesis.

Prof. Joost Vlassak, Prof. Matthieu Lancry and Prof. Fabien Sorin for kindly accepting to be examiners.

Prof. Demetri Psaltis for accepting to chair the committee.

Prof. Max-Olivier Hongler, Dr. Ben McMillen and Pieter Vlugter for their contributions in this work.

Dr. Nathaniel Groothoff, Dr. Alexandros Mouskeftaras, Dr. Tao Yang, Jakub Drs, Pieter Vlugter for their help.

Finally, I would like to express my gratitude to the European Research Council (Galatea project, ERC-2012-StG-307442) for funding this thesis.

Christos Athanasiou,

Neuchâtel, 2017

A handwritten signature in black ink, appearing to be 'CA', with a long horizontal line underneath.

Curriculum Vitae

Christos Edouardos ATHANASIOU

Born on 31st May 1989

Nationality: Greek

c.e.athanasiou@gmail.com

Education

- 2015-2018 Ph.D. Candidate at Galatea Laboratory
Institute of Microengineering, School of Engineering
Ecole Polytechnique Fédérale de Lausanne (EPFL), Switzerland
- 2013-2014 Ph.D. Candidate at Microsystems Group
Department of Mechanical Engineering
Technische Universiteit Eindhoven (TU/e), the Netherlands
- 2007-2012 Diploma in Applied Physics
School of Applied Sciences, Department of Physics
National Technical University of Athens (NTUA), Greece

Journal articles

C.-E. Athanasiou, and Y. Bellouard, "A Monolithic Micro-Tensile Tester for Investigating Silicon Dioxide Polymorph Micromechanics, Fabricated and Operated Using a Femtosecond Laser," *Micromachines*, vol. 6, no. 9, pp. 1365-1386, 2015.

B. McMillen, C. Athanasiou and Y. Bellouard, "Femtosecond laser direct-write waveplates based on stress-induced birefringence," *Optics Express*, vol. 24, no. 24, pp. 27239-27252, 2016.

C.-E. Athanasiou, M.-O. Hongler and Y. Bellouard, "Unravelling Brittle-Fracture Statistics from Intermittent Patterns Formed During Femtosecond Laser Exposure," *Physical Review Applied*, vol. 8, no. 5, pp. 0540013, 2017.

C.-E. Athanasiou, and Y. Bellouard, "On the Long-Term Mechanical Behavior of Fused Silica Under High Tensile Stress and the Effect of Water," (*to be submitted*).

Conferences with published proceedings

B. McMillen, C.-E. Athanasiou, and Y. Bellouard, "Direct-write waveplates using femtosecond lasers: Confined stress states for new polarization devices," *CLEO/Europe-EQEC:2017*, Munich, Germany. (Oral presentation)

C.-E. Athanasiou, and Y. Bellouard, "Investigation of the micro-mechanical properties of femtosecond laser-induced phases in amorphous silica," *Proceedings of SPIE* 9740, 97401E (2016), SPIE Photonics West, San Francisco, United States. (Oral presentation)

C.-E. Athanasiou, and Y. Bellouard, "A monolithic micro-tensile tester for investigation silica micromechanics, fabricated and fully operated using a femtosecond laser," *CLEO:2014, OSA Technical Digest*, paper AW1H.5 (2014), San Jose, United States. (Oral presentation)

Selected conference presentations without proceedings

C.-E. Athanasiou, M.-O. Hongler and Y. Bellouard, "Transition between chaotic and self-organized patterns during femtosecond laser writing in glass: a tool for investigating glass fracture mechanics," Glass and Optical Materials Division Meeting (GOMD) 2017, Waikoloa, United States. (Oral presentation)

C.-E. Athanasiou, and Y. Bellouard, "Investigation of the micro-mechanical properties of femtosecond laser-induced phases in amorphous silica matrix," Photonics West (PW) 2016, San Francisco, United States. (Oral presentation)

C.-E. Athanasiou, and Y. Bellouard, "A monolithic micro-tensile tester fabricated by femtosecond laser to investigate silica's mechanical properties," Conference on Laser Advanced Material Processing (LAMP) 2015, Fukuoka, Japan. (Oral presentation)

C.-E. Athanasiou, and Y. Bellouard, "A monolithic micro-tensile tester for investigating silica micromechanics, fabricated and fully operated using a femtosecond laser," Conference on Lasers and Electro-Optics (CLEO) 2014, San Jose, United States. (Oral presentation)

Honors and Awards

Travel Grant Award, SPIE Optics + Photonics Conference 2017, San Diego, United States.

Second Best Student Presentation Award, Frontiers in Ultrafast Optics: Biomedical, Scientific and Industrial Applications, Photonics West 2016, San Francisco, United States.

Third Place Flash Presentation Award, EPFL Photonics Day 2016 (sponsored by +GF+), Lausanne, Switzerland.

Best Business Plan Award, CTi Entrepreneurship – the Swiss Federal Training Programme for Startup Founders, Class of 2016, Neuchâtel, Switzerland.

Outstanding Student Presentation Award, Conference on Laser Advanced Material Processing (LAMP) 2015, Fukuoka, Japan.

